

GROWTH AND CHARACTERIZATION OF FREE-STANDING GALLIUM NITRIDE
SUBSTRATES BY THE HYDRIDE-METALORGANIC VAPOR PHASE EPITAXY
TECHNIQUE

By

MICHAEL D. REED

A DISSERTATION PRESENTED TO THE GRADUATE SCHOOL
OF THE UNIVERSITY OF FLORIDA IN PARTIAL FULFILLMENT
OF THE REQUIREMENTS FOR THE DEGREE OF
DOCTOR OF PHILOSOPHY

UNIVERSITY OF FLORIDA

2002

To Mom and Dad

ACKNOWLEDGMENTS

Without a great deal of scientific curiosity, I would never have aspired to challenge myself to learn as much as I could about the universe we live in, and by extension to this dissertation, comprehensively learn about a small topic within it. Several influences in my formative intellectual and scholastic years stand out, and I wish to recognize them.

Dr. Carl Sagan, Dr. Richard Feynmann, Don Herbert, J. R. R. Tolkein, Dr. Isaac Asimov, Sir Arthur C. Clarke, and Sir David Attenborough were standbys of mine, and each left a permanent mark upon my intellect, and I thank them for it.

Mr. Robert Parker and Dr. James Bock ("Doc Bock") were, aside from my father and uncle, the best teachers I have ever had. They taught me how to think critically and gave me wide latitude in my science education. Because of their fascination with problem solving and the fun, mystery, and awe with which they presented their science, I chose to be a chemical engineer.

My advisor, Dr. Tim Anderson, gave me great latitude—perhaps too much, some might say—to investigate topics that interested me. I am grateful in many ways for his advice, experience, critical thinking, knowledge, and especially his patience.

Dr. Olga Kryliouk made me a better scientist and researcher, by playing devil's advocate. She, more than anyone while I have been a student, has refined my view of science, always returning my views to the objective and dispassionate, which is where

science should be performed. Although we have occasionally disagreed, I hold her in the highest respect regardless, and find her the consummate professional scientist.

I would like to thank Mike Mastro, Dr. Billy Stanbery, Dr. Roger Aparicio, Dave Moorehead, Dr. Albert Davydov, Dr. Tao Feng, and Jeanne Tokarz for being sounding boards for my ideas, rants, theories, gripes, and questions. They advanced my research considerably and did wonders for my peace of mind.

The staff of Microfabritech has always been helpful in ways that go beyond mere acknowledgements in a dissertation. Scott and Tanya Gapinski, and Diane Badylak have been invaluable during my entire tenure as a researcher at University of Florida. Dr. Mark Davidson has been a continual source of reference and support, and I would like to thank Dr. Paul ("Doc") Holloway for both his technical and social contributions to the cause. Without William ("Pete") Axson, I would still be building the system, and his expertise, especially with electronics, is continually missed.

I would like to thank Dr. Cammy Abernathy for her insight and help, often without being aware of it. She continually provided me a different viewpoint, which was invaluable, and always was available to field ideas, no matter how outlandish or novel. Many thanks go to Dr. Fan Ren and Dr. Jason Weaver, for their perspectives and understanding regarding devices and kinetics, as well.

Without my friends, I would have quit in frustration. Thanks go to Dr. Tom Murphy, Heidi Bendeck, Susan Gondran, Andrew Potratz, Nicole M. Jackson, Nancy Miller, David Van De Car, Jennifer Huffman, Meggen Tucker, Alison Austin, Lisa Little, John Berlo, and Kristi McDowell, for being there all of these years.

I would like to thank my aunt, Jeanne Lubanovic, for her continual support and encouragement. My uncle David Reed encouraged my scientific curiosity, starting at age 6 with my first chemistry set. He is also partially responsible for my sense of humor, and thanks to him I can always keep my spirits high, no matter the circumstances.

And finally, all my thanks go to Mom and Dad, for everything.

TABLE OF CONTENTS

	<u>Page</u>
CHAPTERS	
ACKNOWLEDGMENTS	iii
ABSTRACT	ix
1 INTRODUCTION	1
Growth Techniques	2
Substrate Issues	5
2 LITERATURE REVIEW: GALLIUM NITRIDE.....	9
Crystalline Gallium Nitride.....	9
Properties	9
Physical properties	9
Thermochemical properties	10
Optoelectronics properties	10
Electrical properties	14
Defects in Gallium Nitride.....	16
Gallium Nitride Growth.....	21
Methods.....	21
Substrates	23
Layers on Lithium Gallium Oxide Substrates	25
Gallium Nitride Substrate Growth	30
Historical efforts	30
Current approaches	31
Gallium Nitride Photonic Devices.....	47
Light-Emitting Diodes	47
Laser Devices.....	49
Gallium Nitride Device Production	51
3 GROWTH INVESTIGATIONS OF THE HYDRIDE-METALORGANIC VAPOR PHASE EPITAXY (H-MOVPE) SYSTEM	55
The H-MOVPE Reactor System.....	56
Chemistry.....	56

TABLE OF CONTENTS

	<u>Page</u>
CHAPTERS	
ACKNOWLEDGMENTS	iii
ABSTRACT	ix
1 INTRODUCTION	1
Growth Techniques	2
Substrate Issues	5
2 LITERATURE REVIEW: GALLIUM NITRIDE.....	9
Crystalline Gallium Nitride.....	9
Properties	9
Physical properties	9
Thermochemical properties	10
Optoelectronics properties	10
Electrical properties	14
Defects in Gallium Nitride.....	16
Gallium Nitride Growth.....	21
Methods.....	21
Substrates	23
Layers on Lithium Gallium Oxide Substrates	25
Gallium Nitride Substrate Growth	30
Historical efforts	30
Current approaches	31
Gallium Nitride Photonic Devices	47
Light-Emitting Diodes	47
Laser Devices.....	49
Gallium Nitride Device Production	51
3 GROWTH INVESTIGATIONS OF THE HYDRIDE-METALORGANIC VAPOR PHASE EPITAXY (H-MOVPE) SYSTEM	55
The H-MOVPE Reactor System.....	56
Chemistry.....	56

Design	59
Experimental Procedures	67
Initial Investigations.....	69
Parametric Investigation of the H-MOVPE System	71
Method	72
Temperature	74
X-ray diffraction (XRD)	78
Atomic force microscopy (AFM)	83
Auger electron spectroscopy.....	88
SIMS	91
Summary of temperature optimization	97
Hydrogen Chloride/Gallium Ratio.....	98
Growth rate	99
X-Ray diffraction	100
AFM	102
SIMS	103
Photoluminescence	106
Summary of HCl/Ga optimization	109
Ammonia/Gallium Ratio.....	110
Growth rate	110
X-ray diffraction	112
AFM	113
SIMS	114
Photoluminescence: Yellow Luminescence	116
Films Grown upon Two-inch-diameter Sapphire Substrates.....	120
Summary	123
 4 EQUILIBRIUM MODELING OF THE H-MOVPE REACTOR CHEMISTRY	125
Equilibrium Calculations for the H-MOVPE System.....	126
Equilibrium Theory.....	126
Equilibrium Calculations for the H-MOVPE System: Temperature Variation	129
Gas phase	131
Calculations with liquid phase rejection	143
Calculations with liquid phase present	154
Conclusions.....	161
Equilibrium Calculations for the H-MOVPE System: Cl/Ga Variation	162
Equilibrium Calculations for the H-MOVPE System: NH ₃ Variation	170
Summary	173
 5 MODELS OF NITRIDE SOLID SOLUTIONS	175
Thermodynamics of [B,Al, In]GaN Solid Solutions	175
The Delta Lattice Parameter Model	176
The Valence Force Field Model	177

Abstract of Dissertation Presented to the Graduate School
of the University of Florida in Partial Fulfillment of the
Requirements for the Degree of Doctor of Philosophy

GROWTH AND CHARACTERIZATION OF FREE-STANDING GALLIUM NITRIDE
SUBSTRATES BY THE HYDRIDE-METALORGANIC VAPOR PHASE EPITAXY
TECHNIQUE

By

Michael D. Reed

May 2002

Chairman: Dr. Timothy Anderson
Major Department: Chemical Engineering

A novel chemistry was investigated and characterized for the atmospheric-pressure deposition of gallium nitride films that combined the advantages of the high crystal quality of metalorganic vapor-phase epitaxy (MOVPE) with the high growth rate of hydride vapor phase epitaxy (HVPE). The limits of the hydride-metalorganic vapor phase epitaxy (H-MOVPE) growth envelope between 500°C and the furnace-limited 950°C were investigated and compared to literature results. Variation of process parameters such as V/III ratio and HCl/Ga ratio was also researched, and the effects upon film quality were tabulated. Films were characterized by growth rate measurement, X-ray diffraction (XRD), atomic force microscopy (AFM), Auger electron spectroscopy (AES), secondary ion mass spectrometry (SIMS), and photoluminescence (PL). The best results for single-crystalline GaN film growth on sapphire were obtained at 950°C, an ammonia flow rate of 500 sccm, and an HCl/Ga ratio of 2:1.

Thick gallium nitride films were grown upon lithium gallium oxide (LGO) and lithium aluminum oxide (LAO) substrates, which were nearly lattice-matched to gallium nitride. While the films grown upon LGO possessed superior crystal quality and surface morphology, the films grown upon LAO possessed greater mechanical stability and much lower impurity concentrations. Oxygen incorporation, in particular, was very high for films grown upon LGO. Investigation by SIMS revealed evidence of decomposition of the LGO substrate during hydride growth, but no decomposition of the LAO.

Finally, the thermodynamics of both the growth chemistry and nitride solid solutions were investigated. Theoretical variations of growth rate with process parameters were predicted and compared with experiment. While general trends between theoretical and experimental growth rates were similar, the theoretical results were not descriptive of the experimental without arbitrarily increasing the stability of the gallium nitride solid phase. The solid solution behavior of the nitrides was modeled by regular solution theory, using several models for interaction parameters. An empirical model was developed for sole use with nitrides and compared with literature models. Experimental results for the InGaN system proved the model statistically indistinguishable from other published numerical and theoretical models.

CHAPTER I INTRODUCTION

As the millennium turned, about 200 million people used the Internet in some capacity. Whether the form is electronic mail, e-commerce, or World Wide Web usage, Internet connectivity is quickly becoming a way of life. Video-on-demand, Internet telephony, and streaming video and audio are growing in popularity. With this exponential growth of Internet computing, information transmission, retrieval, and storage are playing an increasingly important role in everyday life.

The sheer number of Internet-connected users demands the capability to transmit, retrieve, and store data at very high rates. Currently, high-speed data transmission is accomplished by transmitting infrared laser light through fiberoptic cables. Lasers and photodetectors use the semiconductor alloy system indium gallium arsenide phosphide ($\text{In}_x\text{Ga}_{1-x}\text{As}_y\text{P}_{1-y}$), which is deposited on indium phosphide substrates (InGaAsP/InP). By adjusting the alloy composition, this material can emit light at 1.55 or 1.3 μm , which are the wavelengths of minimum loss in fiberoptic cables.

Using lasers fashioned from a semiconductor called gallium nitride may increase the bandwidth of existing cables. Commercially available gallium nitride lasers operate at a band gap energy of 3.4 eV, and an operational wavelength of $\sim 405 (\pm 10)$ nm. This wavelength is less than one-third of the width of the 1.3 μm wavelength of indium gallium arsenide phosphide. Hence, if the limiting step in information transmission is the throughput per line, over twice as much information (accounting for an additional

between-bit pause) may be transmitted per unit time with devices made from gallium nitride.

The same advantage of using shorter wavelengths carries over to data storage. Compact discs recorded using gallium nitride lasers may store 4.6 times as much information as CDs made using traditional GaAs lasers, because the compression occurs in both radial and lateral directions. When factors such as multi-level disc design and data compression are compounded with this, CD capacity may be increased 31-fold.

Photonic devices incorporating gallium nitride are not limited to information storage and transmission. As an emitter of blue light, the material completes the red-yellow-blue primary color combination from which all tints—including white—may be created. Blue light-emitting diodes (LEDs) are currently in industrial production for uses as mundane as billboards, to as esoteric as stage lighting. By alloying gallium nitride with indium nitride, or by doping with magnesium in sufficient quantity, green and yellow light may be obtained as well. Alternately, using phosphors when encapsulating the device can yield true white light from GaN LED devices.

Growth Techniques

Gallium nitride crystal growth can be achieved by several general techniques, including but not limited to metalorganic chemical vapor deposition (MOCVD), molecular beam epitaxy (MBE), hydride vapor phase epitaxy (HVPE), atomic layer epitaxy (ALE), pulsed laser deposition (PLD), supersonic arcjet plasma deposition, sublimation sandwich growth, pendeo-epitaxy, and high-pressure/high-temperature melt growth. The first four methods, and particularly the first two, are the most widely used. A table of gallium nitride growth methods is given as Table 1.

Table 1-1. Methods of gallium nitride growth.

Method	Temperature (°C)	Pressure (Torr)	Advantages	Disadvantages
MOCVD	950+	76-760	<ul style="list-style-type: none"> • High quality film • Uniformity • Scalability • Well-understood • Off-the-shelf equipment 	<ul style="list-style-type: none"> • Low (< 20%) In incorporation
MBE	650-850	10^{-5}	<ul style="list-style-type: none"> • Uniformity • In-situ characterization • Abrupt junctions • High In incorporation 	<ul style="list-style-type: none"> • Low growth rate • Leakage currents in devices • Residual donor concentration
HVPE	950+	760	<ul style="list-style-type: none"> • Very high growth rate • High quality 	<ul style="list-style-type: none"> • Uniformity • No Al compounds • Junction abruptness • Source issues • Low In incorporation
ALE	500-700	10^{-5} and higher	<ul style="list-style-type: none"> • Uniformity • In-situ characterization • Abrupt junctions • High In incorporation 	<ul style="list-style-type: none"> • Low growth rate • Inefficient use of reactants
PLD	600-700	0.1-0.2	<ul style="list-style-type: none"> • Single-crystalline film • p-type doping • No reactive chemicals 	<ul style="list-style-type: none"> • Particle generation • Rough surfaces
Arcjet plasma	700-800	0.3 - 1	<ul style="list-style-type: none"> • Single-crystalline film 	<ul style="list-style-type: none"> • Uniformity • Temperature control • Particle generation
Sublimation Sandwich	1100-1300	760	<ul style="list-style-type: none"> • High growth rate • High quality 	<ul style="list-style-type: none"> • Limited wafer size • Bulk technique, not for devices
High-pressure High-temperature Melt growth	1400-1600	1.5×10^7	<ul style="list-style-type: none"> • High-quality • High growth rate • Bulk growth 	<ul style="list-style-type: none"> • Not scalable • Expensive • Residual doping

Metalorganic chemical vapor deposition (MOCVD) is a process described by the gas phase surface reaction at elevated temperatures of a dilute gallium metalorganic, such as trimethylgallium (TMG) or triethylgallium (TEG), with ammonia. The metalorganic decomposes at the wafer surface to provide gallium adatoms to the growing GaN film, while the ammonia provides a reactive nitrogen source. These reactants combine in a 1:1 stoichiometric ratio to form a wurtzite (hexagonal) or zincblende (cubic) crystal structure, depending on the substrate. MOCVD is a well-understood technology, is readily scalable, and MOCVD equipment is available off-the-shelf.

Molecular beam epitaxy uses a molecular beam of gallium atoms that react with NH_3 or an N_2 plasma under high vacuum (10^{-5} Torr) and moderate growth temperature (650 to 850°C). MBE growth yields greater uniformity across the wafer and superior smoothness compared to MOCVD-grown films. Furthermore, MBE growth may be monitored in situ for improved process control.

Hydride vapor phase epitaxy (HVPE) is an atmospheric-pressure gas-phase CVD growth technique that takes place in two steps. The first step generates gallium chloride (GaCl) by passing a diluted HCl stream over a boat of liquid gallium. The HCl reacts spontaneously at the liquid surface to form the volatile chloride, which then flows downstream. The gallium chloride then reacts with ammonia above the surface of a substrate at elevated temperature, typically 1000 to 1100°C. The primary advantage of HVPE is its high growth rate for single-crystalline GaN film, which may run as high as 120 microns per hour

Atomic layer epitaxy (ALE) is the sequential deposition of monolayers to grow gallium nitride. The substrate is exposed to two precursors, one of which supplies

gallium to the nitrogen-terminated surface, and another that supplies the newly-gallium-terminated surface with nitrogen. Typically, TMG and NH_3 are used as precursors. ALE is typically conducted at MBE pressure and temperatures of 500 to 700°C.

The other five techniques previously mentioned—pulsed laser deposition (PLD), supersonic arcjet plasma deposition, sublimation sandwich growth, pendeo-epitaxy, and high-pressure/high-temperature melt growth—are novel and/or primarily experimental techniques, and will only be briefly described. Pulsed laser deposition uses an excimer laser to ablate a pressed GaN pellet in a high-vacuum chamber, and the vaporization products react at the wafer surface, similar in principle to MBE. Ammonia is supplied in excess to facilitate high-quality film growth. The arcjet plasma technique uses a supersonic plasma jet in vacuum to provide active nitrogen and gallium sources to the wafer surface.

Sublimation sandwich growth uses sublimation and recondensation of gallium nitride powder to grow GaN epilayers at elevated temperatures. Ammonia diffuses into the gap between heated powder and inverted substrate to provide an abundance of reactive nitrogen to the substrate surface.

Finally, the high-temperature, high-pressure melt growth technique—which will be detailed elsewhere in this work—uses nitrogen bubbled through a nitrogen-saturated melt at high pressure to grow gallium nitride films close to thermodynamic equilibrium.

Substrate Issues

The gallium nitride LED and the gallium nitride blue laser both require high-quality single crystalline films for reliable and efficient operation. The laser demands the highest quality crystal because photons may recombine at defects such as dislocations. In inferior quality material, this prevents the density of photons from becoming high enough

to achieve a population inversion, and the material fails to lase. For LEDs, highly defective material might not preclude luminescence, but it may degrade the lifetime of the device by generating short-circuits and “dark line defects,” which are non-luminescent areas of material associated with magnesium or zinc electromigration at dislocations. For these reasons, crystal quality is of paramount importance for the fabrication of devices.

The ideal solution to this quandary is to grow gallium nitride epilayers—where the charge carriers combine to produce the photons—upon gallium nitride substrates. In such a case, the subsequent film merely continues the crystal structure of the substrate. No discontinuity at the film/substrate interface complicates the energy configurations or surface energy of successive layers. No thermal or lattice mismatches exist to generate stress. There are no stress-induced dislocations, microtwins, microcracks, or macrocracks. As a result, electromigration and solid-state diffusion of dopants and contact materials are suppressed, and hence short-circuits, dark-line defects, and mechanical failures are reduced. Therefore, because homoepitaxially-grown films contain fewer defects than films grown upon other substrates, the resulting devices are more reliable, of higher quality, and last longer.

Unfortunately for gallium nitride device engineers, gallium nitride substrates are not readily available from vendors “off the shelf.” The best available commercial substrate at present is a two-inch diameter sapphire wafer uniformly coated with several microns of gallium nitride. This is not the ideal, because dislocation density is still high, and the wafers are very expensive (\$2000/wafer, as of April 2000). Alternatively, one-inch diameter bulk GaN substrates can be purchased, but the availability is very limited,

and the expense is still high (\$1800, as of March 2002). Silicon carbide is a still-poorer second, both because of the high expense and a significant mismatch with gallium nitride of both lattice parameter (-3.4 %) and thermal expansion coefficient (-33.1%).

The most popular substrate for gallium nitride growth, however, is sapphire. Although the lattice mismatch is large (16.1%), sapphire is inexpensive, thermally and chemically stable, and produces single-crystalline hexagonally-oriented films. While these films tend to be highly defective, with dislocation densities typically of order $10^7/\text{cm}^2$ and sometimes as high as $10^{10}/\text{cm}^2$, techniques are available to greatly reduce the defect density and increase the crystal quality of the film. Unfortunately, these procedures are time-intensive and increase the number of steps to complete a device.

Two potential alternatives to sapphire are lithium gallium oxide (lithium gallate, LiGaO_2 , or LGO) and lithium aluminum oxide (lithium aluminate, $\gamma\text{-LiAlO}_2$, or LAO). Both films produce hexagonal, single crystal gallium nitride films of high quality. Lithium gallium oxide is an orthorhombic crystal that is very nearly an identical match to gallium nitride's lattice constant (-0.1% mismatch) and thermal expansion coefficient (<10% average mismatch in basal plane). As a result, stress related dislocations and cracks should be much less numerous for gallium nitride films on LGO (GaN/LGO) than for gallium nitride films on sapphire ($\text{GaN/Al}_2\text{O}_3$) or silicon carbide (GaN/SiC). Similar to LGO, LAO has a very close lattice (-1.75%) and thermal (18%) mismatch to gallium nitride, though not quite as good as LGO. Lithium aluminum oxide is more mechanically, chemically, and thermally stable than LGO. The possibility exists that thick films grown upon these substrates may be removed and used for subsequent epitaxial growth.

The purpose of this work is to investigate and evaluate the potential of these oxide crystals for use as templates for the growth of free-standing gallium nitride thick films. In the course of this investigation, a custom CVD reactor was built and analyzed. Detailed models of both process fluid dynamics and process thermodynamics were studied. Process parameters such as growth temperature, hydrogen chloride to trimethylgallium flow ratio, ammonia to trimethylgallium flow ratio, and wafer-to-nozzle distance were varied, and their effects upon the structural, electrical, and luminescent properties of the film were studied. From this body of knowledge, various procedures and growth schedules were evaluated for the production of free-standing gallium nitride films using LGO and LAO templates.

This work details the growth system, the parametric study, and the results of different techniques explored for the production of free-standing gallium nitride substrates.

CHAPTER 2 LITERATURE REVIEW: GALLIUM NITRIDE

Crystalline Gallium Nitride

Properties

Physical properties

Gallium nitride (GaN) is a wide bandgap direct semiconductor. It may be created in either of two crystalline forms: the metastable zincblende cubic structure with $E_g=3.45$ eV (Fig. 2-1a) and the wurtzitic hexagonal structure with $E_g = 3.39$ eV (Fig. 2-1b) [1].

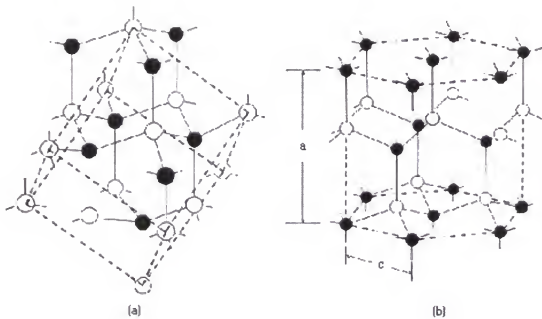


Fig. 2-1. Crystal structure of gallium nitride. (a) zincblende; (b) wurtzite [2].

Table 2-1. Physical properties of wurtzite gallium nitride.

Property		Ref.
Lattice constant (Å)	a: 3.18 c: 5.185	1, 3-5
Thermal expansion coefficient ($\times 10^{-6}/\text{K}$)	a: 5.59 c: 3.17 300K - 700K 7.75 700K - 900K	1, 5 1, 5
Color	gray to yellow to white to clear	1
Solubilities	insol. alc., v. sl. sol. alkali, sol. boiling H_3PO_4	1, 5

Thermochemical properties

Thermodynamically, gallium nitride is a “line compound,” meaning that its solid phase is stable over an extremely narrow region of compositions, namely $x_{\text{Ga}}=0.500$, when shown on a T-x phase diagram (Fig. 2-2) [6]. A P-T phase diagram shows the other thermodynamically interesting feature of gallium nitride growth (Fig. 2-3). At a typical growth temperature, gallium nitride is unstable. Without accounting for the kinetic barrier for decomposition, gallium nitride will either congruently sublime or decompose into nitrogen and nitrogen-saturated gallium droplets above $\sim 700^\circ\text{C}$. This result has been widely studied in the literature [7-10].

Optoelectronics properties

Gallium nitride is used in optoelectronic devices as a consequence of three of its electronic properties. Its band gap, or the energy difference between its conduction and valence bands, is classified as direct. This means that the minimum energy location in phase space for a carrier in the conduction band is the same as the maximum energy location in phase space for the carrier in the valence band (Fig. 2-4) [11]. As a result, transitions between the two bands may proceed directly; a third body is not necessary to

provide or absorb either energy or momentum in the transition. This results in high efficiency recombinations producing photons.

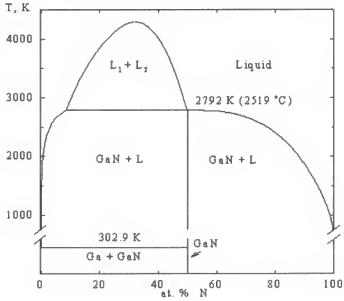


Fig. 2-2. Gallium nitride T-x diagram, at equilibrium N_2 pressure [6].

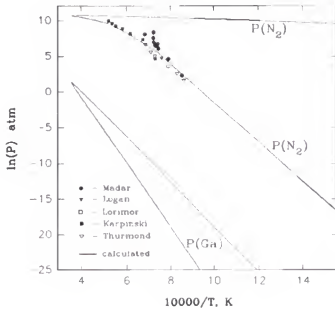


Fig. 2-3. Gallium nitride P-T phase diagram [7, 12-16].

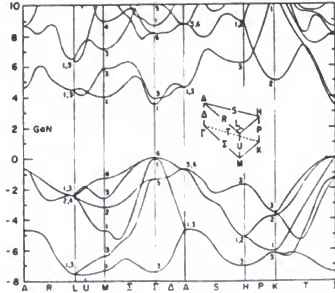


Fig. 2-4. Wurtzite gallium nitride band diagram [17, 18].

The second property influencing the commercial usage of GaN is the width of the energy gap itself. The value of 3.39 eV characteristic of the wurtzite phase, which is the predominant crystalline type currently grown, resides in the shallow ultraviolet wavelengths of the electromagnetic spectrum (Fig. 2-5). This facilitates doping to create centers for carrier recombination in wavelengths in the blue region of the spectrum [19, 20]. Not only do these photons carry more energy, but also their smaller wavelengths have enormous implications for information storage and transmission. The resolution of the scanning laser doubles when the wavelength of the detection photon is cut in half. Because the blue GaN laser can resolve features half the size of red GaAs lasers, four times as much information may be stored on a compact disc. Also, twice as much information may be sent along fiberoptic cables with coherent blue light than with coherent red light, effectively doubling bandwidth [21, 22].

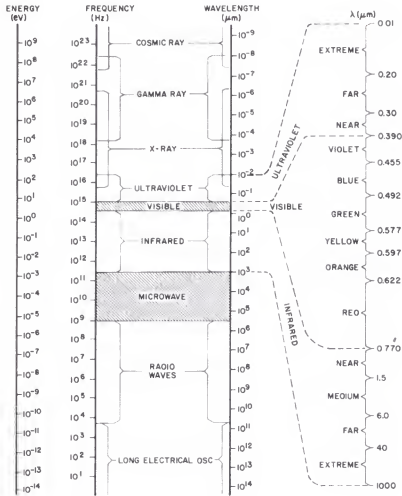


Fig. 2-5. The electromagnetic spectrum [23].

Finally, gallium nitride readily forms alloys with other III-N semiconductors, which extends the available spectrum. Of particular interest are the alloys GaN forms with AlN ($E_g = 6.2$ eV, lattice constant (a) = 3.104 \AA) and InN ($E_g = 1.9$ eV, lattice constant (a) = 3.53 \AA) [21]. These alloys permit a range of solid solutions with band gap energies from deep ultraviolet to infrared. Furthermore, pseudoternary $\text{Al}_x\text{Ga}_y\text{In}_{(1-x-y)}\text{N}$ alloys can theoretically be tailored to accommodate a range of band gaps for a given lattice constant (Fig. 2-6).

Alloys are used in electroluminescent (EL) devices to provide optical confinement layers, especially in multi-quantum-well devices to decrease linewidths and generate cavity modes for lasers. Also, in some applications, the band gap difference between alloys is used to create carrier confinement, e.g. two-dimensional electron gases.

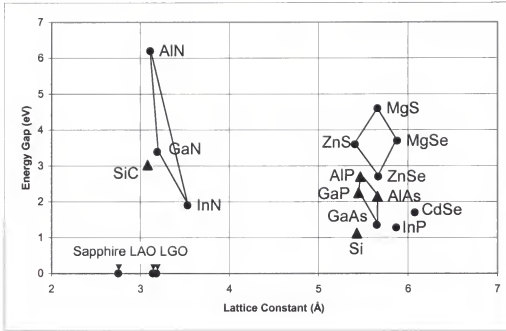


Fig. 2-6. Band gap vs. lattice constant for several semiconductors [24]. Circular and triangular markers represent direct and indirect energy band gap types, respectively.

Electrical properties

Gallium nitride is a semiconductor that is intrinsically n-type, due to a high concentration of native defects. As detailed in the next section, these are believed to be either nitrogen vacancies or terminated ends of edge dislocations. Typical net donor concentrations are 10^{17} to $10^{18}/\text{cm}^3$ for MOCVD-grown GaN and $10^{18}/\text{cm}^3$ for HVPE-grown GaN. Despite this propensity to be heavily n-type, GaN may be doped p-type with Mg, and less commonly, Zn. A comprehensive list of dopants, for the hydride chemistry, is given in Table 2-2.

Table 2-2. Dopants studied in gallium nitride for the hydride process. In addition, Pankove performed ion implantation of the following into hydride films and studied their photoluminescence spectra [25]: Li, Be, B, C, O, Na, Mg, Al, Si, P, S, Cl, K, Ca, Sc, Fe, Ca, Ni, Cu, Zn, Ge, As, Se, Kr, Sr, Zr, Ag, Cd, Sn, Te, Ba, Au, Hg, Dy, Er.

Dopant	Type	References
Mg	p	1, 26-33
Zn	p	1, 30-60
Si	n	1, 38, 54, 61
Ge	n	1, 38, 54, 62
Cd	p	30, 38, 42, 54, 59, 63-66
Sn	n	54
Dy	p	67
Cu	p	61
Cl	n	61
Ni	p	35, 61
As	n	68
P	n	68
Fe	p	35, 61
S	n	32
Cu	p	35
Cr	p	35, 61
Hg	p	1, 32
Li	p	32, 67
Be	p	67

Reported electron mobilities have recently topped $1000 \text{ cm}^2/\text{V-s}$ at room temperature [69]. Johnson's and Keyes's figures of merit, typically used to compare materials for high-power transistors, are shown in Table 2-3. The electric field of the material at breakdown is E_B , V_{sat} is the saturated electron velocity, and σ_T is the thermal conductivity of the material. Johnson's figure of merit applies to the power and frequency capabilities of the material, while Keyes's accounts for size effects of the devices and the ability to dissipate heat. Despite this, Keyes's figure does not take into account thermal stability, which is also desirable [70].

Table 2-3. Figures of merit for various semiconductor materials, from Reference 2.
 Johnson's figure of merit: $E_B V_{sat}/2\pi$ (V/s) Keyes's figure of merit: $\sigma_T (eV_{sat}/K)$ (W/cm-K)

Material	Johnson's	Ratio to silicon	Keyes's	Ratio to silicon
Si	4.75×10^{11}	1.0	2.39×10^8	1.0
GaAs	12.5×10^{11}	2.63	1.07×10^8	0.45
3C-SiC	160.0×10^{11}	33.7	1.39×10^9	5.82
6H-SiC	125.0×10^{11}	26.3	1.22×10^9	5.10
GaN	80.0×10^{11}	16.8	4.20×10^8	1.76
Diamond	430.0×10^{11}	90.5	7.68×10^8	32.1

Defects in Gallium Nitride

In gallium nitride, the primary defect structures are nitrogen vacancies, stacking faults, dual position boundaries, dislocations, microtwins, and microcracks [29, 71-78]. Nitrogen vacancies are point defects that are donors (Fig. 2-7). They are a result of the high N_2 vapor pressure at high temperature. Thermodynamically, a perfect incorporation of atomic nitrogen requires high N_2 overpressures, or a plentiful source of active nitrogen. At a typical reactor temperature of 950°C and a typical pressure of 76 Torr or atmospheric pressure, GaN will incongruently sublime into a nitrogen-saturated gallium liquid, and the diatomic N_2 [16, 79-82]. This is not a reversible reaction; a source of active nitrogen such as ammonia or a nitrogen plasma must be present to retard this process. Because of the large thermodynamic driving force [83-86], a fraction of the nitrogen sites in the crystal will remain vacant, as this is the lowest-energy configuration of the system. Each of these vacancies has the effect of a donor. As a result, these "native defects" cause the as-grown undoped film to be n-type, typically with $10^{17}/\text{cm}^3$ (or higher) donors on sapphire [87].

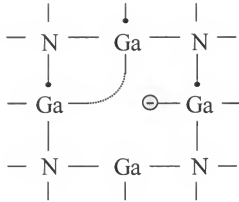


Fig. 2-7. Two-dimensional schematic of a nitrogen vacancy. Two of the electrons from adjacent gallium atoms reconstructs a bond; the other acts as a donor [88].

The conclusion that the native defect is a nitrogen vacancy is still speculative, however [89]. Recent theoretical models have suggested that the native donor may actually be a gallium-terminated edge dislocation [90]. The functional equivalent of this arrangement is a vertical stack of nitrogen vacancies, due to dangling bonds. Therefore, according to this model, highly dislocated films will be heavily n-type.

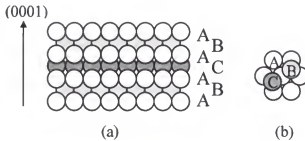


Fig. 2-8. (a) Stacking fault in a hexagonal crystal, viewed parallel to the basal plane. (b) Atomic positions B and C on basal plane A.

Stacking faults are variations in the order of the crystal (Fig. 2-8). In a standard wurtzitic crystal, there are two low-energy configurations for stacking atoms in the $\langle 0001 \rangle$ direction, labeled B and C in the figure. The base configuration is labeled as A. In a perfect wurtzitic crystal, the atoms are stacked in a repeating ABABAB pattern in the $\langle 0001 \rangle$ direction, throughout the crystal. When a stacking fault is present, the order switches from ABABAB . . . to ABACAB . . . or ABABC . . . for some period. In any case, there is some disruption in long-term order in the crystal [91]. Since the energy difference in these configurations is very small because this is a second-nearest-neighbor effect, this happens often in GaN [91].

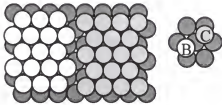


Fig. 2-9. Dual position boundary, viewed normal to the basal plane, illustrating convergence of B on A and C on A crystallites.

Dual position boundaries are the intersections between crystallites which grow together from different nucleation sites (Fig. 2-9). In heteroepitaxial growth of GaN on sapphire, the first phase of epitaxial crystal growth is the formation of small islands of GaN upon the sapphire substrate. These islands then coalesce, forming a continuous film, at which time growth proceeds in step-mode fashion. The initial islands may form

upon either B or C sites when nucleating upon the basal plane. Where two dissimilarly-sited islands coalesce, the grain boundary is irregular; this defect is called a dual or double position boundary (DPB) [91, 92].

The most numerous type of structural defect in GaN is the dislocation [78, 93]. Dislocations are caused by stresses inherent in the growth of a GaN film upon a substrate of a different lattice parameter. For basal-plane sapphire and silicon carbide, the two most common substrates, the a lattice parameter is the determinant of the degree of stress in the overlying film. This stress is relaxed by the formation of threading dislocations, as well as screw dislocations common to rotating-disk reactors [92, 94]. These dislocations start at the sapphire/GaN or SiC/GaN heterointerface and propagate through the film approximately in the (0001) direction. Threading dislocations are typically pure edge dislocations in GaN, with Burgers vectors of $1/3 \langle 11\bar{2}0 \rangle$ [95]. Dislocation densities on sapphire are typically in the 10^9 to $10^{10}/\text{cm}^2$ range [95-97], and in the best films are less than $10^7/\text{cm}^2$ [98].

Microtwins are large-domain crystalline defects formed due to an applied stress on a crystal. Instead of cracking or slipping, the crystal spontaneously reorients some crystallites into mirror images (Fig. 2-10). This behavior is often found at grain boundaries.

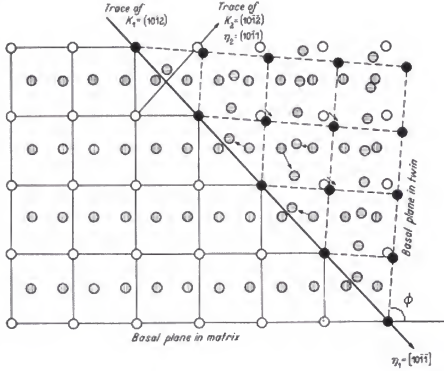


Fig. 2-10. Twin in a hexagonal crystal [99].

The orientational relationship between the twins depends upon the structural archetype of the crystal and the crystalline lattice parameter. For a hexagonal crystal such as GaN, the shear planes are of family $\{1-210\}$ and the twinning planes are $\{10-12\}$. The angle between the basal, or (0001) plane and the basal plane of the twins is given by the expression

$$\cos \phi = \frac{Hh + Kk + \frac{1}{2}(Hk + Kh) + \frac{3}{4} \frac{a^2}{c^2} Ll}{(H^2 + K^2 + HK + \frac{3}{4} \frac{a^2}{c^2} L^2)^{\frac{1}{2}} (h^2 + k^2 + hk + \frac{3}{4} \frac{a^2}{c^2} l^2)^{\frac{1}{2}}} \quad (2-1)$$

where $h, k, l, H, K,$ and L are the Miller indices for the given planes, and a and c are the lattice parameters for the hexagonal crystal [99]. For gallium nitride, which has lattice parameters of $a = 3.189 \text{ \AA}$ and $c = 5.185 \text{ \AA}$, $\phi = 81.3^\circ$.

Microcracks are cracks in the crystal structure of the film caused by a tensile stress. This tensile stress has two general causes. The first of these is a difference in lattice constant between the substrate and the grown film. If the lattice constant of the film is smaller than the lattice constant of the substrate, the atoms of the film will be distorted from their preferred lattice as each comes to rest in a low-energy configuration upon the substrate. The second cause of stress is a difference in the thermal expansion coefficient between the substrate and the film. As the wafer cools down, a substrate with a higher thermal expansion coefficient shrinks more quickly than the film, causing the film to crack once a critical stress is surpassed [73, 94, 100]. For unbuffered GaN on sapphire ($\text{GaN}/\text{Al}_2\text{O}_3$), cracking starts at thicknesses larger than $13\text{ }\mu\text{m}$ in high-quality samples, corresponding to a critical stress of $3 \times 10^8\text{ dynes/cm}^2$ [94].

Gallium Nitride Growth

Methods

Gallium nitride crystal growth can be achieved by several general techniques, including but not limited to metalorganic chemical vapor deposition (MOCVD), molecular beam epitaxy (MBE) [101], hydride vapor phase epitaxy (HVPE), atomic layer epitaxy (ALE) [102-104], pulsed laser deposition [105], supersonic arcjet plasma deposition [106, 107], sublimation sandwich growth [108], and high-pressure solution growth [109, 110]. The first four methods, and especially the first two, are the most widely used.

Metalorganic chemical vapor deposition is a process described by the gas phase reaction at elevated temperatures of a dilute gallium metalorganic, such as

trimethylgallium (TMG) or triethylgallium (TEG), with ammonia. Typically, the process is carried out over sapphire substrates at pressures ranging between 0.1 and 1 atmosphere and at growth temperatures of 950°C or higher. High quality, mirror-smooth single crystal epilayers may be obtained at growth rates of a few (0.5 to 5) microns per hour. MOCVD is a well-understood technology, is readily scalable, and MOCVD equipment is available off-the-shelf.

Molecular beam epitaxy uses a molecular beam of gallium atoms that react with NH_3 or an N_2 plasma under high vacuum (10^{-5} Torr). Typical growth temperatures are in the range of 650°C to 850°C. MBE growth of GaN layers possess greater uniformity across the wafer and superior smoothness compared to MOCVD-grown films, but MBE has three intrinsic problems compared to MOCVD. First, the growth rate of MBE films is low, ~0.5 microns per hour, because the incident atomic flux of gallium is low. The crystal quality of MBE-grown films is lower than that of MOCVD films, due to limited surface diffusion of gallium atoms. Because the growth temperature is lower than MOCVD, these adatoms are less able to diffuse along the surface to kink sites during two-dimensional step-flow growth. This results in smaller grain sizes, and thus more mosaic spread in the crystal. Finally, surface reactions in MOCVD tend to remove impurities such as carbon. Since these reactions are not significantly present in MBE due to the low growth pressure, MBE-grown films tend to have higher levels of some impurities than MOCVD-grown films.

Hydride vapor phase epitaxy is an atmospheric-pressure gas-phase growth technique that takes place in two steps. The first step generates gallium chloride (GaCl) by passing a diluted HCl stream over a boat of liquid gallium. The HCl reacts

spontaneously at the liquid surface to form the volatile chloride, which then flows downstream. The gallium chloride then reacts with ammonia above the surface of a substrate at elevated temperatures, typically 1000 to 1100°C. The primary advantage of HVPE is its high growth rate, which may run as high as 120 microns per hour. Films are transparent, mirror-smooth, and single-crystalline, but hydride films tend to be very nonuniform across the surface of the wafer. Due to this fact, planar heterostructures are very difficult to achieve with HVPE. Additionally, p-type doping of hydride films is challenging, as is growing alloys containing aluminum.

Atomic layer epitaxy is the sequential deposition of monolayers to grow gallium nitride. The substrate is exposed to two precursors, one of which supplies gallium to the nitrogen-terminated surface, and the other, which supplies the newly-gallium-terminated surface with nitrogen. Typically, TMG and NH_3 are used as precursors. ALE is typically conducted at MBE pressures, and temperatures of 500°C to 700°C [102, 104]. The main problems with ALE as a growth technique are that the growth rate is extremely low (~0.1 to 0.3 $\mu\text{m/hr}$), and that reactant efficiency is very low compared to MOCVD [102]. ALE possesses the uniformity and smoothness characteristics of MBE films, however, while retaining the high crystal quality of MOCVD films [103, 104].

Substrates

Each of the aforementioned defect structures can either be suppressed or eliminated by growing the film on a substrate of the same material, a process called homoepitaxy. A homoepitaxial substrate improves the order of the film, which merely becomes a continuation of the substrate. This film is more optimal for electronic devices for several reasons. Nitrogen vacancies are less because there are fewer physical

imperfections from which the nitrogen may vacate. Such physical imperfections may lower the activation energy for the nitrogen to desorb from the crystal. From a process standpoint, less p-type dopant atoms are needed to compensate these donors to make insulating or p-type material.

More importantly, however, there is no structural discontinuity at the film interface to complicate the energy configurations of successive layers. Compared to heteroepitaxy on unlike substrates, the film is more relaxed because it has no incorporated stress due to lattice constant or thermal mismatch. Since there are no stresses of this sort, no stress-induced dislocations, microtwins, or microcracks. As a result, electromigration and solid-state diffusion of dopants and contact materials are suppressed, and hence short-circuits, dark-line defects, and mechanical failure are reduced. Therefore, because homoepitaxially-grown films contain fewer defects than films grown on other substrates, the resulting device structures are more reliable, of higher quality, and last longer.

The problem with gallium nitride homoepitaxy is that no true homoepitaxial substrates are commercially available. Although it is possible to commercially obtain sapphire wafers covered by several microns of epitaxial gallium nitride, and to deposit subsequent layers upon them, no free-standing gallium nitride wafers are available for purchase as substrates.

Since there are no gallium nitride substrates available, heteroepitaxy, or growth on a different substrate, must be used. Table 2-4 lists the properties of various substrates for heteroepitaxial GaN growth. The thermal expansion coefficient refers to the a-direction, perpendicular to the c-axis. The values for GaN are provided as a reference.

Table 2-4: Properties of substrate materials for gallium nitride [1, 3-5, 111].

Material	Lattice parameter (Å)		Mismatch to GaN (%)	Thermal Exp. Coeff. ($\times 10^6 \text{ K}^{-1}$)	Structure
	(a)	(c)			
GaN	3.189	5.185		5.59	Wurtzite
AlN	3.112	4.982	-2.5	4.2	Wurtzite
6H-SiC	3.08	15.12	-3.54	4.2	Wurtzite
Al ₂ O ₃	4.75	12.991	16.1	7.5	Wurtzite
ZnO	3.25	5.213	1.94	2.9	Wurtzite
LAO	3.134	5.1687	-1.85	7.61	Tetragonal
LGO	3.186	5.007	-0.1	6	Orthorhombic

Table 2-5. Substrates used for hydride VPE growth.

Substrate	Notes	References
(0001) [C-plane] Sapphire	Logan: solution gradient growth	20, 26-31, 35-48, 61, 63, 73, 85-86, 94, 100, 112-124
(1-102) Sapphire		26-27, 29, 36, 40, 44
(11-20) Sapphire		124
(01-10) Sapphire		46
(10-12) Sapphire		74
Sapphire hemisphere		49
(111) Si		115, 125
(111) GaAs		125, 126
a-SiC		77, 118, 127-129
(001) LGO (LiGaO ₂)		130-132
(100) LAO (LiAlO ₂)		130-132

From these requirements, the substrate of choice for gallium nitride growth is sapphire. Sapphire produces single crystalline, hexagonal, gallium nitride epilayers. It is thermally and chemically stable, is available in bulk quantities of single crystalline wafers, and is relatively inexpensive. Unfortunately, as detailed above, films grown upon unadulterated sapphire possess high concentrations of defects, due to stresses generated from lattice constant and thermal expansion coefficient mismatch. Solutions have been engineered to circumvent this problem, but all compare unfavorably to homoepitaxy. A comprehensive list of substrates which have been used by researchers for hydride vapor phase epitaxy (HVPE) growth is given in Table 2-5.

Layers on Lithium Gallium Oxide Substrates

Lithium gallate (LGO), LiGaO_2 , is an orthorhombic crystal viewed as a potential substrate material for gallium nitride deposition. Three factors favor the use of LGO substrates when compared to sapphire. Gallium nitride grown on (001) LGO is hexagonal and single-crystalline. Lithium gallate is easily etched in common acids, providing a route for free-standing wafer fabrication. Most importantly for crystal growth, the lattice constants and thermal expansion coefficients for LGO are within 0.2% and 10%, respectively, of the values for GaN. This directly results in a reduction of stress at the heterointerface, resulting in a two-decade reduction in dislocation density, from $10^{10}/\text{cm}^2$ on sapphire, to $10^8/\text{cm}^2$ on LGO for MOCVD-grown gallium nitride. Table 2-6 lists the physical properties of LGO crystals.

Table 2-6. Physical properties of lithium gallium oxide crystals [130-135].

Property	
Lattice constant (\AA)	a: 3.186 c: 5.007
Thermal Expansion Coefficient ($\times 10^{-6}/\text{K}$)	a: 6 b: 9
Color	clear
Melting temperature	$\sim 1600^\circ\text{C}$
Structure	Orthorhombic
Solubilities	Sol. acids

Quality issues surround the LGO substrates that are commercially available, partially because bulk growth of LGO has not been perfected [133]. Routinely, substrates possess so-called “crossed line” defect structures [134, 135]. These are macroscopic streaks on the wafer surface attributed to inversion domain boundaries (IDBs). At these boundaries, the polarity of the crystal inverts from an oxygen-

terminated surface to a cation-terminated surface. This evokes concern because, the IDBs may propagate into the epilayer, and the crystal quality of epitaxial GaN will differ for the two surface terminations [136]. Furthermore, LGO crystals are very susceptible to twinning, which is an undesirable feature for a potential GaN substrate material.

A substantial amount of the GaN/LGO literature has been devoted to characterizing films grown upon the different surface terminations of LGO. Most of this work has focused upon RF-plasma MBE growth. Okada et al. have determined that stress is ~ 1 GPa lower in films grown upon the Li/Ga-terminated side of LGO than upon the O-terminated face [134]. Surface morphology, determined by SEM, improved with the cation-terminated face, as well.

Films grown upon the O-terminated side often spontaneously delaminated upon cooling from the growth temperature. Ishii suggested that nitridation of the cation surface provides an effective nucleation layer for GaN growth, and that this nitrated layer was strongly bonded to the cations, preventing any delamination [136, 137]. Reactive nitrogen did not bond well with the dangling oxygen bonds on the surface, resulting in a weakly bonded GaN film. Kryliouk and coworkers investigated surface nitridation using NH_3 , which confirmed this supposition [111, 138, 139]. Ammonia was able to change the surface of the O-terminated side to form an as-yet unidentified phase, speculated to be a Li-Ga-O-N quaternary compound. This compound formed an amorphous or nanocrystalline layer between film and bulk substrate, and therefore became the nucleation layer.

Despite these problems, both MBE and MOCVD techniques have grown epitaxial gallium nitride films on LGO substrates. Unless otherwise noted, MBE results from

Doolittle and Matyi, Johnson, and Tazoh and Ishii refer to films grown upon the Li/Ga cation-terminated surfaces [133, 137-137, 143-145, 147]. Characterization of these films has been undertaken to quantify their surface morphology, XRD, PL/CL, and electrical properties.

Surface morphology, examined by AFM and SEM, indicated improvement over sapphire substrates for MBE samples [134, 140]. In further comparison, MOCVD samples grown by Kryliouk demonstrated planar surface morphologies by AFM ($r_{\text{rms}}=0.036$ nm), indicative of step-mode growth. This value is significantly superior to sapphire films grown under similar growth conditions [111, 138, 139].

Crystal quality for films was generally reported as the full-width at half-maximum (FWHM) of the (0002) reflection of the wurtzite GaN peak. In all cases in the literature, the GaN/LGO epilayers showed a narrower FWHM than did the GaN/Al₂O₃ epilayers. In a similar fashion to GaN/Al₂O₃, the general trend was a decrease in the FWHM of the (0002) GaN peak with increasing epilayers thickness. The narrowest FWHM in the literature is from this group, a value of 21.6 arcsec, which is close to the theoretical minimum of ~20 arcsec. A comprehensive survey of the literature is shown in Figure 2-11.

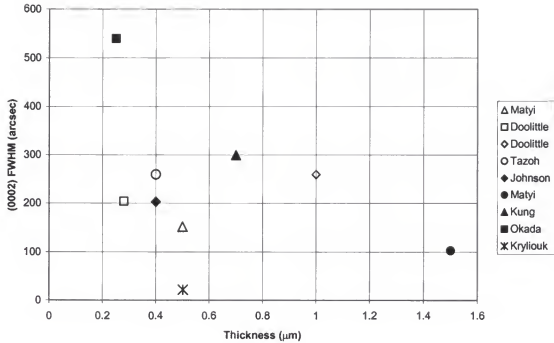


Fig. 2-11. Full-width at half-maximum for various GaN epilayer thicknesses. From references [111, 133-147].

Finally, only two groups have reported mobilities and carrier concentrations for GaN films grown upon LGO substrates. Doolittle and coworkers reported a room-temperature mobility of $43 \text{ cm}^2/\text{V-s}$ and n-type carrier concentration of $1.3 \times 10^{18}/\text{cm}^3$ for undoped MBE films [147]. Si-doped films possessed a 77K mobility of $31 \text{ cm}^2/\text{V-s}$, a room-temperature mobility of $103 \text{ cm}^2/\text{V-s}$, and a room-temperature carrier concentration of $7.8 \times 10^{17}/\text{cm}^3$. The only MOCVD results reported were from Kung, which were a mobility of $10 \text{ cm}^2/\text{V-s}$, and an n-type carrier concentration of about $1 \times 10^{20}/\text{cm}^3$ [142]. These MBE values compare unfavorably to standard MOCVD films (which possess nominal mobilities above $100 \text{ cm}^2/\text{V-s}$, and $n \sim 10^{16}/\text{cm}^3$), while Kung's MOCVD values are poor.

Gallium Nitride Substrate Growth

Historical efforts

Researchers have attempted to manufacture thick gallium nitride crystals by several techniques. Juza and Hahn attempted direct nitridation of gallium metal at 1200°C but were only able to obtain needles sufficient to investigate physical properties [148, 149]. Isherwood and Wickenden attempted to nitride gallium arsenide substrates by flowing NH_3 at high temperature, but the subsequent film growth turned out to be polycrystalline [150]. Grimmeiss et al. tried to directly reduce a lithium-gallium alloy [19]. Lorenz and Binkowski also attempted the high-temperature reduction of Ga_2O_3 by NH_3 [151]. These experiments resulted in polycrystalline gallium nitride. Several researchers attempted solution growth of GaN at high temperature and pressure from a nitrogen-saturated gallium melt. This technique was plagued by very low growth rates (~1 mm/day), and it was difficult to reproducibly get single-crystalline film [7, 152].

Maruska, using a variation of the hydride technique commonly used to grow gallium arsenide and indium phosphide for infrared devices, grew the first single-crystalline gallium nitride. This technique is essentially a two-reaction growth technique [1, 153].



The first reaction generates a volatile chloride of the metal of interest by flowing HCl over a boat of the molten metal. The second reaction, which takes place at the wafer surface, reacts this volatile chloride with the hydride of the group V element to produce the III-V material, in this case, gallium nitride [29].

After Maruska grew the first single-crystalline film by hydride VPE, a few researchers attempted to use this high growth rate technique to grow thick GaN films upon sapphire to produce free-standing GaN substrates [72]. Their objective was to use chemical-mechanical polishing to grind away the sapphire, leaving the free-standing wafer for use as a substrate for subsequent higher-quality GaN thin film growth. Thick, single-crystalline film was grown successfully, but the films grown upon these substrates, while of high quality, were still not good enough to fabricate lasers. LEDs could be produced, and were, but doping problems still proved to be the bane of volume production. This avenue of inquiry ebbed with the rest of gallium nitride research in the middle 1970s.

Current approaches

There are three current approaches toward producing substrates for gallium nitride laser devices. Two of them are pseudo-bulk CVD that adapt sapphire substrates to produce low dislocation density, single crystalline epitaxial gallium nitride films.

The first approach uses hydride vapor phase epitaxy to grow thick gallium nitride films on sapphire. As the films grow, threading dislocations self-annihilate with increasing thickness, leading to a film with a lower dislocation density farther from the GaN/sapphire interface. This film can then be planarized and subsequent film growth conducted for electroluminescent device production.

The second approach toward making gallium nitride EL devices, epitaxial lateral overgrowth (ELOG), takes advantage of the high lateral $\langle 1-100 \rangle$ growth rates of GaN to coalesce nearly dislocation-free epilayers. Gallium nitride is grown on top of stripes of SiO₂ selectively deposited upon either bare sapphire or a thin GaN/sapphire epilayer. The windows of the pattern form columns of gallium nitride, which grow together from

the sides when their height surpasses the height of the SiO_2 stripes. Since dislocations propagate primarily along (0001) in GaN, film grown laterally from the sides of these columns is essentially dislocation-free. Devices may then be reliably grown on the stripe regions of the substrate.

The third approach is a true bulk technique, employing near-equilibrium growth from a nitrogen-saturated gallium melt. Nitrogen is bubbled through a gallium melt at high temperature and high pressure near the liquidus equilibrium condition. Crystal growth starts with a GaN seed, usually a freestanding needle. Gallium nitride then proceeds to grow at the solid-melt interface, conceptually similar to Bridgeman growth of GaAs.

Hydride techniques

The first technology for substrate production begins with hydride growth of thick gallium nitride films on sapphire. This technique exists in two major variants. These are chemical-mechanical polishing (CMP) of thick hydride layers to planarize the surface for subsequent MOCVD growth, and using a zinc oxide (ZnO) buffer layer followed by acid immersion to separate the film.

HVPE/CMP: The first hydride approach toward creating substrates for laser device production involves the growth, and subsequent planarization, of a several-hundred micron thick layer of gallium nitride on sapphire. As the film grows, threading dislocations annihilate in pairs, which increases the structural quality of the epilayer. The ultimate step in the sequence is chemical-mechanical polishing with molten KOH or

boiling H_3PO_4 to provide a smooth, dislocation-sparse surface. After this planarization, device structures would be grown, likely by MOCVD, on top of the smoothed layer.

Most of the research for this technique has been directed toward optimizing the structural and electrical properties of the bulk film. Several researchers, most notably Keuch and coworkers at the University of Wisconsin, have investigated the relationship between common growth parameters and crystal structural quality. Temperature, V/III ratio, mixing zone length (wafer position), and N_2 buffer flow rates were varied, and the effects upon the structural and electrical properties of the crystal were examined.

Researchers have investigated the importance of high growth temperature for gallium nitride films. Lee reported that films grown on a- Al_2O_3 and c- Al_2O_3 were polycrystalline below 960°C and single crystalline at 980°C and above [154], although this result conflicts with this researcher's growth of single-crystalline GaN on c-plane sapphire. Both Lee and Molnar reported that higher growth temperatures resulted in a transition from three-dimensional growth below $\sim 960^\circ\text{C}$ to truncated pyramids and ultimately step-flow growth above 980°C [89, 154, 155]. For these reasons, GaN film growths using the hydride process were typically performed at a growth temperature of 1000°C to 1100°C .

Safvi et al. experimented with changing the wafer positioning in the growth zone of the reactor [156-158]. At distances close to the inlet nozzle, the resulting film was polycrystalline at the center of the wafer, due to poor mixing of the NH_3 and GaCl streams. Computational fluid dynamics calculations showed that the local V/III ratio at the center was 25% that of the edge, too low for single crystalline growth. With longer

mixing zones, the NH_3 became more homogenous across the surface of the wafer, and the resulting X-ray diffraction FWHM improved correspondingly.

This group also investigated other mass transport properties of hot-wall hydride reactors. Longer mixing zones improved the lateral uniformity of the film, from $\pm 300\%$ to $\pm 100\%$ from center to edge [156-158]. Overall growth rates decreased, however due to parasitic deposition on the reactor walls. Increasing the nitrogen buffer flow rate minimized these reactions, maximizing growth rate and uniformity. The authors concluded that reactor velocities should be high enough to suppress wall deposition upstream, while permitting NH_3 to diffuse across the wafer surface. Furthermore, a balance should be determined between wafer uniformity and structural quality on one hand, and desired growth rate on the other.

Several researchers have associated improved crystalline properties with thicker films and higher growth rates [159-163]. As distance from the $\text{GaN}/\text{Al}_2\text{O}_3$ heterointerface increased, dislocations tended to annihilate in pairs, thereby improving the quality of the overlying crystal [162]. This manifested in isotopically narrower X-ray FWHM of both the ω - and $\theta/2\theta$ -scans with increased thickness of several hydride films [164]. Omega-scans of films a few μm thick had 1000 to 3000 arcsec FWHM, while 300 μm thicknesses had 300 to 500 arcsec FWHM. For $\theta/2\theta$ -scans, these values narrowed from ~ 250 to 200 arcsec. Reciprocal lattice maps also indicated narrower features across the wafer surface for thicker films [161].

Götz [165] termed the heavily faulted region at the sapphire interface an "autobuffer layer." This autobuffer effect also manifested in DLTS and Hall measurements of several different thicknesses of $\text{GaN}/\text{Al}_2\text{O}_3$ films. Donor concentrations

near the surface of thicker films measured on the order of $10^{17}/\text{cm}^3$, while thin ($1.2\ \mu\text{m}$) films possessed donor concentrations of $10^{20}/\text{cm}^3$ [165]. The origin of these donors could not be assigned. SIMS measurements of films grown at 1050°C demonstrated O donor concentrations of $8 \times 10^{17}/\text{cm}^3$ in the bulk, which increased to $2 \times 10^{18}/\text{cm}^3$ at the GaN/ Al_2O_3 interface. While significant, this could not account for the total donor concentration. Other impurities incorporated into the film included Si ($\sim 3 \times 10^{17}/\text{cm}^3$), F ($\leq 1 \times 10^{15}/\text{cm}^3$), C ($\sim 1 \times 10^{16}/\text{cm}^3$), and Cl ($\sim 2 \times 10^{16}/\text{cm}^3$) [154, 165].

Photoluminescence results, usually reported for the bound acceptor peak at 3.47 eV, varied widely with temperature for hydride films of various research groups. Lee reported a FWHM of the peak of 29 meV at 77K [154]. Skromme performed 2K PL of hydride films and reported a FWHM of 2 meV [166]. Naniwae measured the same peak at 4.2K for several film thicknesses and reported values ranging between 1.5 to 2.5 meV. PL measurement at 7K of Perkins's films yielded values near 10 meV [156].

To demonstrate the applicability of the conventional hydride process for the production of GaN substrates for subsequent epitaxial growth, Molnar and coworkers mechanically polished $15\ \mu\text{m}$ thick HVPE films to a final thickness of $8\ \mu\text{m}$ [155, 168]. These were then chemically cleaned and etched, and an $\text{Al}_{0.1}\text{Ga}_{0.9}\text{N}/\text{GaN}$ double heterostructure was grown on top by MBE. Active layer thicknesses were either $1000\ \text{\AA}$ or $4000\ \text{\AA}$. Upon illumination with a Nd:YAG laser emitting at 266 nm, PL of these structures displayed a threshold fluence, and linear dependence of the PL intensity above this fluence level, indicative of optically-pumped stimulated emission. 77K PL showed cavity mode emission, with five modes visible. External quantum efficiency was estimated to be 1%. While a low figure, this result demonstrated the utility of

conventional HVPE followed by CMP for the production of GaN substrates for subsequent LD and LED fabrication.

The second hydride technique uses a zinc oxide (ZnO) buffer layer between the sapphire substrate and the gallium nitride film. This serves two purposes. The buffer layer acts as a stress reducing intermediate layer, because the lattice constant of ZnO is 3.2496 Å, much closer to that of GaN (3.189 Å) than that of sapphire. This directly improves the physical and electrical properties of the film. The ZnO buffer also serves as a sacrificial detachment layer after the thick gallium nitride film is grown. Immersion of the GaN/ZnO/sapphire heterostructure in an acid, such as HCl, permits separation of the GaN thick film from the sapphire, which may be reused.

Detchprohm et al. from Nagoya University in Japan first described the ZnO technique in 1993 [169]. Buffer layers with thicknesses ranging from 0.1 to 1.0 mm were sputtered in Ar, O₂, and 50% Ar/50% O₂ ambients. The O₂ ambient was found to produce nearly single-crystal ZnO, superior in quality to the other ambients. A buffer layer thickness of 0.4 mm was found to be a threshold thickness. Above this value, millimeter-scale abnormal features are present; however, the rest of the film displayed blue light emission at 2.809 eV when optically pumped by a 325 nm He-Cd laser. Below the 0.4 mm limit, no growth abnormalities were present, but no blue Zn-related emission could be observed. This suggested that the ZnO thermally desorbed prior to growth. All films had significant, visible cracking, which originated near the sapphire surface.

Attempts to separate the GaN film from the sapphire substrate met with varying success; often films could not be easily peeled off, and required delamination with forceps [169]. Damage to the surface of the samples due to peeling was "fairly severe" at

the sapphire/GaN interface, although whether this referred to the mechanical removal of the thick film or to peeling from thermal or lattice stresses is unclear [170]. Typical free-standing films had dimensions of 4 x 2 mm.

Some of these films were later used as substrates for MOCVD growth [170, 171]. Mg-doped layers of various concentrations were grown at temperatures ranging from 1050 to 1100°C. Photoluminescence (PL) and cathodoluminescence (CL) were performed on these films. CL indicated a strong blue peak at 445 nm for high ($2 \times 10^{20} \text{ cm}^{-3}$) acceptor concentrations, and a strong violet peak at 400 nm for low ($7 \times 10^{19} \text{ cm}^{-3}$ to $1 \times 10^{20} \text{ cm}^{-3}$) acceptor concentrations. Both of these peaks were attributed to Mg. The films needed neither thermal annealing nor low-energy electron beam irradiation (LEEBI) to activate the donors, but LEEBI dramatically improved the room temperature PL intensity of films with low Mg concentrations. No mention was made regarding Mg activation treatments for the heavily doped films [170]. Contacts were evaporated onto each side and LEDs were formed. These devices rectified as classic p-n junctions when C-V profiling was done, and showed a breakdown voltage of approximately 8 V [171].

Other free-standing films were used to investigate the excitonic spectrum of gallium nitride. Meyer used FTIR to resolve the donor-acceptor (DA) and band-acceptor (eA) transitions, and from absorbance measurements calculate effective masses for shallow donors of (35.5 +/- 0.5) meV and for electrons of (0.236 +/- 0.005) m_0 [172]. Volm and Meyer also used high (12 T) magnetic fields to resolve Zeeman splitting and anisotropy of the donor bound exciton at 3.473 eV. They found spin splitting in the PL spectrum when the magnetic field was perpendicular to the c-axis of gallium nitride, but no effect when it was parallel to the c-axis [124, 173].

The Nagoya group found that burial of the side surface of the sapphire under the thick gallium nitride film contributed to the difficulty with delamination. To improve this process, they masked a 1 mm border at the edges of the substrate with an SiO_2 mask. While no crystal growth took place on the masked-off areas, thus preventing burial of the edges, no separation of the film from the substrate was reported. No explanation was given. This group later abandoned this technology due to repeatability problems [174].

Molnar et al. from MIT Lincoln Labs and Xerox Palo Alto compared the ZnO buffer layer treatment with a GaCl growth pretreatment developed by Naniwae to optimize the electrical and structural characteristics of the grown films [162, 163, 175, 176]. No substrate separations were attempted, possibly because they discovered from TEM micrographs that under their growth conditions, the buffer layer had thermochemically desorbed prior to growth. They found comparable mobility results for the ZnO buffer and GaCl pretreatments, with the GaCl treatment exhibiting an RT electron mobility of $124 \text{ cm}^2/\text{V-s}$ (vs. 93 for ZnO), but the GaCl demonstrated an inferior RT donor concentration of $1 \times 10^{19}/\text{cm}^3$ (vs. $1.7 \times 10^{17}/\text{cm}^3$ for ZnO) [89]. In subsequent films, the ZnO treatment clearly yielded better electrical properties, with a carrier concentration of $1.4 \times 10^{17}/\text{cm}^3$ and a carrier mobility of $768 \text{ cm}^2/\text{V-s}$ at RT [163, 175].

Photoluminescence results on these high-quality films showed an intense donor-bound exciton (BX) peak at 3.468 eV. The authors rejected the accepted belief that this peak served as an indicator of crystal structural or electrical quality, because the lowest-defect-density, highest-mobility sample demonstrated the broadest FWHM of this peak [176]. XRD of these films showed a $\Delta\omega$ of 4.5° for the (002) peak of GaN, which measured tilt, and a $\Delta\phi$ of 11 minutes for the (112) peak, which measured twist. Theta

rocking curve FWHM ranged between 4.8 and 7.2 arcmin. AFM demonstrated step-flow growth [162].

Efforts were made to control the initial stages of growth so that ZnO remained after epitaxial growth began. By accomplishing this, several small ($\sim 10 \text{ mm}^2$) free-standing flakes of GaN were produced, but the size of the flakes were limited by thermal cracking [155].

Ueda has also attempted to use a single-crystalline ZnO buffer layer, deposited by pulsed laser deposition, in an attempt to improve the structural quality of the GaN epilayers [177]. While thin (25 nm) buffer layers significantly improved the surface morphology of the film, a 200 nm buffer layer resulted in cracking and peeling. Growth on unbuffered sapphire resulted in polycrystalline film with mixed (0001) and (11-21) character. The FWHM of the (0002) GaN reflection was plotted against buffer layer thickness, and passed through a minimum of 0.45 degrees for a 50 nm thick ZnO buffer layer. Based upon this result, Ueda speculated that the ZnO buffer layer remained, although no direct confirmation was available at the time. The authors further suggested that a single-crystalline buffer layer would have a lower desorption rate than a sputtered buffer layer. No electrical properties were reported for their films.

Epitaxial lateral overgrowth

The second technology for the production of substrates for optoelectronic devices uses a selective area growth method called epitaxial lateral overgrowth (ELOG) to decrease the dislocation density of films on sapphire substrates. A several-micron thickness of (0001) gallium nitride is grown on (0001) sapphire by MOCVD. On top of

this, a series of lines of silicon dioxide (SiO_2) are deposited. MOCVD gallium nitride is deposited into the windows of the SiO_2 mask, and columns of GaN are grown. The column walls become (1-100) faceted, because growth in the basal direction is slowest, and start to grow laterally. These columns are permitted to completely grow together in order to again form an uninterrupted film.

As previously mentioned, dislocations in GaN tend to propagate in the (0001) direction. They do not continue into the laterally overgrown region. Furthermore, because lateral film growth along the walls of the column occurs upon a free surface of GaN, no stress-related defects are generated. As a result, the crystalline quality of the GaN in the overgrown region is exceptionally high. Dislocation density plummets from a concentration of order $10^{10}/\text{cm}^2$ in the volume below the SiO_2 to $10^7/\text{cm}^2$ in the window region. In the laterally overgrown region, the dislocation density was “almost zero,” according to Nakamura, and later measured by TEM to be near $10^5/\text{cm}^2$ [178, 179].

This low dislocation density further improves the electrical and optical properties in the region. Singh et al. measured carrier concentrations of 10^{17} to $10^{18}/\text{cm}^3$ for a geometry of 100 μm diameter windows on 500 μm centers [180]. Room temperature PL for their films demonstrated a peak emission at 361 nm with a FWHM of 12.5 nm at room temperature. Optical pumping with a 337 nm nitrogen laser exhibited a threshold incident power for stimulated emission of $3.4 \text{ mW}/\text{cm}^2$.

Nakamura's geometry of 10 μm SiO_2 stripes with 3 μm windows lased by carrier injection at a threshold voltage of 6V and a threshold current density of $5 \text{ kA}/\text{cm}^2$ [178]. The area of the LD was 3 μm x 450 μm . The emission spectrum at 1 mW showed numerous well-defined cavity modes from 406 to 411 nm, and transformed to single-

mode emission at 408.6 and 409.1 nm for input powers of 5 and 10 mW, respectively. Furthermore, at a current of 200 mA, the LD lased at an output power of 90 mW, which was the highest value reported at the time, for room temperature continuous-wave operation.

Three main drawbacks to this technique exist. Laser devices produced by ELOG come from the laterally overgrown areas of the wafer. This limits the usable area of the sapphire substrate to the area covered by the SiO_2 stripes. The window region is not useful for making LDs, because of high dislocation concentrations. This forestalls lasing action, and decreases LD lifetimes and reliability. For Nakamura's patterns, at most 77% of the wafer may be used to make devices. Some of this inefficiency may be regained by using the window areas as traces for the dicing saw, but this will still be less efficient than fabricating lasers directly upon GaN substrates.

The second drawback to ELOG arises from making contacts to the device. Substrates of silicon and gallium arsenide can be conducting, which means that contacts can be formed directly on the reverse side of the wafer. Then, attachment of leads to the top and bottom of the wafer and encapsulation are all that is necessary to finish the device. By contrast, sapphire is an insulating material. Both anode and cathode contacts therefore must be formed on the same side of the wafer in the ELOG.

Because of this geometry, the resistance near the anode affects the design. The entire current flows through a relatively narrow strip near the surface of the anode. If the current is too great, the resistance will increase with temperature, requiring higher drive voltages for the same luminosity. Too little current—or voltage—will prevent the device from reaching the lasing threshold. Furthermore, this current channeling can lead to

device failure if the crystal becomes hot enough for aluminum atoms to migrate from the anode into the crystal. In contrast, geometry matters less for the typical DH laser with top-and-bottom contacts. Electrons have a much wider channel through which to flow, eliminating carrier crowding resistances in the device.

Formation of the contacts also creates the third problem with the ELOG technique. ELOG demands the selective sacrificial etch of tens of microns of material from the sides adjacent to the device. Metallic deposition steps then follow these steps, typically Ni/Au for the cathode and Al/Ti for the anode, to form the actual contacts. Due to the etching requirement, this technique requires more fabrication steps. Cluster tools for photomasking and lithography and wet/dry etching, and SiO₂ deposition must be added to the CVD process line. This represents a significant capital investment, and more manufacturing steps reduce wafer throughput and increase production scheduling complexity.

Despite its inefficient use of the wafer surface, and more difficult fabrication, the ELOG technique is currently the only method to have produced carrier injection lasers. For now, it is the only industrial production method for lasers based upon gallium nitride.

High-pressure solution growth

The bulk technique perfected by Porowski uses a seed crystal of GaN in a gallium melt through which nitrogen is bubbled under high temperature and pressure. Gallium nitride then forms at the heterointerface due to the Gibbs energy differential between nitrogen in the bulk solution and at the growth surface. The theory is similar to horizontal Bridgeman growth of GaAs crystals. Typical growth temperature is 1500 to

2000°C, and typical pressure is 1 to 2 GPa. This method is used to produce large (7 mm x 7 mm) single-crystal plates of GaN [109].

The structural quality of crystals grown by the high-temperature, high-pressure method was excellent. Omega X-ray rocking curves were reported as narrow as 30 to 40 arcsec for 0.1 mm to 2 mm undoped crystals, and as narrow as 20 to 30 arcsec for Mg-doped films [110, 181-184]. Larger samples displayed wider Bragg peaks (1 to 3 arcmin) and split peaks, indicative of low-angle grain boundaries [109]. TEM performed on these samples exhibited a dislocation density of 10^3 to $10^5/\text{cm}^2$ [109, 185, 186].

Electrical characterization of these films displayed mobilities in the range from 30 to $100 \text{ cm}^2/\text{V-s}$ and carrier concentrations between 10^{19} and $10^{20}/\text{cm}^3$ for undoped films [181, 183, 185, 187-190]. Photoluminescence and electroluminescence of these films generally showed a strong, broad near-band-edge peak at 3.468 eV attributed to an exciton bound to a neutral donor. A peak corresponding to parasitic yellow luminescence was present at 2.2 to 2.4 eV in most samples [183, 190, 191].

Films were later grown upon these substrates using both MBE and MOCVD techniques. Several papers reported upon the differences in physical properties between the substrates, which typically had donor concentrations of $1 \times 10^{20}/\text{cm}^3$, and the epilayers, which were grown under the same conditions as films grown upon sapphire that had donor concentrations of $\sim 10^{17}/\text{cm}^3$. Due to the fact that the highly conductive substrate provides a parallel path for electron transport, epilayer carrier concentrations could not be directly determined by Hall-effect measurements.

Suski and coworkers investigated the difference in lattice parameters between substrate and MBE-grown epilayer, and found that the *a*-lattice constant was 0.02%

smaller for the epilayer when compared to the bulk lattice constant [183, 189]. As a result, the epilayer and the substrate, while the same material, presented separate peaks when X-ray diffraction was performed upon them. This effect can be attributed to a lattice constant variation with donor concentration for GaN [35, 164, 192]. If a smaller donor concentration were to be achieved, even this relatively small mismatch could be eliminated. A FWHM of 30 to 40 arcsec was measured for these films, one of the lowest ever reported. This result confirmed the desirability of GaN substrates for homoepitaxial growth.

Optical characterization of these films was performed by 4.2K and room-temperature PL. A strong near-band-edge peak at 3.467 eV was reported and was assigned to an exciton bound to a neutral donor [191]. This peak had a FWHM of 16 meV, much higher than most MOCVD results [155, 167, 173, 193].

Baranowski investigated the MOCVD growth of GaN on GaN substrates grown by the high T, high P method [183]. Films were grown at temperatures ranging from 800 to 1050°C, and upon both N-terminated and Ga-terminated surface polarities. AFM showed that at typical growth temperatures, the initially smooth N-terminated surface became rough, and the initially rough Ga-terminated became smooth. Furthermore, the film grown upon the surface generally retained the polarity of its substrate, although occasional inversion domains were seen by TEM. PL performed upon these films showed that the intensity of the 3.47 eV near-band-edge emission was much sharper for the Ga-terminated side than the N-terminated one. The PL of the latter possessed a single very broad peak with half-maxima at 3.43 and 3.54 eV, as well as strong yellow luminescence absent from the Ga-terminated film [182, 183, 192]. When Mg doping of

the epilayer was attempted, the FWHM of the exciton-donor and exciton-acceptor lines were measured by 4.2K PL to be 0.5 meV. This figure was one-third the width of typical PL [155, 167, 173, 193].

Pelzmann reported on blue light LEDs homoepitaxially fabricated upon GaN produced by the high pressure, high temperature method [186]. The substrates were undoped, having native donor concentrations of 10^{19} , dislocation densities of 10^3 to $10^5/\text{cm}^2$ and a FWHM of the (0002) GaN peak of 30 to 40 arcsec. I-V profiling was handicapped by poor contact with the p-type material, but a drive voltage of $\sim 4\text{V}$ was reported. EL demonstrated a single intense peak at 420 nm, twice as bright as a heteroepitaxial LED fabricated on sapphire under the same growth conditions. The heterostructure LED, on the other hand, peaked at a more desirable wavelength of 384 nm, in the near-UV.

While this technique offers an avenue for the production of bulk single crystals, several problems must be overcome or circumvented. To date, only small crystals have been grown, the largest being 50 mm^2 . The current benchmark for wafer size in nitride semiconductors is two inches in diameter. Scale-up for the high-pressure, high-temperature process is more difficult than for chemical or physical vapor deposition [155]. This is due to the fact that the pressure chamber requires redesign and major manufacture to accommodate larger crucible sizes, while CVD techniques typically require only redesign of the reactor and off-the-shelf ancillary equipment to produce larger substrates. Furthermore, ingots can only be produced individually, while vapor deposition techniques permit batches of several wafers per growth run. This lack of scalability hinders development of this technology as a true volume production technique.

Growth rates are very low for the solution technique, compared to other melt techniques, such as CZ growth of silicon or Bridgeman growth of gallium arsenide. A 6 mm x 6 mm crystal took 150 hours to produce [185]. The growth rate in the [1-100] directions was the fastest, at 20 $\mu\text{m/hr}$. This growth rate is comparable to hydride vapor phase epitaxy. The growth rate may be increased by increasing the thermodynamic driving force via increasing the temperature gradient across the solid-liquid interface, but at higher growth rates, the boule becomes polycrystalline [185, 187]. With further increases in temperature gradient, the crystal growth becomes unconstrained, introducing voids and dendrites in the as-grown crystal. Such gross imperfections prohibit the use of these crystals as substrates.

The electrical properties of the crystals grown by the solution technique also present a concern, because the concentration of donors is very high compared to other techniques. Donor concentrations of $10^{20}/\text{cm}^3$ are typical. This may be caused by oxygen contamination in either the growth crucible or the nitrogen stream. Oxygen concentrations of 10^{19} to $10^{20}/\text{cm}^3$ were reported by Suski, Perlin and associates [188, 189, 194]. Other impurities included hydrogen ($\sim 4 \times 10^{17}/\text{cm}^3$), carbon ($3 \times 10^{19}/\text{cm}^3$), and silicon (1×10^{17}) [194]. Whether or not this is an inherent problem is not clear at this time.

Gallium Nitride Photonic Devices

Light-Emitting Diodes

A light-emitting diode (LED) is an electronic device that produces photons of light upon application of an electric field. Although there are several archetypes of LED, the simplest and most common type is the p-n homojunction diode (Fig. 2-12). A semiconducting material is doped n-type in one region of the material, and in an adjacent region of the material, doping is made p-type. The n-type region has an excess of electrons, and the p-type region has an excess of holes. At the interface between the two regions, the carriers combine, forming a region of no space-charge called the depletion region. An electric field is present, created by the separation of negative charge on one side of the depletion region and positive charge on the other side [23, 195].

In nominally-undoped gallium nitride, the majority carriers are electrons. Upon application to the diode of a forward current or forward-bias, in which a positive voltage is applied from the p-type region to the n-type region, electrons are injected from the n-type region into the p-type region, and recombine at or near the interface (Fig. 2-13) [36, 196, 197]. A process called impact ionization may also occur, where an electron collides with a dopant atom and imparts energy to a dopant electron. This excited dopant electron then returns to its ground state, emitting a photon [197]. Carriers typically recombine at a crystalline defect such as a dopant or impurity atom or a crystalline fault. The energy lost as the carrier falls back into its valence state is preferably emitted radiatively, in which case a photon is created, but may be lost in non-radiatively by such methods as phonon generation [21, 198].

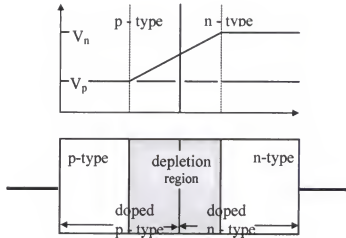


Fig. 2-12. A p-n junction, from Dalven [195].

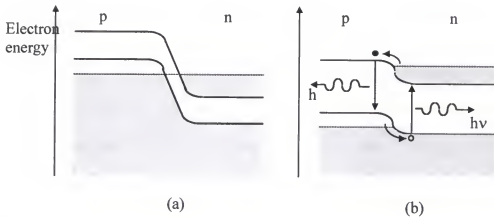


Fig. 2-13. (a) Band diagram of degenerate p-n junction at equilibrium. (b) Same junction under forward bias [195].

As a practical matter, several challenges must be overcome to successfully make a p-n homojunction LED. The material should be a direct bandgap semiconductor, with a wide enough bandgap to produce visible light (if the primary usage is in electroluminescent displays, for which most LEDs are used). The material must be able to be doped both n-type and p-type. The dopants must be able to emit photons through

radiative recombination in the material. The dopants must be made electrically active, meaning bonding in the crystal lattice in such a fashion as to contribute electrons or holes to the space-charge region in which they reside. Finally, the material must be transparent to the frequencies of light it generates [198, 199].

Furthermore, highly efficient LED operation requires a high internal quantum efficiency [21]. This is the ratio of photons produced to the number of carriers flowing through the diode. The quality of the semiconductor crystal plays a huge part in this regard. A highly defective crystal matrix will not be conducive to the radiative transitions necessary to produce light. Carriers may combine nonradiatively at imperfections, and imperfections may also reabsorb generated light [26, 50, 198]. Each of these processes generates heat, which also tends to degrade performance [200]. Higher temperatures can decrease carrier mobility, increase the probability of non-radiative transitions, enhance diffusion of impurities into the crystal causing short-circuits and dark line defects, and cause precipitation of impurities [21]. In extreme cases, phase changes or phase separation may occur in the material [201]. As a result, a high degree of crystalline perfection is required when fabricating LEDs [202-205].

Laser Devices

Solid state lasers operate upon the same principles as LEDs. The classic semiconductor laser is a double-heterostructure (DH) laser (Figure 2-14). It consists of three semiconducting layers. The center layer, or active layer, is where the lasing action takes place. Surrounding this are two layers compositionally distinct from the active layer, called the optical confinement layers. These are chosen so that the difference between the index of refraction of the active layer and that of the confinement layers

permits total (or near-total) internal reflection for the wavelength of interest. Carriers are confined to this region by the heterojunction potential barriers on both sides of the region. The cavity sides are typically cleaved into mirror facets to increase the internal reflection in the direction of lasing, and roughened on the other facets to forestall lasing in undesired directions [23].

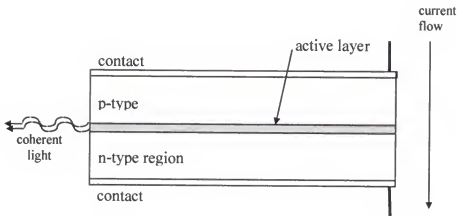


Fig. 2-14. Typical double-heterostructure laser.

Like the LED, the semiconductor laser diode (LD) generates photons by carrier recombination at the interface of the active layer and the p-type layer. This recombination generates a photon, and self-interaction between the photon and the electromagnetic field across the active layer can replicate it. These generation mechanisms are balanced out at steady state by losses from internal absorption and transmission to the environment. As in the case of the light-emitting diode, defects are the primary cause of loss within the active layer [21, 26, 50]. The higher the concentration of defects, the greater the loss, and if this prevents a population inversion from being achieved, the crystal cannot lase [21]. Essentially, such a device is an LED.

Furthermore, like LEDs, the lifetime and efficiency of LDs are inversely proportional to the concentration of defects [206]. Hence, crystal quality is imperative in semiconductor laser fabrication [207].

Gallium Nitride Device Production

Maruska's ability to grow single-crystalline gallium nitride films generated much research directed toward the production of electroluminescent devices. As listed in Table 2-2, several studies reported on a wide variety of dopants, which permitted researchers to customize LEDs by selecting the wavelength of light to be produced. Pankove created the first LED using the material in 1971. This group created a metal-insulator-semiconductor green LED using zinc as a dopant. Zinc was introduced into their reactor from a heated sidearm by direct evaporation into a hydrogen carrier gas. Later that year, the same group reported an LED which produced blue light at 2.8 eV (440 nm) [51-53]. In 1972, Maruska and co-workers used Mg as a dopant to produce the first violet light LED at 425 nm [31]. Subsequent researchers were able to boost efficiencies and luminosities, but due to problems caused by doping repeatability and marginal crystal quality, p-type films could not be repeatably achieved [41, 208, 209]. Hence, the efficient p-n homojunction LED could not be produced, and commercial production of gallium nitride LEDs was not successfully undertaken.

In 1971, Dingle and coworkers produced the first laser device in gallium nitride by using the hydride technique. Using a pulsed N₂ laser operating at 337.1 nm, they produced 4.2 K stimulated emission from GaN needles [112, 210]. Several other researchers were able to produce devices that could be optically pumped to lase, but none

were able to produce a semiconducting GaN laser which worked by current injection. A critical need was for repeatable, controllable p-type doping, and better crystal quality.

Due to the lack of successful device fabrication, research on gallium nitride ebbed in the late 1970s. But, in 1986 the field of gallium nitride research was rejuvenated by a breakthrough discovery by Amano and Akasaki of Nagoya University in Japan [75, 211]. They discovered that a very thin-- tens of nanometers thick-- buffer layer of aluminum nitride grown upon the sapphire substrate before gallium nitride growth dramatically increased the quality of the subsequently grown film. X-ray diffraction of their film showed a full-width at half-maximum (FWHM) of 2.7 arcmin for the (0006) diffraction peak of gallium nitride. This was over four times narrower than the best film reported in hydride growth, which was 12 arcmin for Shintani [212]. Furthermore, their carrier mobilities were 350 to 400 $\text{cm}^2/\text{V}\cdot\text{s}$, which (at the time) was a full order of magnitude better than the next-best films. Subsequent researchers have successfully deposited gallium nitride buffer layers at low temperature, or used sputtered zinc oxide and other materials to grow high-quality films. The immediate improvement in crystal quality that resulted from these efforts again made the prospect of a current-injected GaN laser appear to be achievable, and GaN research took on renewed interest.

One large problem remained, however-- doping GaN p-type was a challenge. The large n-type native defect concentration must be overcome, and then some, to make GaN p-type. Maruska and Tietjen, and most of the hydride researchers, attempted p-type doping using direct evaporation of the elemental dopant into the growing film. Among the problems they encountered were nonrepeatability, surface nonuniformity, lower growth rates for doped films, and a high percentage of electrically inactive dopant atoms

in the grown film. As a result, reproducible fabrication of high-quality LEDs was difficult, much less LDs.

Among the spate of research generated by the buffer layer discovery was research into p-type doping. This body of research produced three substantial findings, two of which related to procedures for activating p-type dopants. Low energy electron beam irradiation (LEEBI) of Mg-doped samples showed a two order of magnitude increase in the concentration of holes in p-type regions [213]. This enabled the fabrication of the first p-n junction LED [199].

Another technique, thermal annealing in a nitrogen or ammonia atmosphere, also increased the electrical activity of incorporated magnesium. These experiments showed that hydrogen was the culprit in the passivation of magnesium. Hydrogen incorporated with the dopant into the film formed Mg-H complexes that were electrically neutral. LEEBI broke the Mg-H bond for complexes near the surface of the film, and thermal annealing permitted the out-diffusion of hydrogen from the bulk of the film [214, 215]. Along with a more reliable delivery system, namely the use of metalorganic sources for dopants, these findings enabled repeatable doping and fine control over p-type doping procedures.

In 1996, a series of small refinements in technique resulted in the paramount achievement in GaN device manufacture. Nakamura, of Nichia Chemicals of Japan, fabricated the first gallium nitride lasers which operated strictly by carrier injection. It operated in both continuous and pulsed modes, generating monochromatic light at 417 nm [216]. Confirmation of this result was achieved in October of 1997 by a multidisciplinary group from the University of California, Santa Barbara [217].

Subsequent improvements have permitted a blue GaN LD with an estimated lifetime of over 10,000 hours, which is generally considered the threshold for commercial viability.

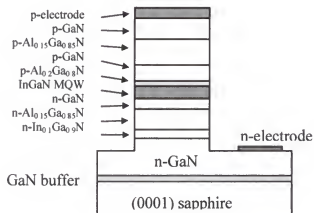


Fig. 2-15. Laser diode of Nakamura et al. [216]

CHAPTER 3

GROWTH INVESTIGATIONS OF THE HYDRIDE-METALORGANIC VAPOR PHASE EPITAXY (H-MOVPE) SYSTEM

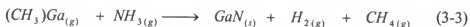
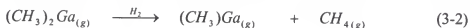
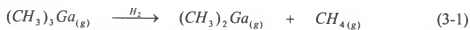
Most GaN photonic devices are formed from the highly controlled deposition of epitaxial layers in a sequential fashion using different growth recipes, like the rungs of a ladder. For GaN, often there is deposition of a thin, amorphous buffer layer of GaN or AlN, to reduce the density of dislocations in the device. This is followed by a several-micron thickness of undoped GaN before growth of the actual device layers. These subsequent device layers may be doped either n- or p-type, or they may be alloyed with aluminum or indium to form confinement or active layers. Accordingly, there exists a need for a CVD technique to provide thin, dopable, planar films for growth of device structures that is versatile enough to grow thick films and pseudobinary/ternary compounds.

The purpose of this chapter is to describe the elements of the H-MOVPE reactor system, the experimental procedures, the initial GaN growth investigations, and the subsequent parametric studies. Characterization results from growth rate measurements, low- and high-resolution XRD, AFM, AES, SIMS, and PL are presented. Finally, thickness and PL measurements from GaN experiments upon 2" diameter sapphire substrates are given.

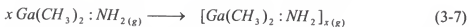
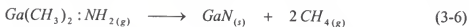
The H-MOVPE Reactor System

Chemistry

The simplest model of gas-phase GaN deposition reactions involves the decomposition of trimethylgallium (TMG) by the sequential elimination of methyl groups (Reactions 3-1 and 3-2) to produce monomethylgallium. This is followed by the surface reaction of adsorbed monomethylgallium with ammonia on the surface to form GaN (Reaction 3-3).



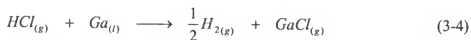
It is known that the detailed reaction mechanism is more complex and involves adduct formation [218, 219]. In this model, trimethylgallium reversibly reacts with ammonia in the gas phase to produce an adduct (Reaction 3-4). Sequential homolysis of Ga-C bonds leads to reactive dimers and adducts which deposit GaN on the surface. The adduct can then either decompose when near the substrate (the reverse reaction of Reaction 3-4), or form a thermally stable species $Ga(CH_3)_3:NH_3$ by elimination of a methane molecule (Reaction 3-5). This thermally stable adduct can either directly participate in the deposition reaction (Reaction 3-6) or oligimerize (Reaction 3-7). According to Theodoropoulos et al. [220], the decomposition of the adduct (Reaction 3-4) to give TMG which then produces GaN (according to Reactions 3-1 to 3-3) is the primary pathway and with proper reactor design all pathways involving the thermally stable adduct are relatively minor.



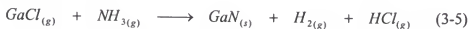
Other gas-phase and surface reactions are possible, such as desorption, free-radical formation, polymerization, crystal decomposition, and so forth, but the above reaction mechanism is believed to be the most common MOCVD reaction model. An intriguing conclusion by several groups is that the various reaction models predict nearly the same growth rates (within $\pm 10\%$) for the same reactor geometry, and the reaction models respond similarly to process variables such as reactor pressure and rotation rate [220-222].

By contrast with the MOCVD process, the HVPE process is a two-step reaction process. In the first step, HCl reacts with a liquid gallium source to form volatile GaCl. This reaction typically occurs at a temperature between 850 to 900°C. This monochloride is then transported downstream to the wafer, where it reacts with ammonia at the wafer surface to form GaN:

Monochloride formation:



Nitride formation:



The primary advantage of HVPE over MOCVD is the increase in growth rate of single-crystalline films. MOCVD growth rates generally range from 1 to 3 $\mu\text{m/hr}$ [219]. Higher MOCVD growth rates resulting from increased TMG flows produce polycrystalline film. By contrast, HVPE growth rates usually range from 10 to 40 $\mu\text{m/hr}$ [155, 170, 171, 175], depending upon reactor geometry and flow conditions, and higher growth rates are possible.

It was realized that a system that could selectively react hydrogen chloride with these metalorganics would confer the advantages of both chemistries. Research by Flemish, Jones and Ban proved that TMG (and TMI) reacts with HCl at moderate temperature to form group III chlorides [223]. Without the hydrogen chloride reaction, the growth chemistry would remain a standard GaN MOCVD system, except using a hot-wall reactor. When the hydrogen chloride was added, the metalorganic reacted to form GaCl by reaction 3-7, and effectively changed the growth chemistry from MOCVD to HVPE:



In this fashion, the high growth rate and good crystallinity features of the HVPE chemistry, which is due to the presence of chlorine, may be added to the controllability of the MOCVD chemistry to create a more robust process for nitride semiconductor growth. Several advantages accrued to this combination.

The primary advantage over MOCVD of combining these chemistries by H-MOVPE is the increase in growth rate for GaN CVD. The H-MOVPE chemistry permits growth rates of 10 to 15 $\mu\text{m/hr}$ (limited in this system by the transport rate of TMG), while typical MOCVD growth occurs at growth rates of 1 to 3 $\mu\text{m/hr}$. This enables the

growth of thick films. Furthermore, these films possess high structural quality and reduced metal impurity incorporation compared to MOCVD films. The chemistry can incorporate indium while growing in hydride mode, and both indium and aluminum in MOCVD mode.

By contrast, HVPE growth cannot incorporate aluminum into the nitride layer, due to the high thermodynamic stability of aluminum chloride. Furthermore, source transients from the initial introduction of hydrogen chloride to the HVPE gallium and/or indium sources provide inherent controllability problems, requiring novel or cumbersome physical methods to grow heterostructures. Hence, the primary advantage of the H-MOVPE method over HVPE is found in controllability.

With the appropriate reactor design, the H-MOVPE design may allow planar composition changes throughout the film in two ways. It can incorporate dopants by standard MOCVD techniques. Of perhaps more interest, however, may be its capability to grow planar heterostructures at high growth rates by adding another metalorganic (such as trimethylindium (TMI) or, in MOCVD mode, trimethylaluminum (TMA)) to the reactant stream. With the proper manifold design, two different compositions of film may be alternated at will with this method, and the abrupt junctions required for devices such as heterostructure lasers can be manufactured.

Design

From a design standpoint, there were several considerations to be made. First, the hydrogen chloride and metalorganic controls must be quickly switchable from vent to run settings. Otherwise, transients from initiating the growth would affect the critical initial layers in an uncontrollable fashion. For instance, the initial ratio of hydrogen chloride to gallium species at the wafer surface was known *a priori* to be important to crystal quality

of III-Vs. Higher ratios result in better quality film, as measured by structural perfection and electrical properties [156-158, 219]. If this ratio were to vary from film to film, as would happen if the line pressure in the bubbler were not yet steady state, the quality of the resulting epilayers would also be less controllable. Another example of the required control requirements was the possibility of alloy growth by adding intervals of indium chloride to the gallium chloride stream. This would result in $\text{In}_x\text{Ga}_{1-x}\text{N}$ growth, and would be used for confinement and/or active layers in devices. These applications require precise layer thicknesses, and therefore precise timing, of each type of growth mode.

To solve this problem, the manifold design represented in Figure 3-1 was built. The schematic shows a set of quick-switching pneumatic valves for the control of reactant flow to either the run side of the reactor, where crystal growth takes place, or to the vent side of the reactor, where reactants merely flow to the exhaust.

The NH_3 and HCl gas cylinders are located in gas cabinets attached to the system. The nitrogen or hydrogen carrier gas is supplied from individual lines from a liquid nitrogen ball (N_2) or an individual cylinder (H_2). Trimethylgallium (5N) is supplied by Epichem, and stored in bubblers located underneath the reactor benchtop. Mass flow controllers regulate reactant stream flows, and are located in a cabinet mounted adjacent to the reactor hood. The pneumatic switching valves are mounted vertically on the inside of the reactor hood. Before entering the building exhaust system, exhaust is passed through a custom dry chemical scrubber filled with copper sulfate-based resin.

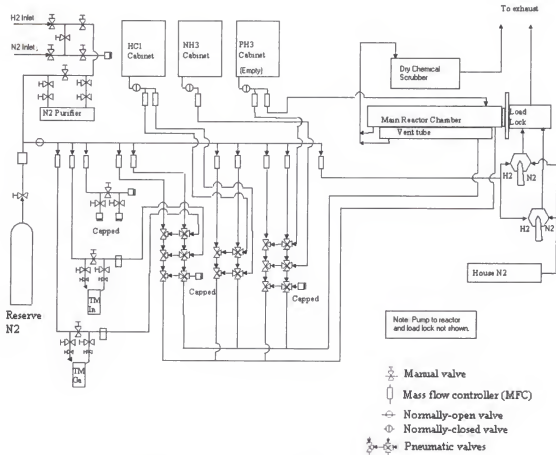


Fig. 3-1. H-MOVPE chemical reactor system schematic. Mass flow controllers are Tylan FC-type. Manual valves are Nupro model SS-DSV1-VCR4. Pneumatic valves are either Nupro SS-BNVCR4-NO or SS-BNVCR4-NC, depending upon normal state (open/closed, respectively).

Another major design issue was the geometry of the reactor tube. Several issues were addressed, and a tubular design was adopted for three primary reasons. First, the design was simple, in that process flows could be easily envisioned and modeled (if desired).

Secondly, the design was capable of modular upgrades. This permitted flexibility according to research needs and goals. For instance, scale-up to 2" diameter wafers did not require an entire system redesign from inlet through furnace to exhaust. A larger reactor was set in place, and the material needs for scale-up were complete. At the time,

a larger load-lock was installed as well, but that was unnecessary for the accommodation of 2" wafers; it was an opportunistic addition. Currently, the maximum wafer size is 2"x2" square, or 2" diameter.

Finally, a tubular design permitted flexibility in the design of the inlet injection nozzle, which was a critical design feature in terms of fluid dynamics and control of the deposition and TMG/HCl mixing reactions. Attachment of the inlet to the reactor by 40 mm Ultratorr compression fitting provided the capacity to switch inlets *in situ*, quickly and economically. This permitted minimal downtime for breakage, or for redesign (Fig. 3-2).

The reaction kinetics of TMG with HCl were unknown during the design process, yet a design was required that enabled the reactants to mix at a temperature high enough to form GaCl (not GaCl₃) without prematurely decomposing the TMG before reaction with HCl. The initial fabricated inlet therefore featured a central metalorganic tube that was attached to the inlet through a bored-out 13 mm Ultratorr fitting (Fig. 3-3). In this method, simply loosening the fitting and sliding the TMG tube in or out along the centerline of the inlet could vary the location of the intermixing of the HCl with the TMG. Later, when the distance was known, this feature was removed in favor of a simple ring seal between the TMG tube and the inlet.

The initial inlet design worked well in practice. The only issue for which design improvement was attempted was side-to-side uniformity for 2" films. To that end, flared (by making the wafer end of the inlet bell-shaped) and rectangular injector geometries were investigated, but no significant improvement was seen.

A third major design issue was the types of fittings between the various system components (reactor, gate valve, inlet, exhaust, and reactant lines). The ideal fittings for the upstream components (reactor-inlet and inlet-reactant lines) were necessarily leak-tight, capable of quick and repeatable connection, and as minimal a source of contamination as possible. Temperature sensitivity was unimportant, unlike the reactor to exhaust joint. Therefore, Ultratorr compression fittings were selected over ground glass or standard-taper joints. The connection between reactor and gate valve was chosen to damp the mechanical shock of opening and closing the gate valve. While the flexible bellows sleeve between the two was the primary means of dampening this motion, the rubber-gasketed 3" Ultratorr fitting provided additional capability. Finally, the connection between the exhaust and the reactor was specified by the elevated (350+ °C) temperature at this joint. A 75/50 mm ball-and-socket joint was selected, coated with a thin layer of high-temperature/low-vapor-pressure vacuum grease. Although an Ultratorr connection was once attempted, the high temperatures baked the rubber O-ring gaskets, causing them to harden and lose their ability to seal properly.

The fourth consideration of the system design was the ability to conduct both MOCVD and HVPE runs in the same reactor without time-consuming modifications or equipment replacements. To this end, a hot-wall reactor design was used, which allowed independent temperature control over up to six different zones of the furnace (Fig. 3-4). The hot-wall design was necessary because temperature control of both the HCl/TMG mixing zone and the growth zone were required. The other zones complement these two, moderating any temperature oscillations, and increasing the ramp rate of the furnace. Typically, all of the furnace zones are on for HVPE growths: the first two maintain

control over the HCl/TMG mixing temperature, the next two control the growth temperature, and the final two minimize deposition beyond the exhaust sidearm. Since there is no need for HCl mixing for MOCVD growths, and since high temperature would cause premature decomposition of metalorganics, the first two temperature zones are not powered for growth in pure MOCVD mode. This keeps the metalorganic at relatively low temperature before entering the growth zone of the reactor (the centermost 6" furnace element in Fig. 3-4).

The final design of the reactor system is shown in Figures 3-2 and 3-3. Of special note are the concentric tubes that keep the HCl and TMG separate until the mixing zone, and the ammonia and gallium species separate before reaction in the growth zone. Figure 3-4 shows the inlet and reactor when fully assembled and resting in the clamshell furnace, and Figure 3-5 shows the reactor in operation.

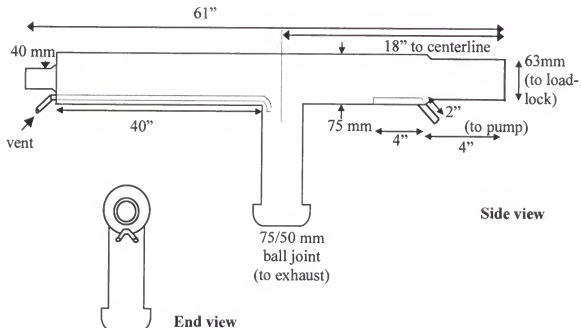


Fig. 3-2. H-MOVPE main reactor tube and dimensions (not to scale).

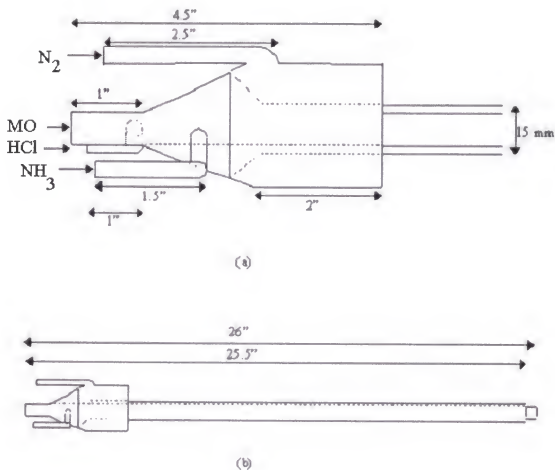


Fig. 3-3. (a) Close-up view of H-MOVPE inlet section, before coupling to reactor. (b) extended view. $\frac{1}{4}$ " MO tube is not shown, for clarity, but is slid coaxially into 15 mm tube at location marked "MO," and secured with Ultratorr connection.

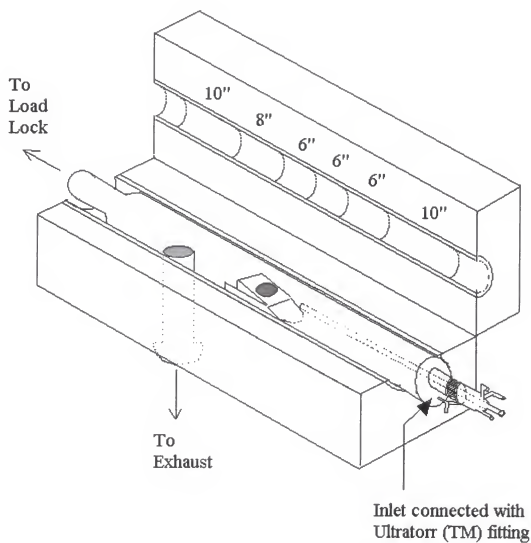


Fig. 3-4. Schematic showing reactor assembly, clamshell furnace, and furnace filament details.

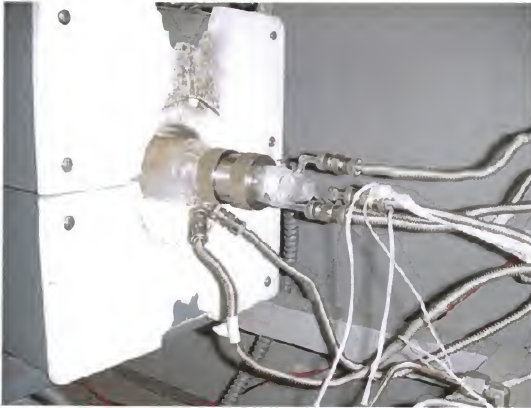


Fig. 3-5. Assembled inlet and reactor.

Experimental Procedures

Substrates used in these studies include (0001) sapphire, (111) silicon, silicon carbide, (001) LiGaO_2 or lithium gallate (LGO), (100) LiAlO_2 or lithium aluminate (LAO), and ScMgAlO_4 . Sapphire and silicon were most commonly used. The sapphire substrates used for this work are (0001)-oriented [basal plane], Czochralski-grown, 10 or 13 mils thick. Union Carbide/Bicron Crystal Products provided the majority of the sapphire used. Wacker-Chemitronic GMBH produced the (111)-oriented silicon, which was primarily used as test wafers for shakedown runs to test procedures and equipment. Silicon carbide was hexagonal (6H) in structure, and was produced by Cree, Inc. Lithium gallium oxide and lithium aluminum oxide substrates were Czochralski-grown and supplied by MTI and Crystal Photonics, Inc.

Prior to crystal growth, substrates are degreased by immersion for 5 min each in boiling 1,1,1-trichloroethylene, acetone, and methanol, and are blown dry with house nitrogen. Acid etching is generally not used. Acid-etched substrates produced uniformly poor quality epitaxial GaN films on sapphire and SiC.

The substrate is loaded upon a quartz, sled-like wafer holder, which is then manually loaded into a stainless steel load-lock. The load-lock is pumped to rough vacuum and refilled with nitrogen, and the cycle repeated six to ten times. The gate valve is opened, and the sled is loaded into the reactor by translating a magnetically coupled arm. The arm is drawn back into the load-lock, and the gate valve is closed. Then the reactor is pumped down using a mechanical roughing pump and purged three to six times with nitrogen to desorb contaminants from the reactor walls. The wafer is permitted to come to thermal equilibrium under nitrogen for 10 minutes. Ammonia flow is started to the run side of the reactor, and HCl and TMG flows are started to the vent side. After 10 minutes of nitridation (unless otherwise noted), the HCl and TMG are shunted to the run side.

At the end of the growth run, the HCl and TMG are reshunted to the vent, and then all reactant flows are stopped. An exception to this case is made when LGO or LAO is the substrate being used, in which case NH_3 is flowed until the furnace temperature drops below a given value, typically 700°C . The reactor is again purged with nitrogen for 10 minutes, and unless the growth is on LGO or LAO, the substrate-bearing wafer holder is removed from the reactor. If the growth is on LGO or LAO, the reactor is allowed to cool to room temperature, at which time the film is removed.

Initial Investigations

A quick set of investigations was performed to verify that the H-MOVPE chemistry conformed to expectations based upon both the literature review and growth experience. Figure 3-6 shows the film thickness versus time for GaN growths upon a sapphire substrate. The growth temperature was 950°C, the HCl/Ga ratio was 2.0, and the NH_3 flow rate was 500 sccm. As expected, the growth rate is linear with time within measurement error, at a value of $\sim 14 \mu\text{m/hr}$.

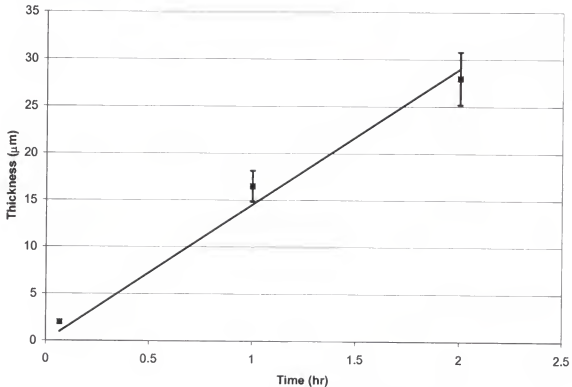


Fig. 3-6. Thickness as a function of time for GaN films grown under identical conditions. Cl/Ga = 2.0, F_{NH_3} = 500 sccm, T = 950°C.

The second verification concerned the variation of growth rate with input gallium flow rates. The TMG mole fraction was increased and by increasing the HCl flow

proportionally, the HCl/Ga ratio was kept at the constant value of 2.0. Compensatory reduction of the N_2 carrier gas was unnecessary (to keep total flow rate constant), due to the minor impact ($< 0.1\%$) of the increased TMG and HCl upon the total flow rate. The growth temperature was kept constant at 950°C , and the NH_3 flow rate was kept constant at 500 sccm.

Figure 3-7 confirmed the reports in the hydride and MOCVD literature of the first-order dependence of the growth rate with the group-III flow rate, in this case trimethylgallium (TMG). From the graph, the first-order dependence of growth rate upon TMG flow rate was apparent, and thus TMG was known to be the limiting reactant.

While producing thicker films, however, very high TMG flow rates produced films that were gray and polycrystalline in the center of the wafer. This result was consistent with the available literature. Safvi et al. have attributed this effect to locally small V/III ratios, which are well known to produce poor quality films [156-158]. He found that when the wafer was very near to the inlet nozzle, insufficient NH_3 diffused to the center of the wafer. The increased growth rate also contributed to localized NH_3 depletion, because the region of highest growth rate—the center of the wafer—had the lowest NH_3 mole fraction even neglecting the growth reaction. Including the growth reaction in the computational fluid dynamics calculations further reduced the V/III ratio. Increasing the distance between substrate and nozzle permitted higher NH_3 diffusion, and the crystallinity of the GaN film improved to single-crystalline.

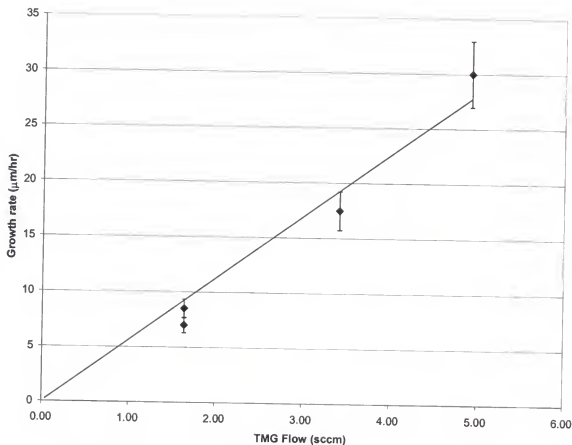


Fig. 3-7. Growth rate as a function of TMG flow. $\text{Cl/Ga} = 2.0$, $F_{\text{NH}_3} = 500$ sccm, $T = 950^\circ\text{C}$.

Parametric Investigation of the H-MOVPE System

For a given chemical reactor system, it is important to explore the envelope of process parameters that affect film growth, especially for the production of single crystalline films. Exploration of these parameters provides information regarding the capabilities of the machine, and an understanding of what can and cannot be done through this chemistry.

For example, within the capabilities of the H-MOVPE reactor system, several growth regimes are possible. Low temperature films may be deposited for use as buffer layers to improve the quality of epilayers subsequently deposited at high temperature. The lower growth rates of MOCVD films may be utilized to obtain highly planar surfaces for use in vertical cavity laser devices or high-brightness LEDs. High growth rates from HVPE may be used for thick film growth, especially for use as substrates.

It is for this reason that the process parameters of temperature, HCl/Ga ratio, V/III ratio, and wafer tray position were varied to understand the details of GaN film growth by the H-MOVPE method. With an understanding of how these factors affect the quality of as-grown film, an optimal recipe for the production of a given epilayer or device can be formulated.

Substrate growth, which is the primary goal of this work, demands single-crystalline layers. Wafer uniformity and low dislocation density are also desirable, but may be parleyed against high growth rates. This section reports upon the optimization of growth parameters that produce single-crystalline film at high growth rates and surface uniformities, and suitably low dislocation densities and roughnesses.

Method

An investigation was performed to determine the effect of several process variables upon the quality of the epitaxial GaN films grown upon sapphire substrates. In all experiments, the total volumetric (and therefore, molar) flow rate through the reactor was held constant, as were all process variables except for the one being examined. Where reactant flows were varied, the additional reactant volume displaced the nitrogen in the main reactor flow, to maintain the same total molar flow rate. The baseline parameters for crystal growth are given in Table 3-2.

Table 3-2. Standard process parameters for optimization growths.

Process Variable	Value
Growth temperature	950°C
Total flow rate	4 slpm
Trimethylgallium flow rate	2.3 sccm HVPE; 0.38 sccm MOCVD
NH ₃ flow rate	500 sccm
HCl (10% in N ₂) flow rate	45.3 sccm
TMG dilution stream flow rate	300 sccm
V/III mole ratio	220 (2000 MOCVD)
HCl/Ga mole ratio	2.0
Substrate	Sapphire (Al ₂ O ₃)

The thickness, structural perfection, roughness, luminescence, and composition of the epilayers were measured. Thickness was measured by three methods. In order of preference, the methods were optical profilometry, cross-sectional SEM, and gravimetric. The last was only used to measure the average thickness of films grown on 2" diameter wafers, since cleaving was generally not desirable. Optical profilometry was restricted to films that were mirror-smooth or nearly so. Agreement between the optical profilometry and SEM techniques was typically $\pm 10\%$. Optical profilometry was carried out on a customized Ocean Optics LS-1 ellipsometer attached to an Ocean Optics PC-1000 spectrometer. The SEM used in this analysis was a Hitachi S-450 SEM. The balance used as a Denver Instruments XE-50 microbalance, with resolution of ± 0.0001 g. All of these instruments are located in the Microfabritech building in University of Florida's Surge Area.

Structural perfection was typically assessed by X-ray diffraction, but some high-quality films were also examined by transmission electron microscopy (TEM). Typically, samples were characterized by low-resolution X-ray diffraction using a Cu-K α_1 source, performed on an APD 3270 X-ray diffractometer located in the MAIC facility at University of Florida. Single-crystalline films were further characterized by

high-resolution XRD, performed on a Phillips MPD 1880/HR X-ray diffractometer. Transmission electron microscopy was used both in plan view and cross-sectional modes to classify and quantify defects in epilayers and substrates. The microscope used was a JEOL 200CX, also located in the MAIC facility.

Surface roughness was characterized by atomic force microscopy, performed on a Digital Nanoprobe III set in tapping mode. Surface profiles were usually taken for $1\ \mu\text{m}$ x $1\ \mu\text{m}$ and $5\ \mu\text{m}$ x $5\ \mu\text{m}$ areas, and repeated once on a different location on the film, to gauge uniformity. Height and amplitude scans for each area were generated, and from the height scan, a roughness was calculated using the data analysis program of the Nanoprobe III.

Luminescent properties of films were investigated through photoluminescence using two systems. The first, an Oriel Instruments PL system, was located in the Surge Area at the University of Florida. Films were irradiated with light from a mercury xenon lamp filtered through a monochromator set to 325 nm, and the resultant spectrum was measured from 350 nm to 800 nm, with the ~ 600 nm second-order source peak separately eliminated by an attached filter. Optimization films were also analyzed using an ACCENT RPM 2000 PL mapping system operating at 325 nm, located at Uniroyal Optoelectronics in Tampa, Florida.

Temperature

The first parameter investigated was growth temperature. The effect of growth temperature upon crystal quality for GaN grown upon sapphire substrates is well documented [36, 156-158, 224]. With increasing temperature, the film changes in structure from amorphous to polycrystalline to single crystalline. In terms of modes of

growth, the film changes from amorphous to three-dimensional growth to truncated pyramidal growth to classic two-dimensional step-flow growth. The transition temperature from three-dimensional to two-dimensional growth was reported in the literature as between 960 and 980°C [154].

The growth regime also changes from reaction-limited to diffusion-limited to thermodynamic-limited growth with increasing temperature, which is schematically shown as in Figure 3-8. From this figure, the apparent activation energy for the rate-limiting step can be calculated as the negative slope of the logarithm of the growth rate versus reciprocal temperature for the kinetic-limited regime.

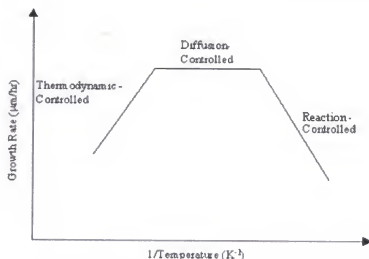


Fig. 3-8. General modes of CVD growth.

The optimization of the growth temperature for the H-MOVPE reactor system ranged between 450 and 950°C. The lower limit was previously found to be the lowest temperature at which film growth occurred. Film growth in this region is amorphous, and may be used as buffer layers between sapphire and epitaxial film growth for devices. The upper limit was set by the upper limit of the furnace at the specified flow rates, rounded

to the nearest 25°C. The steady-state upper limit of temperature for the HVPE growth system was generally ~960°C.

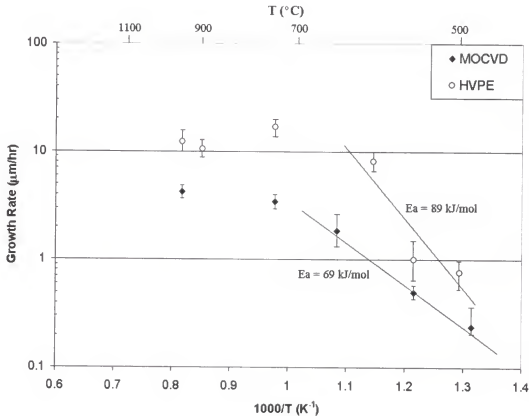


Fig. 3-9. Growth rate as a function of temperature. $F_{\text{NH}_3} = 500$ sccm; $\text{HCl}/\text{Ga} = 2.0$ for HVPE, $\text{HCl}/\text{Ga} = 0$ for MOCVD.

The effect of temperature upon growth rate is plotted in Figure 3-9 for the two different growth techniques comprising the H-MOVPE method. The HVPE growth rate increases exponentially with temperature until ~700°C (973 K), at which temperature the growth rate levels off to the 10 to 15 $\mu\text{m/hr}$ range. The MOCVD growth rate behaves in a similar fashion, although the growth rates are lower than for the hydride method. The activation energies for both methods were calculated as the best-fit line between the

points ranging from 450 to 700°C inclusive. For HVPE, this value is 89 kJ/mol, which is comparable to literature values of 90 and 101 kJ/mol [36, 128]. This best-fit value was for a line with an R^2 value of 0.86, indicating a moderate fit, but similar to values reported in the literature.

The MOCVD activation energy was calculated to be 69 kJ/mol. Theodoropoulos reported that the highest activation energy was (59.5 kJ/mol) for the initial homolytic fission of a methyl radical from TMG, which was thusly considered a rate-limiting step [220]. The reaction path involving adduct formation had an activation energy of 49 kJ/mol. Both of these energies were calculated on the basis of statistical chemistry, using parameters from Jacko and Price [225]. Safvi used the statistical chemistry approach, as well, using data from Mihopoulos to obtain an activation energy of 50.5 kJ/mol [221, 226].

These two literature reports involve computational fluid dynamic modeling of CVD reactors, however. The surface reactions are assumed to be very fast ($E_a \sim 0$ kJ/mol) due to the high temperature at the growth surface. This assumption is not necessarily true for low-temperature, kinetically limited growth as described here, and thus the reported E_a should only be considered the lower bound of the activation energy for deposition.

Two other reports in the literature use experimental data to calculate the activation energy. However, the data are for MOCVD growth with H_2 carrier gas, instead of the N_2 carrier used in the H-MOVPE system. This changes the rate-limiting step of the deposition chemistry, because TMG decomposes more rapidly in H_2 than N_2 . Even so, the two literature values are far apart. Talalaev et al. calculated an E_a of 41 kJ/mol, and

further attributed the rate-limiting step to the pyrolysis of methyl groups at the wafer surface [227]. Chen and coworkers stopped just short of calculating the E_a , but their regressed data yielded an E_a of 93 kJ/mol [228]. The problem inherent in both papers is the sparse amount of data used—2 data points by Karpov, and 3 by Chen—to calculate the activation energy. As a result, minor variations in measurement of a single growth rate have a very large impact upon the final calculation. Based upon these results, the most that can be concluded is that the value of the MOCVD activation energy is at least 49 kJ/mol, that H-MOVPE-obtained value of 69 kJ/mol for the MOCVD activation energy is therefore reasonable, and that a few more data points should be obtained to lower the uncertainty in this data.

X-ray diffraction (XRD)

Analysis of the crystal structure of all optimization films was performed using low-resolution X-ray diffraction. Films over 5 μm in thickness that demonstrated single-crystal wurtzite character were further analyzed with high-resolution XRD to determine the full-width at half-maximum (FWHM) of the (0002) GaN peak taken by an ω -scan. These parameters measure the relative orientations of subdomains in the film, and are measures of crystalline perfection. The narrower the FWHM, the smaller the tilting and twisting of the subdomains.

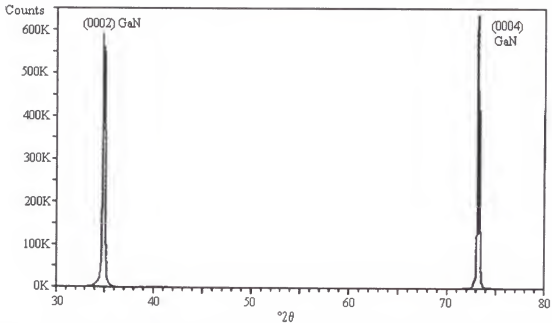


Fig. 3-10. Low-resolution XRD spectrum of a single crystal H-MOVPE GaN/sapphire film.

Figure 3-10 shows the low-resolution XRD spectrum for a single-crystalline film.

The growth conditions for the given film were the baseline conditions: $T_g = 950^\circ\text{C}$, $\text{HCl}/\text{Ga} = 2.0$, NH_3 flow rate of 500 sccm, and a trimethylgallium flow of 2.3 sccm.

Figure 3-11 shows the high-resolution XRD of the corresponding (0002) peak at $2\theta = 34.8$ degrees. The full-width at half-maximum value of 898 arc-seconds is typical of a film grown by HVPE on (0001) sapphire without a buffer layer. The narrowest FWHM obtained for HVPE films grown under the same conditions in the H-MOVPE system was 642 arc-seconds. This value, however, was not repeatable, while the ~ 900 arc-second value was a typical result. Although reported literature values are somewhat lower (560 by Safvi et al. [156, 157], 280 by Molnar et al. [163], for instance), generally either GaCl pretreatments or buffer layers are used. The 642 arc-second FWHM from this work is the lowest published value for HVPE on unbuffered, nitrided sapphire.

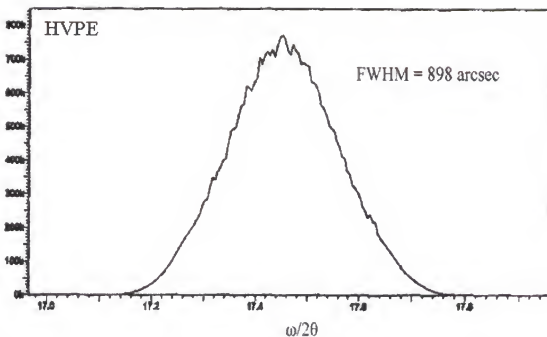


Fig. 3-11. High-resolution XRD spectrum of GaN (0002) peak, with FWHM = 898 arc-seconds.

Figure 3-12 shows the variation of low-resolution XRD spectra with increasing growth temperature under the same (standard) growth conditions for HVPE GaN/sapphire. The transition from amorphous GaN at low temperatures ($T_g < 550^\circ\text{C}$) to textured polycrystalline GaN ($550^\circ\text{C} < T_g < 900^\circ\text{C}$) to single-crystalline GaN ($T_g \geq 900^\circ\text{C}$) is clearly observable. With increasing temperature, the (000x) peaks ($x = 2, 4, 6$) become dominant and then singularly representative. Film thicknesses for the 750°C and 900°C films were several ($5+$) μm , while the thickness of the films grown at lower temperatures was $\sim 1 \mu\text{m}$.

For comparison with HVPE, the XRD results of films grown under MOCVD conditions are shown in Figure 3-13. These films show the same trend. A plot showing the ratio of the intensities of the (0002) GaN peak to the next-highest orientation peak is

shown in Figure 3-14. This figure dramatically illustrates the trend of the domination of the basal orientation with temperature. Single-crystalline GaN film cannot directly be grown on sapphire substrates by the H-MOVPE chemistry at growth temperatures under 900°C using HVPE conditions, nor at growth temperatures under 950°C using MOCVD conditions.

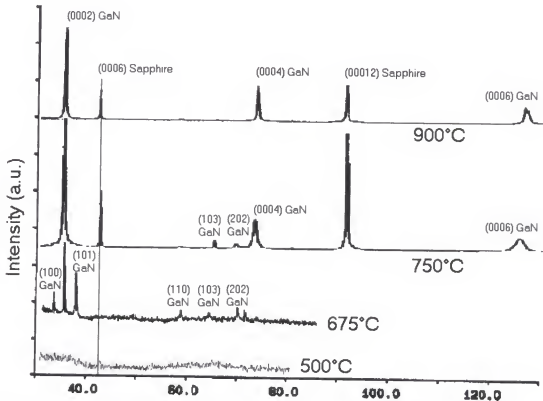


Fig. 3-12. X-ray diffraction spectra showing transition from amorphous to single crystalline film, for HVPE-grown films. Spectra are aligned at 42° substrate peak.

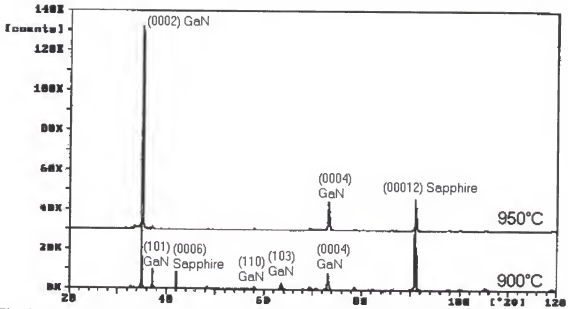


Fig. 3-13. X-ray diffraction spectra showing transition from polycrystalline to single crystalline film, for MOCVD-grown films.

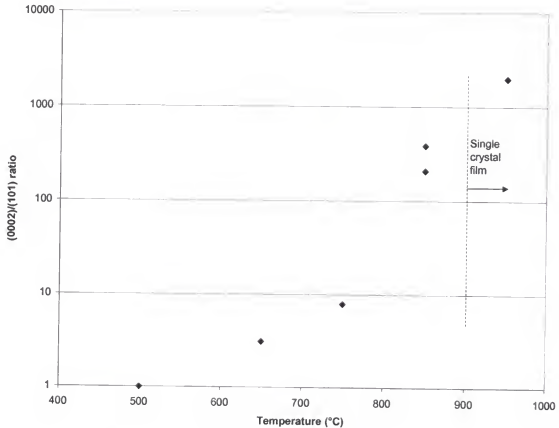


Fig. 3-14. Predominance of (0002) XRD peak, indicating trend toward single crystal film with increasing temperature for HVPE-grown films.

Atomic force microscopy (AFM)

The set of temperature optimization films for HVPE (Cl/Ga = 2.0) conditions were also characterized by atomic force microscopy to determine the surface roughness. Each film was measured twice, and thrice if wide variations of surface topography were present, on different locations on the film. Measurements were performed in tapping mode on a Digital Nanoscope III AFM located in the MAIC facility at the University of Florida. Roughness is distinguished from uniformity by its scope. Roughness as measured by AFM is the point-to-point root-mean-square variation of the planarized film surface. This means, for example, that a nonuniform film that varies exactly linearly from 6 μm in thickness at its leftmost edge to 5 μm at its rightmost edge may have a roughness of approximately zero, although the uniformity of the film is $\pm 20\%$. Alternately, a film which has edge thicknesses of 5.5 μm , but peaks and valleys of 5 μm and 6 μm distributed throughout, is highly uniform but very rough. A representative AFM image for an HVPE GaN film grown upon sapphire is shown in Figure 3-15. This figure illustrates the height variation across the surface, as well as the amplitude variation across the surface, which is the first derivative of the height variation.

Figure 3-16 shows the roughness measurement of the same film from Figure 3-15. The obtained RMS roughness of this film is 2.84 nm, which indicates the nearly step-mode growth regime at 950°C.

The transition from amorphous to three-dimensional to step-flow growth regimes is clearly shown in Figure 3-17. This figure presents the 1 μm x 1 μm and 5 μm x 5 μm RMS roughnesses of the HVPE growth chemistry as a function of growth temperature. The onset of three-dimensional growth, at which point kinetically-limited growth gives

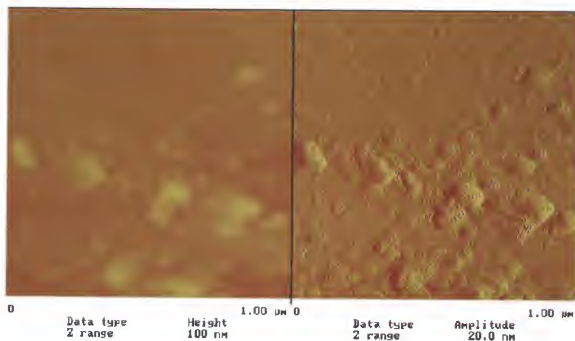


Fig. 3-15. Height (left) and amplitude (right) scans of baseline: GaN/sapphire film grown at 950°C, 500 sccm NH_3 , and 2.0 HCl/Ga ratio.

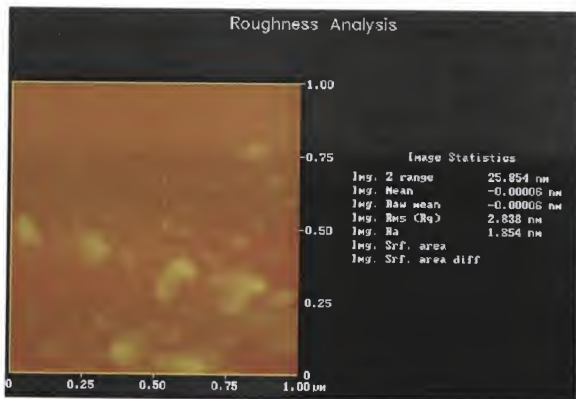


Fig. 3-16. Roughness measurement of baseline film.

way to diffusion-limited growth, occurs between 650 and 750°C. This agrees exactly with the results from the exploration of growth rate versus temperature (see Fig. 3-9). Furthermore, the transition from the three-dimensional mode of crystal growth to step-flow mode occurs at temperatures from 750 through 950°C. This agrees well with literature results from Lee, who report that this transition occurs at approximately 970°C [154]. The minimum roughness for single crystalline film growth occurs at 950°C.

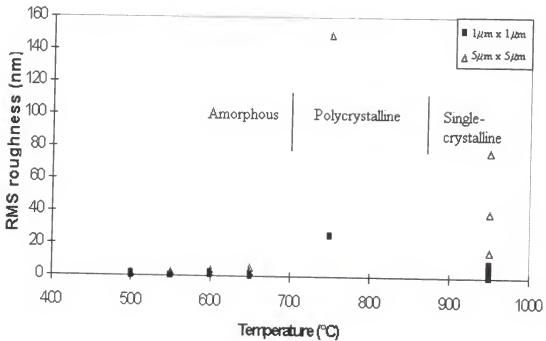


Fig. 3-17. Roughness as a function of growth temperature for HVPE GaN/sapphire films. Multiple values for the same temperature represent measurements performed at various locations on the same film. Cl/Ga = 2.0, F_{NH_3} = 500 sccm.

Before the decrease in roughness can be attributed strictly to growth temperature, however, other variables must be deconvolved. The only process variable to be changed was the growth temperature, but the growth rate was also a function of the growth temperature. Therefore, the effect of growth rate upon surface roughness must be

examined, to be assured that the decrease in roughness with temperature was strictly a result of the growth temperature itself, and not due to the change in growth rates from the temperature variation.

To attempt to deconvolute these effects, the variation of RMS roughness was plotted against growth rate to determine whether a correlation was in evidence. Figure 3-18 demonstrated the absence of a strong correlation for the $1\text{ }\mu\text{m} \times 1\text{ }\mu\text{m}$ scans. The correlation coefficient was 0.58, primarily due to the outliers at $37\text{ }\mu\text{m/hr}$ (1 film, three data points). Without this film, the correlation dropped to 0.289. Figure 3-19 demonstrated the almost-random nature of the $5\text{ }\mu\text{m} \times 5\text{ }\mu\text{m}$ scan dependence. The correlation coefficient for this area was 0.050. The analysis was also repeated for each of the crystal polytypes (Table 3-3). Again, no strong correlations were demonstrated between growth rate and roughness for any polytype, though a mild correlation is present for amorphous films. As a result of these analyses, the conclusion made was that growth rate was not correlated to surface roughness, but that the temperature effect was.

Table 3-3. Statistical correlations between RMS roughness and growth rate.

Size	Overall	No outliers	Amorphous	Single crystal
$1\text{ }\mu\text{m} \times 1\text{ }\mu\text{m}$	0.58	0.289	0.696	0.27
$5\text{ }\mu\text{m} \times 5\text{ }\mu\text{m}$	0.29	0.050	0.50	0.12

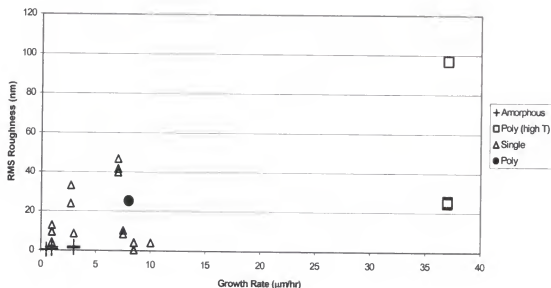


Fig. 3-18. Variation between surface roughness and growth rate, showing lack of strong correlation for $1\ \mu\text{m} \times 1\ \mu\text{m}$ area scans, sorted by growth mode. High-temperature polycrystalline film refers to run performed at 950°C with lowest NH_3 flow rate, which resulted in polycrystalline film. Paired (or tripled) measurements for the same growth rate are for different regions of the same wafer.

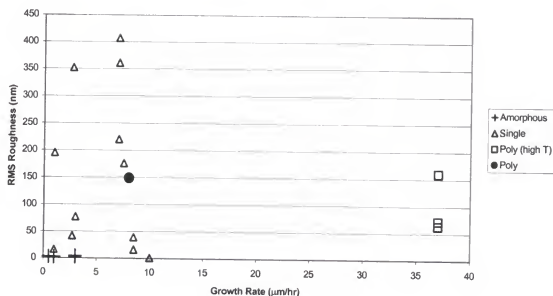


Fig. 3-19. Variation between surface roughness and growth rate, showing lack of strong correlation for $5\ \mu\text{m} \times 5\ \mu\text{m}$ area scans, sorted by growth mode. High-temperature polycrystalline film refers to run performed at 950°C with lowest NH_3 flow rate, which resulted in polycrystalline film. Paired (or tripled) measurements for the same growth rate are for different regions of the same wafer.

Auger electron spectroscopy

The impurity content of the temperature optimization films was obtained by Auger electron spectroscopy (AES). Carbon, chlorine, and oxygen were identified as the most prevalent impurities. While the use of GaN standards is the most accurate method for determining impurity concentrations by AES, these were unavailable, and therefore an alternate means of comparison was necessary. Since carbon and oxygen act as substitutional dopants on nitrogen sites in the GaN crystal, the atomic gallium concentration should be constant throughout all of the films. Thus, the ratios of (C, Cl, O) counts to gallium counts provide the most accurate measure of impurity contamination for comparison among various films. Figure 3-20 shows a typical Auger energy scan for the baseline film, and Figure 3-21 shows the corresponding depth profile. Common peaks for impurities, not distinguishable in the figure, are carbon at ~ 272 eV; chlorine at ~ 181 eV, and oxygen at ~ 510 eV.

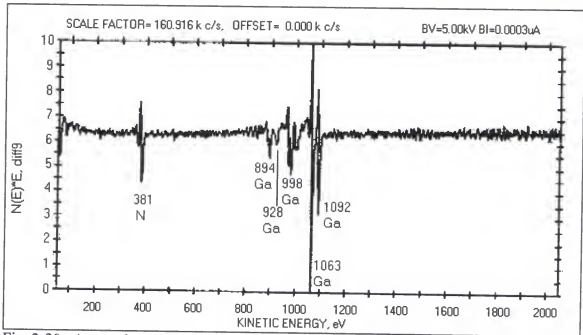


Fig. 3-20. Auger electron spectroscopy spectrum of baseline film. Not shown or indistinguishable are peaks from C, Cl, and O.

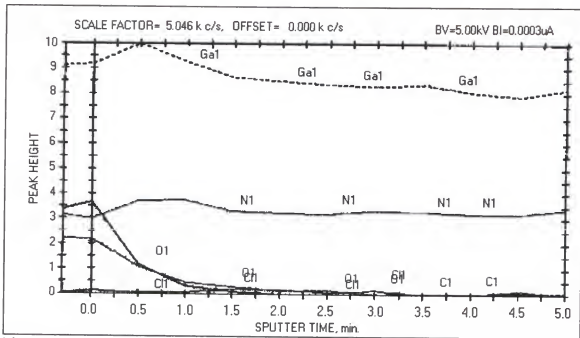


Fig. 3-21. Depth profile of baseline film, showing trace contaminants.

The only reliable data obtained from the AES characterization of the films from the parametric study identified the atomic contaminants, but no trends with temperature or any other parameter. Proof of the inaccuracy of AES for the quantitative measurement of impurities is demonstrated by the wide variation of Ga concentration determined by the measurement software. For GaN, which is a line compound, the bulk Ga concentration should be constant and very nearly 50%. Examples of the variation with temperature of the bulk (Fig. 3-22) and surface (Fig. 3-23) impurity concentrations are diagrammed below. These figures show the unscaled (not impurity-per-gallium atom) measurements; scaling the impurities (Fig. 3-24) further distorts the trendlines. While a general decrease in oxygen contamination is apparent on each figure, the uncertainty arising from the gallium concentration moderates such a conclusion. Clearly, no other correlations can be made.

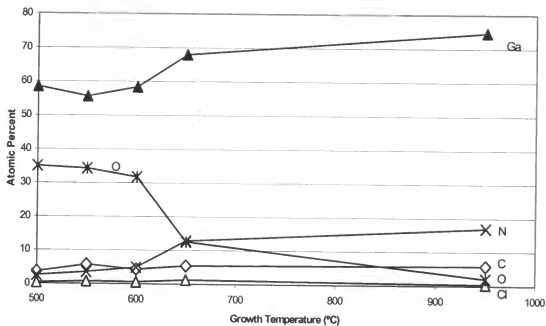


Fig. 3-22. Variation of bulk impurity and native atom concentrations in temperature parameterization films, as measured by AES. $\text{Cl/Ga} = 2.0$, $F_{\text{NH}_3} = 500$ sccm. Sputter time = 1 minute.

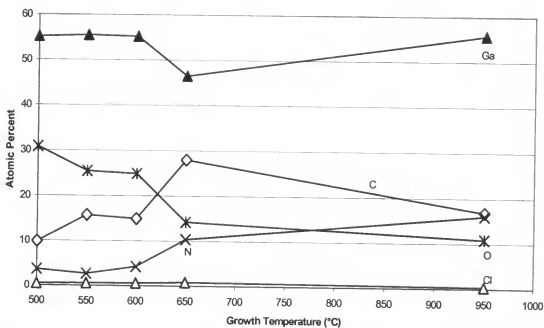


Fig. 3-23. Variation of surface impurity and native atom concentrations in temperature parameterization films, as measured by AES. $\text{Cl/Ga} = 2.0$, $F_{\text{NH}_3} = 500$ sccm.

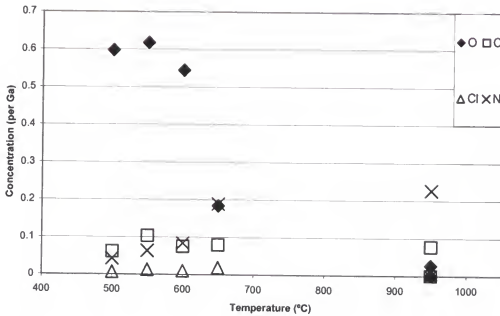


Fig. 3-24. Ratios of contaminants scaled to gallium, as a function of temperature.

SIMS

Although AES provided insight into the identification of impurities on the GaN surface and in the bulk crystal, quantitative accuracy was not the strength of AES, as evidenced by up to 50% error in stoichiometry (75% Ga, 18% N, 6% C, trace O) for single-crystalline GaN. Had the film actually possessed this composition, it would not have shown the clean XRD pattern of single-crystalline GaN, as in Figure 3-10. Therefore, secondary ion mass spectrometry (SIMS) was performed upon the optimization films, to more accurately gauge impurity concentrations.

The SIMS analysis showed detectable amounts of carbon, chlorine, and oxygen. The beam used was a Cs⁺ ion beam at an energy of 5 kV, and a beam current of 103 nA. The survey itself was for negative ions. Sputtering proceeded from the surface of the GaN film. The sputter rate was measured by stylus profilometry to be $11 \pm 1 \text{ \AA/s}$. Since GaN standards were not available for quantification of carbon, chlorine, or oxygen

concentrations, the impurity intensities were scaled to that of gallium-87, which should be very nearly constant throughout the GaN matrix. A mass survey and a depth profile of a representative HVPE film are shown as Figures 3-25 and 3-26, respectively.

The drawback to SIMS was its "matrix dependency." For a constant impurity concentration, the signal will change for different crystalline structures (matrices), even for the same stoichiometry of material. Thus, for analysis of the temperature dependence of impurity concentrations in GaN, where the matrix changed from amorphous to polycrystalline to single-crystalline, SIMS results were viewed skeptically. For other parametric variations where the matrix was invariant, such as HCl/Ga ratio and the NH_3 flow rates (V/III ratio), SIMS provided greater insight into trends in impurity concentration.

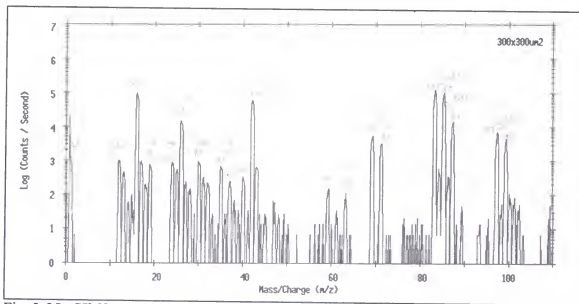


Fig. 3-25. SIMS mass survey of baseline GaN/sapphire film. Growth conditions: $T_g = 950^\circ\text{C}$, $F_{\text{NH}_3} = 500$ sccm, $\text{HCl/Ga} = 2.0$. T_g

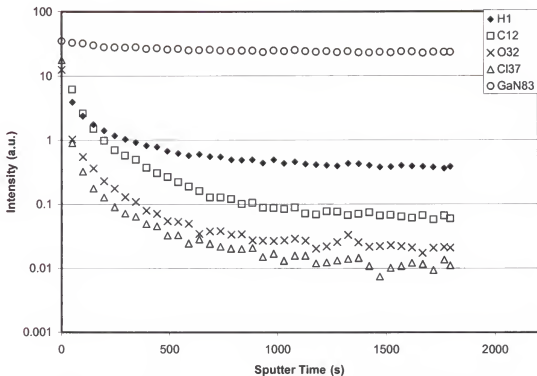


Fig. 3-26. SIMS depth profile of baseline GaN/sapphire film. Growth conditions: $T_g = 950^\circ\text{C}$, $F_{\text{NH}_3} = 500$ sccm, $\text{HCl}/\text{Ga} = 2.0$.

Despite this caveat, the evolution of the GaN matrix—noted by the gradual increase in intensity of the GaN^- ion—appeared in the impurity vs. temperature plot (Fig. 3-27), and was the only reliable and significant trend present. Identifiable impurities were, however, the same as recognized by AES.

The lack of temperature-dependent trends is confounded by the variation of the sputter yield with the evolution of the single-crystalline GaN matrix from the amorphous polytype. If only the amorphous films are considered (those grown at temperatures of 550 to 650°C), the yield variation is minimized. In this case, the oxygen concentration decreases in the film, and the carbon concentration increases.

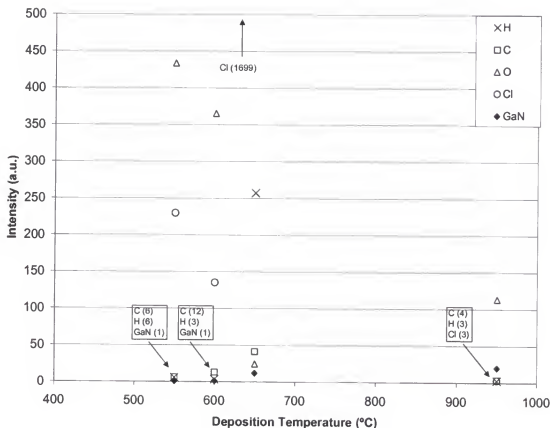


Fig. 3-27. Evolution of GaN matrix with temperature (solid diamonds), as recorded by SIMS data. Ratios of impurities (scaled to Ga₈₇) are shown for H, C, O, Cl. Growth conditions: T_g = 950°C, F_{NH₃} = 500 sccm, HCl/Ga = 2.0.

From a theoretical perspective, the variation of dopant concentrations in semiconductor films proceeds from the thermodynamics of solid-vapor equilibrium at the interface of the growing film. Using Stringfellow's treatment [229], in which the assumption is made that the diffusion coefficients of the V and III species are nearly equal, the input V/III ratio is much greater than 1 so that the group III element will be depleted at the surface. Thus,

$$x_D^s = \frac{J_D}{J_{III}} = \frac{p_D^* - p_D^i}{p_{III}^*} \quad (3-8)$$

where x_D^s is the dopant mole fraction in the solid film, J_i is the flux to the surface of species i , p_i^* is the input partial pressure of species i , and p_D^i is the partial pressure of the dopant at the growth interface. The proportionality of x_D^s and p_D^i is expressed as the distribution coefficient k , so that $x_D^s = k p_D^i$, and thus

$$x_D^s = \frac{p_D^* - (x_D^s/k)}{p_{III}^*} \quad (3-9)$$

From this beginning, the variation of dopant concentrations divides into two cases. When the vapor pressure of the dopant atom is low, $p_D^i \ll p_D^*$, and thus the majority of the dopant reaching the interface is incorporated. From Equation 3-8, x_D^s is inversely proportional to the growth rate (which is itself proportional to p_{III}). This mass transport limited behavior is classified as "case I."

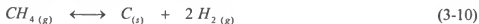
When the vapor pressure of the dopant is high, $p_D^i \sim p_D^*$, and $x_D^s = k p_D^*$. As a result, the dopant incorporation is determined by the thermodynamics of the interface, and is independent of the growth rate. This case, in which the thermodynamics limit the dopant incorporation, is called "case II." This case is characterized by a decrease of dopant concentration with temperature and separate behaviors for dopants residing upon the group III and group V sublattices. Dopants occupying group III sites increase in concentration with increasing group V fluxes (case II (III)), while those occupying group V sites decrease in concentration (case II (V)). A comprehensive discussion of the doping behavior can be found in Stringfellow [229], and the references therein.

Based upon this simple theoretical treatment, carbon should be a case I dopant due to its low vapor pressure, and conversely oxygen should be a case II dopant due to its

high vapor pressure. As oxygen rests on the N-site in GaN, and therefore dopes n-type, case II (V) behavior is expected.

The problem with using this simple model for GaN doping is that it is only valid for growth regimes that are limited by mass transport, because the assumption is no longer valid that the group III element will be depleted at the interface. In this case, the group III flux will be proportional to the difference between the input partial pressure of the group III species and the group III partial pressure at the interface, instead of merely being proportional to the input partial pressure of the group III species. Since the partial pressure of the group III species at the interface will depend upon both the group V partial pressure and the reaction kinetics (assuming that the group V kinetics control, as is the case for ammonia in GaN growth), the expression for x_D^S increases in complexity. A more detailed summary is presented in Stringfellow (58 JCG 914, 1982). In any case, the lack of data from the mass transport limited growth regime is simply insufficient to make conclusions about the doping behavior with respect to the temperature parameterization study. The HCl/Ga and NH₃ parameterization sections of this chapter are both mass transfer limited, so this treatment is applicable to those sections of this work.

A further complication specifically regarding the analysis of carbon as an elemental dopant species is the significant ($x \sim 1.9 \times 10^{-4}$ at thermodynamic equilibrium) mole fraction of methane in the gas phase. If the carbon in the film is in thermodynamic equilibrium with methane in the gas phase, then the carbon incorporation will depend on the methane decomposition equilibrium (Equation 3-10).



As the equilibrium constant for this decomposition reaction is proportional to $[H_2]^2$, the activity of carbon in the film will change inversely with the amount of hydrogen in the gas phase, and therefore should be sensitive to the mole fraction of ammonia in the input gas phase. Furthermore, the equilibrium constant itself is temperature-dependent. Both of these factors suggest that the thermodynamics of carbon incorporation in HVPE GaN is nontrivial, and correspondingly worthy of future study.

Summary of temperature optimization

From the variation of growth temperature for both HVPE and MOCVD techniques, the basic growth regimes of the H-MOVPE system have been determined. Measurable GaN growth begins at about 450°C for both HVPE and MOCVD. A plot of growth rate as a function of reciprocal temperature revealed a transition from kinetically-limited growth to diffusion-limited growth at ~750°C for HVPE growth (Fig. 3-9). From measurement of the growth rates of the films in the kinetically-limited growth regime, apparent activation energies for each type of growth were estimated. A value of 89 kJ/mol was obtained, which was comparable with literature values for the activation energy of the HVPE deposition reaction. For MOCVD, the calculated value of the activation energy was 69 kJ/mol, which was higher than reported literature values.

For both HVPE and MOCVD, the amorphous material grown at the low temperature of 500°C gradually increased in crystallinity over the temperature range 550 to 900°C, with higher temperatures displaying more (0002) character. The film became single-crystalline above 900°C for HVPE, and above 950°C for MOCVD.

Hydrogen Chloride/Gallium Ratio

In the parametric study, the molar ratio of gaseous hydrogen chloride to trimethylgallium was also examined. This parameter was investigated because the HCl/Ga ratio influences both growth rate and crystal quality. Fewer moles of HCl than TMG can lead to incomplete Ga transport (for instance, formation of Ga droplets), since TMG is unstable at elevated temperatures and GaCl is a volatile Ga species. On the other hand, excess HCl can lead to retention of Ga in the vapor phase and therefore reduction of the growth rate. The available literature on HVPE growth and gallium chloride thermodynamics reports that additional HCl also increases the crystal quality of the film. This phase of the system optimization endeavored to quantify these effects.

The limits of the parameter search are natural. The lowest ratio possible is zero, which corresponds to MOCVD deposition of GaN. The other natural limit is the highest value at which deposition actually occurs; above this value, all of the gallium remains in the gas phase as gallium chlorides, principally gallium monochloride. The set of values of HCl/Ga used in this search was {0, 0.5, 1.0, 1.5, 2.0, 3.0, 4.0, 6.0}.

No growth occurred at HCl/Ga = 6.0 on sapphire, and therefore this value was used as an upper limit for the transition from growth to etching behavior. Whether this value would actually result in etching was unknown, as no experiments were performed to determine the etch rate as a function of HCl/Ga ratio, except for the limiting case of HCl/Ga = ∞ , as described in Mastro et al. [230] Furthermore, the experiments for HCl/Ga = 0.5 repeatedly fouled the inlet with carbon deposition and produced highly nonuniform films. The films were therefore not included in this investigation.

Growth rate

The effect upon the growth rate of increasing the molar HCl flow rate at constant molar TMG flow rate is quantified in Figure 3-28. Because the molar TMG flow for HVPE growth was six times the molar TMG flow rate for MOCVD growth ($\text{HCl}/\text{Ga} = 0$), the MOCVD growth rates are displayed as increased by six times, in order to make valid comparisons regarding growth efficiency. Growth efficiency was defined as the ratio between input moles of gallium (as TMG) and moles of gallium in the final film, which is linearly related to growth rate.

The experimental growth efficiency remains nearly constant, for growth rates ranged between 10 and 13 $\mu\text{m/hr}$ through $\text{HCl}/\text{Ga} = 2.0$, then declined rapidly, falling to zero between values of $\text{HCl}/\text{Ga} = 4.0$ and $\text{HCl}/\text{Ga} = 6.0$. The growth efficiencies at low molar HCl flow rates ranged from 1.6×10^3 to $2.1 \times 10^3 \mu\text{m/mol}$, which is similar to other atmospheric-pressure III-V systems [229].

This behavior variation of near-constant efficiency followed by linear decrease agreed with both Cadoret [231] and the thermodynamic analysis from Chapter Four of this work, "Equilibrium Modeling of the H-MOVPE Growth System." Both of these analyses predicted nearly constant 90+% growth efficiencies beyond the equimolar condition, then linear attrition in the growth rate with increasing HCl.

The theoretical maximum growth rate, assuming that all TMG reacts to form uniformly thick gallium nitride only upon the 2" wafer, was computed to be 46 $\mu\text{m/hr}$. The discrepancy between this theoretical maximum and the experimental results is explained by the observation that not all of the gallium nitride deposited on the wafer surface. Deposition occurred upon the wafer tray, as well as downstream of the growth zone upon the reactor walls. Of significance instead is the validation of the prediction of

constant growth efficiencies past $\text{HCl}/\text{Ga} = 1.0$ (equimolar), and then a rapid, linear falloff.

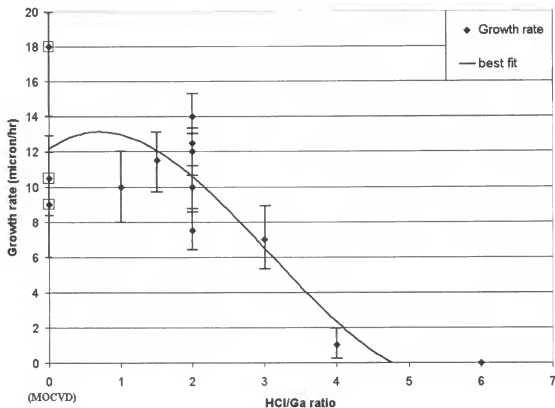


Fig. 3-28. Growth rate as a function of HCl/Ga inlet mole ratio for constant TMG flow. $T_g = 950^\circ\text{C}$, $F_{\text{NH}_3} = 500$ sccm. Multiple values for the same ratio represent films from separate experimental trials.

X-Ray diffraction

Aside from the effect upon growth rate, the other major effect of increasing the molar HCl flow rate is the improvement in the structural quality of the gallium nitride crystal. The optimization films were therefore analyzed using XRD. Unfortunately, XRD only measures the quality of the top $\sim 5\ \mu\text{m}$ of gallium nitride epilayers. This presents a problem when the quality of the film is thickness-dependent, as it is in the "autobuffer region" close to the sapphire substrate. To minimize this effect, only the

spectra of films thicker than 7 μm are displayed, except for films grown under MOCVD conditions.

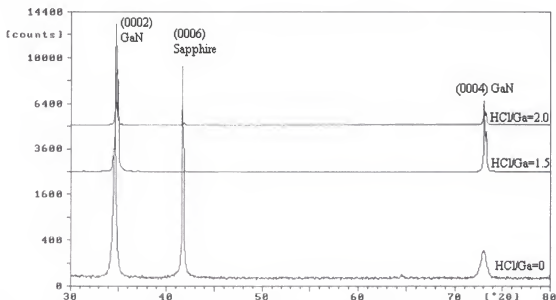


Fig. 3-29. Low-resolution XRD spectra for several values of HCl/Ga inlet mole ratio. $T_g = 950^\circ\text{C}$, $F_{\text{NH}_3} = 500$ sccm.

Figure 3-29 shows the effect of increasing the molar HCl flow rate upon the crystallinity of the GaN/sapphire films. All films grown are single-crystalline and show only basal plane (0002) and higher order reflections, except for the MOCVD film at $\text{HCl}/\text{Ga} = 0$ which shows the c-plane sapphire substrate peak at 42° . Of note is the change in the (0004) GaN reflection, which narrows greatly with increasing HCl flow. This result has two likely causes, the proximity of the highly dislocated interface region for the MOCVD film, and the increase in film quality due to smaller thermodynamic driving forces from increased HCl flow rates (see Chapter 4, “Equilibrium Modeling of the H-MOVPE Reactor Chemistry”). To deconvolve these effects, a thick ($7+ \mu\text{m}$) MOCVD film should be grown and high-resolution XRD of either the (0002) or (0004) GaN reflection compared with its HVPE counterpart. This was not attempted due to

time, scheduling, and budget constraints, but could (with TEM) be the basis of a more detailed comparative study.

AFM

As mentioned in the temperature parameterization above, the surface roughness of the HVPE GaN films decreases with increasing temperature, supporting the hypothesis of a transition from Stranski-Krastenov-mode growth to Frank-Van der Merve-mode growth at the highest growth temperature. This is likely due, at a molecular level, to faster surface diffusion of adatoms leading to reduced islanding and increased terrace-step flow growth. In a similar fashion, anything that increases mobility of adatoms on the surface decreases the probability that the gallium adatoms will cluster into islands, because the adatoms will preferentially attach at kink sites on the step. This is the postulated mechanism for improvement of surface morphology.

Increasing the amount of hydrogen chloride thermodynamically shifts the equilibrium gallium content from the GaN film to the gas phase, where it is found as gallium monochloride or gallium trichloride. The driving force for diffusion to the surface is therefore smaller, and therefore the net flux of gallium to the surface should be smaller. As a result, the amount of reactive gallium at the surface is lower. Since island growth is caused by a surface gallium concentration higher than that which the step-flow growth mode can accommodate, lowering the amount of gallium present at the surface of the film will decrease islanding. Adatoms have sufficient time to diffuse to kink sites on the step. Therefore, increasing the HCl flow rate should improve the surface morphology of the film.

The surface roughness as a function of HCl/Ga ratio for both $1\ \mu\text{m} \times 1\ \mu\text{m}$ and $5\ \mu\text{m} \times 5\ \mu\text{m}$ scan areas is shown in Figure 3-30.

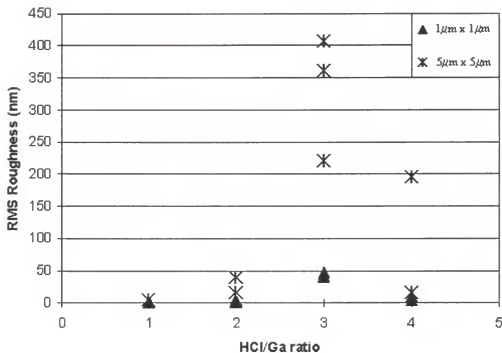


Fig. 3-30. Variation of surface roughness with HCl/Ga ratio. Multiple values for the same ratio represent measurements performed at various locations on the same film. $T_g = 950^\circ\text{C}$, $F_{\text{NH}_3} = 500\ \text{sccm}$.

SIMS

To identify impurity incorporation trends accompanying the variation in HCl/Ga ratio, SIMS was also performed on the optimization films. Figure 3-31 shows the comparison between impurity concentrations in the as-grown films for various HCl/Ga ratios. As analyzed in the temperature parameterization study, the raw data is scaled to the Ga signal, which should be nearly constant in concentration in the matrix.

Based upon Stringfellow's simple doping model described earlier, case I dopant (low elemental vapor pressure) concentrations should change in inverse proportion to

growth rate. The only element that follows this trend in Figure 3-31 is carbon, which increases nominally in concentration until the growth rate decreases for $\text{HCl}/\text{Ga} = 3.0$ and $\text{HCl}/\text{Ga} = 4.0$. Figure 3-32 shows the impurity incorporations multiplied by the growth rate, in order to more clearly identify case I dopant behavior. As can be seen, carbon is obviously a case I dopant.

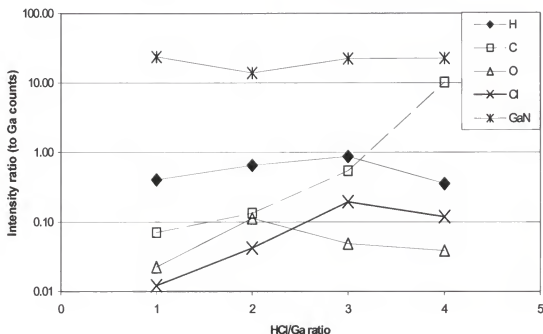


Fig. 3-31. Variation of impurity concentrations with increasing HCl/Ga ratio. $T_g = 950^\circ\text{C}$, $F_{\text{NH}_3} = 500$ sccm.

Interestingly, the concentration of C increases quicker than exponentially in Figure 3-31. With recent interest increasing in carbon doping and carbon/oxygen codoping, this result merits further study as a means to specify carbon (p-type) dopant concentrations in devices. As the H-MOVPE system is unique among hydride-type VPE chemistries, because it incorporates both carbon and chlorine by design into the growth chemistry, it would be ideal for such studies.

Case II dopant incorporation should be linearly proportional to the input mole fraction of the dopant. Oxygen should be included among the dopants with high vapor pressures, but does not show a linear incorporation trend. From this data, no conclusions may be drawn regarding the incorporation of oxygen.

By contrast, both hydrogen and chlorine can be tentatively identified as case II dopants. As the input mole fractions of H and Cl increase linearly with the HCl flow—which for constant Ga flow is equivalent to an increased HCl/Ga ratio—a linear increase in the dopant concentration in the film should be evident. From the graph, it may be seen that hydrogen and chlorine incorporation rise exponentially with HCl flow. The increase makes qualitative sense; with an increase in HCl, one might expect an increase if the hydrogen and chlorine were neutral or nonparticipating in growth reactions. However, the increase does not make quantitative sense. Because the increase is exponential, the elements must affect the interface thermodynamics or kinetics in some way. The theoretical research on GaN HVPE is just starting to investigate the effects of surface modification by elemental species upon film growth (see especially Cadoret and Trassoudaine [231] and Karpov et al. [232]), and this data would be interesting to analyze in such a framework.

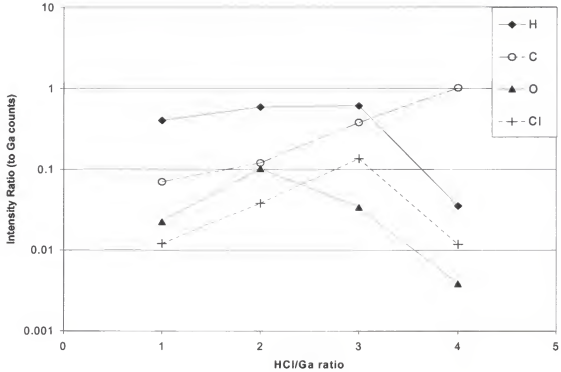


Fig. 3-32. Scaled variation of impurity concentrations with increasing HCl/Ga ratio. $T_g = 950^\circ\text{C}$, $F_{\text{NH}_3} = 500$ sccm.

Photoluminescence

The room temperature (RT) photoluminescence results of the HCl/Ga optimization films demonstrated only one conclusive result, that improved crystal quality is associated with improved band edge (BE) spectral purity. As seen in Figure 3-33, the FWHM of the BE peak passes through a wide maximum with increasing HCl/Ga ratio, although a wide spread in the data is apparent from the measurements taken on two films grown at HCl/Ga = 2.0. This trend appears consistent with an improvement in film quality with increasing HCl/Ga ratio, when coupled with the results from the high-quality MOCVD film at HCl/Ga = 0.

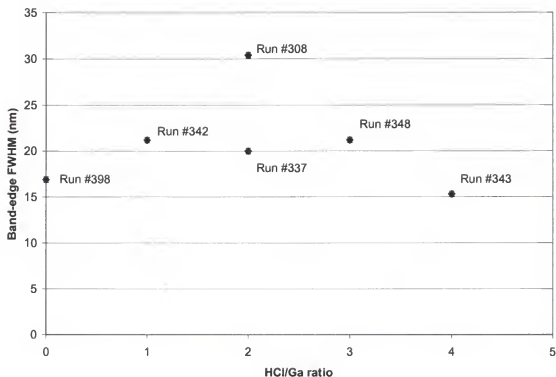


Fig. 3-33. Variation of FWHM of band edge peak with HCl/Ga ratio. $T_g = 950^\circ\text{C}$, $F_{\text{NH}_3} = 500$ sccm for all runs.

The best hydride spectrum, in terms of yellow band intensity to BE intensity ratio, occurred at HCl/Ga = 1.0, although it did not correspond to the narrowest peak. Figure 3-34 shows this spectrum (Run #342), and Figure 3-35 shows the RT MOCVD PL spectrum for comparison (Run #398). The FWHM of both are significantly higher than typical literature values of 2 to 5 nm for the RT photoluminescence of the BE peak for HVPE [77, 159]. Furthermore, the MOCVD spectrum from Run #398 shows a blue peak at 420 nm. This peak was infrequently and irregularly present in the spectra of films grown at 950°C , and has not yet been identified. It is too shallow to be a lithium acceptor peak (which furthermore would show up on SIMS). From its wavelength, this peak could be due to ineffective shielding from fluorescent lighting, but the hypothesis is tentative.

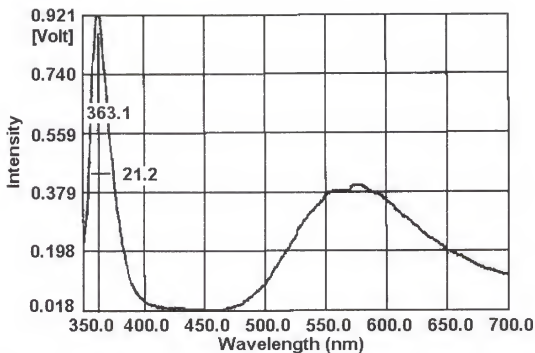


Fig. 3-34. Best room-temperature photoluminescence spectrum of HVPE-grown GaN/sapphire film, grown at 950°C, HCl/Ga = 1.0, NH₃ = 500 sccm.

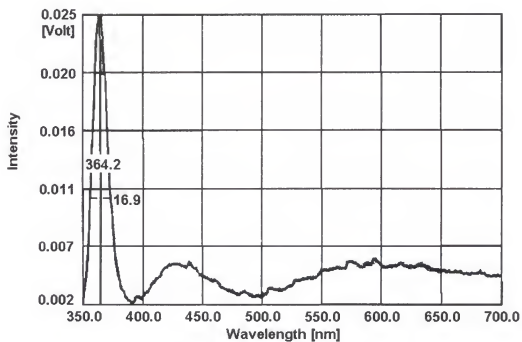


Fig. 3-35. Room-temperature PL spectrum of MOCVD GaN/sapphire film grown at 950°C.

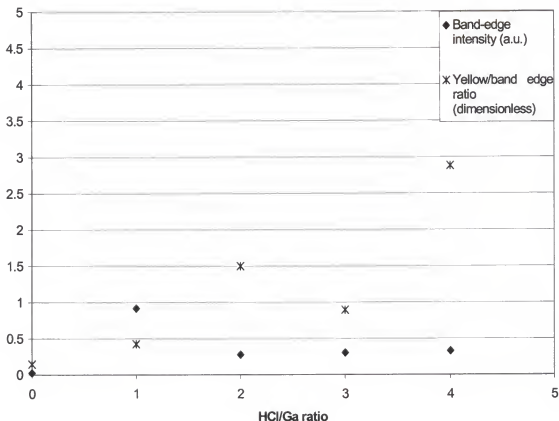


Fig. 3-36. Variation of BE intensity and yellow to BE intensity with HCl/Ga ratio. $T_g = 950^\circ\text{C}$, $F_{\text{NH}_3} = 500$ sccm.

Additional data from the PL spectra are shown in Figure 3-36, but no direct correlation between HCl/Ga and BE intensity or between HCl/Ga and yellow/BE ratio may be extracted. Increased intensity of the HCl/Ga = 1.0 film may simply be due to the effect of smoother surface morphology, since more specular and less diffuse luminescence result in higher intensity of the emitted light.

Summary of HCl/Ga optimization

The HCl/Ga ratio was varied at the base growth condition (950°C , $F_{\text{NH}_3} = 500$ sccm), to determine its effect upon growth rate, surface morphology, film composition,

and luminescent behavior. It was found that a growth rate plateau occurred from an HCl/Ga ratio of 0 to 2.0, and decreased rapidly above 2.0. Crystal quality improved with increasing values of the HCl/Ga ratio. Additionally, a trend of increasing carbon with increasing HCl flow rate was observed, which was the only impurity trend present. Luminescent quality was the best for MOCVD films and films grown at high HCl/Ga ratios, in terms of band-edge FWHM. No trend regarding yellow luminescence was observable.

Ammonia/Gallium Ratio

The third variable modified in the optimization sequence was the ammonia flow rate, which corresponds to the V/III ratio generally reported in the literature. For this series of experiments, the set of flow rates used, in sccm, was {100, 250, 500, 1000, 2000}, and carrier nitrogen was displaced to keep the total flow rate constant. This set corresponds to V/III ratios of {62, 156, 312, 624, 1248}, which are generally higher than literature ratios of 50 to 200 for HVPE growth, though lower than typical MOCVD V/III ratios of 2000 to 5000 [36, 156-158]. Since site blocking has not been reported in HVPE growth of GaN, no detrimental effects of high V/III ratios were expected. The available literature has, however, reported that insufficient V/III ratios result in polycrystalline film growth [156-158].

Growth rate

According to the literature, the growth rate of GaN is weakly dependent or independent of NH_3 concentration for flow rates sufficient to generate single crystalline film. Chu, on the other hand, presents data showing growth rate proportional to the square root of the NH_3 flow rate [72]. This discrepancy may be resolved by noting that the flux of gallium to the surface determines the growth rate in the presence of excess

ammonia when the growth regime is mass transfer limited. By increasing the mole fraction of ammonia in the gas phase, the average molecular mass of the gas phase decreases. Since diffusion coefficient for a molecule—such as GaCl—increases approximately as the inverse square root of the reduced molecular mass of the diffusing gas according to statistical mechanics, increasing the mole fraction of ammonia increases the diffusion of GaCl to the surface. As a result, the growth rate should increase with the ammonia flow rate, in a nearly linear fashion over the range of interest ($0.035 < x_{\text{NH}_3} < 0.69$).

Figure 3-37 showed the variation of growth rate as a function of ammonia flow rate. Also plotted is a curve demonstrating the effect of diffusion upon growth rate. An arbitrary growth rate was chosen to match the data, and multiplied by the ratio of the diffusion coefficient of GaCl in N_2 to the diffusion coefficient of GaCl in the given flow of NH_3 and N_2 . With this consideration, the growth rates matched theoretical predictions reasonably well. The outlier at 100 sccm, which also showed up in data for the small-barrel reactor, can be attributed to film that was polycrystalline. As the growth surface was not the slow-growth basal plane, but a mixture of orientations with different growth velocities, this point should be and was ignored.

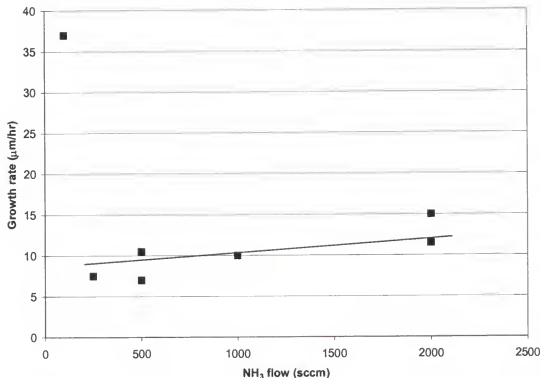


Fig. 3-37. Variation of growth rate as a function of NH₃ flow rate. $T_g = 950^\circ\text{C}$, $\text{HCl}/\text{Ga} = 2.0$.

X-ray diffraction

The variation of the LR- XRD spectra with the molar NH₃ flow rate underscores the importance of the V/III ratio. Below 500 sccm of NH₃ flow (corresponding to a V/III ratio of 312) the GaN films are polycrystalline, as may be seen by the presence of (100) and (101) GaN peaks in Figure 3-38. Therefore, this is a lower limit for the production of high quality GaN films in the H-MOVPE reactor system. This limit may decrease with increased temperature (if the furnace system were to be improved, for instance), which would increase the extent of NH₃ decomposition and therefore provide more reactive nitrogen to the growth surface, or different geometry, which could locally increase the NH₃ concentration at the wafer surface.

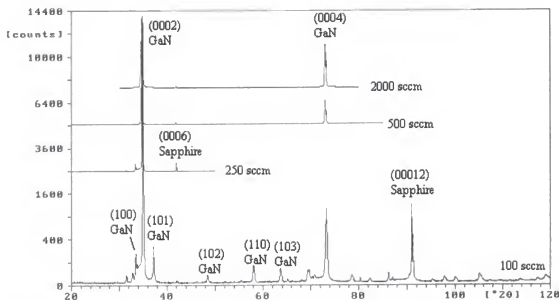


Fig. 3-38. Variation of low-resolution XRD spectra with increasing NH_3 flow rate. $T_g = 950^\circ\text{C}$, $\text{HCl}/\text{Ga} = 2.0$.

AFM

Figure 3-39 shows the variation of surface roughness with the NH_3 flow rate. From the graph, it appears that, although a minimum appears at $F_{\text{NH}_3} = 500$ sccm, higher flow rates possess roughnesses of the same magnitude, especially on the $5\text{ }\mu\text{m}$ square scan. When compared to the parameters of temperature and HCl/Ga ratio, the effect of NH_3 flow rate upon surface roughness is relatively small.

Polycrystallinity due to low NH_3 flows is also apparent in the roughness graph. Crystallites with varying orientations, growing at different rates, will naturally roughen the surface. This is clearly seen by the very high roughnesses corresponding to the 100 sccm flow rate, and is most striking for the $1\text{ }\mu\text{m}$ square area. LR-XRD showed that NH_3 flow rates of both 100 and 250 sccm, corresponding to V/III ratios of 62 and 156, produced polycrystalline film.

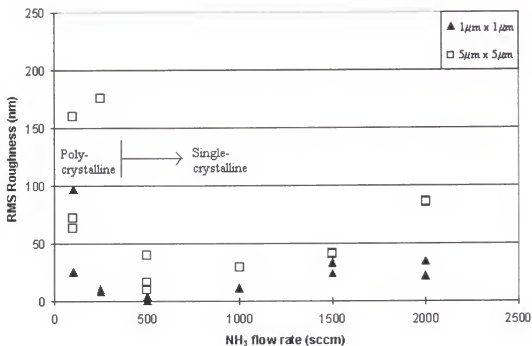


Fig. 3-39. Variation of surface roughness as a function of NH₃ flow rate. $T_g = 950^\circ\text{C}$, $\text{HCl/Ga} = 2.0$.

SIMS

Figure 3-40 presents the SIMS results as a function of the NH₃ flow rate. Despite the apparent decrease in impurity concentrations with increased NH₃ flow, the possibility exists that this is merely an artifact from polycrystallinity. Since SIMS is a matrix-dependent technique, the multiple crystal orientations of the low-flow cases render suspect any overall trends. The abrupt decrease is consistent, however, with the evolution of single-crystalline film at NH₃ flow rates of 500 sccm and higher.

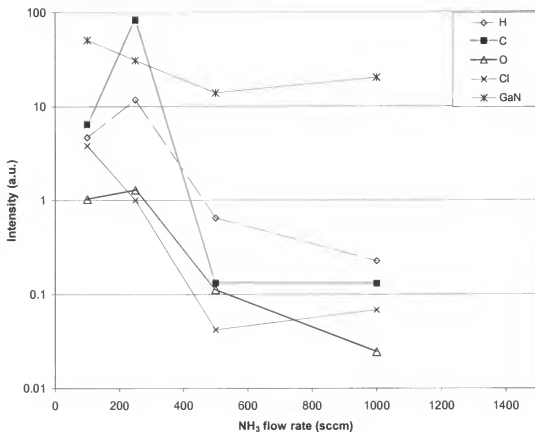


Fig. 3-40. Impurity concentrations as a function of increasing NH_3 flow rates. $T_g = 950^\circ\text{C}$, $\text{HCl}/\text{Ga} = 2.0$.

For most of the measured film properties, variation of the V/III ratio resulted in only minor changes. Surface roughness passed through a weak minimum at $F_{\text{NH}_3} = 500$ sccm, and the growth rate increases slowly due to the mild increase in overall D_{GaCl} . No SIMS or PL trends were observed.

The only important trend present in the V/III analysis was a transition from polycrystalline film below 500 sccm to single-crystalline film, and improving structural quality with increasing NH_3 .

Photoluminescence: Yellow Luminescence

Of primary importance in the production of optoelectronic devices is the spectrum of the light emitted from the material. This is usually analyzed in terms of spectral purity: the number of luminescent peaks, their location, intensity, and width. The most preferable spectrum for GaN devices is a single narrow peak at ~370 nm.

Photoluminescence of films grown under hydride conditions typically showed two peaks, a band-edge peak usually at 367 nm, and a very broad “yellow luminescence” peak centered near 590 nm. Occasionally, a relatively faint blue peak at 425 nm appeared in the spectrum, as well, but could not be assigned. It appeared intermittently in both MOCVD and HVPE films, and only at a growth temperature of 950°C. SIMS did not reveal an impurity causation, and the peak was not further investigated (cf. page 109).

An unresolved question regarding GaN surrounds the origin of the so-called “yellow luminescence,” which is a broad peak centered around ~590 nm (2.2 eV). Various authors have attributed its cause to carbon contamination, oxygen doping, and/or structural defects (Ga/N antisites, N vacancies) [1, 157, 190, 233-235]. Because the H-MOVPE system can perform both HVPE and MOCVD crystal growth, and can vary a wide set of growth parameters, it was believed that this system could provide insight upon a mechanism for yellow luminescence, especially if it were caused by impurities.

The luminescent behavior was investigated as a function of temperature, HCl/Ga ratio, NH₃ flow rate, and carbon and oxygen impurity concentrations. Previously, the parameterization sections of this chapter reported on the variation of the yellow luminescence with process parameters, and found no identifiable trends. Since GaN/sapphire films grown at 950°C were the only films to combine band edge luminescence and yellow luminescence, all optimization films grown at this temperature

were analyzed by SIMS and PL. Since there was apparently no first-order effect between the yellow luminescence and the process parameters of HCl/Ga mole ratio and NH_3 flow rate, the impurity concentrations from all parametric films were used as a group to investigate the relationship between yellow luminescence and impurities. A listing of these films is presented in Table 3-4. In this way, it was hoped, a sufficiently large and diverse data set of films could be obtained for study. No SIMS data exists for experiments 398 and 338; these films were only used for study of the relationship between BE FWHM and YL/BE intensity ratio.

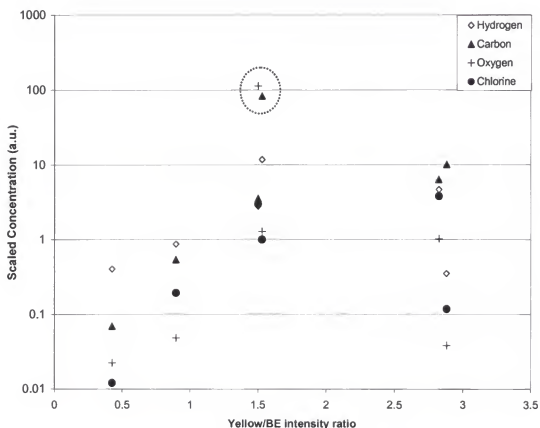


Fig. 3-41. Relationship between H, C, O, Cl bulk concentrations and yellow luminescence.

Table 3-4. Films used for yellow luminescence study.

Experiment	HCl/Ga ratio	NH ₃ flow (sccm)	BE intensity (a.u.)	YL intensity (a.u.)
342	1.0	500	0.921	0.40
308	2.0	500	0.278	0.72
348	3.0	500	0.306	0.274
343	4.0	500	0.331	0.952
336	2.0	100	0.017	0.048
398	0	500	0.027	0.004
338	2.0	250	0.481	0.736

Figure 3-41 shows the semi-logarithmic relationship between impurity concentrations and yellow luminescence among several films. Only mild trends exist—no correlation higher than 0.109 is evident, which occurs between the concentrations of hydrogen and the yellow luminescence. If the outliers at ~1.5 were removed from the data set, however, the correlation with carbon concentration jumps to 0.95—nearly perfectly linear—while the correlation with oxygen concentration improves slightly to 0.321. A separate graph, showing just the carbon/yellow luminescence relationship on a linear ordinate scale, is shown as Figure 3-42. Although this does not conclusively establish a causative relationship between carbon and yellow luminescence, it is suggestive that if the cause of yellow luminescence is impurity-related, then carbon is a good candidate.

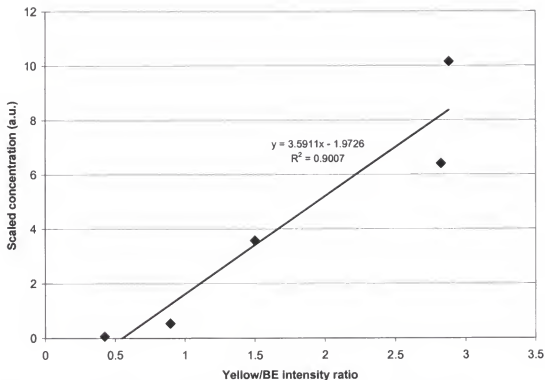


Fig. 3-42. Relation between carbon concentration and yellow luminescence.

Another hypothesis advanced in the yellow luminescence literature is the possibility that the 2.2 eV peak is caused by structural imperfections. Many authors relate the narrowness of the GaN band edge peak to high structural quality [192], although agreement is by no means unanimous. One might expect, that if yellow luminescence was a result of poor structural quality, a correlation would be present between bright yellow peaks and wide band edge peaks. Figure 3-43 shows the relationship between the BE FWHM and the ratio of yellow to band edge luminescence. From the figure, this is not the case, and therefore either the BE FWHM/structural quality association is invalid, or the yellow luminescence/structural quality association is invalid, or both. The information at hand is insufficient to distinguish between these alternatives; either TEM or high-resolution XRD is necessary for further investigation.

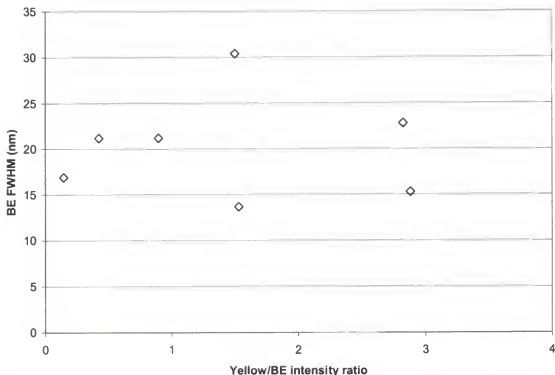


Fig. 3-43. Lack of relationship between band edge FWHM and yellow luminescence.

This analysis suggests that the most likely impurity source for yellow luminescence is carbon, and that there is sufficient evidence to preclude any other impurity sources. A perfunctory attempt to explore the relationship between structural quality and yellow luminescence was performed without definitive results. This topic is worthy of further investigation; causation by structural features may be explored with TEM, and causation by vacancy or antisites may be discerned by EXAFS. By such investigation, all possible causes could be investigated.

Films Grown upon Two-inch-diameter Sapphire Substrates

GaN films were grown using HVPE upon 2" diameter (0001) sapphire substrates. Growth conditions for these films were 950°C, a 2:1 HCl/Ga ratio, and a 500 sccm NH₃

flow rate, which were judged to yield the best film results, judging by the XRD, AFM, and PL results from the parameterization study. The films were then analyzed using optical profilometry and PL.

The thickness variation for both types of films is at least 10% from crown to edge, and often over 50% for the nominal 2-hour growth. The average thickness was $\sim 14 \mu\text{m}$ for the HVPE films. High variations are typical for horizontal hot-wall reactors, although substrate rotation can improve uniformity. Figure 3-44 shows the two-dimensional variation of thickness across a 30-minute HVPE growth on a 2" wafer, as measured by SEM. The bottom of the figure corresponds to the edge closest to the inlet.

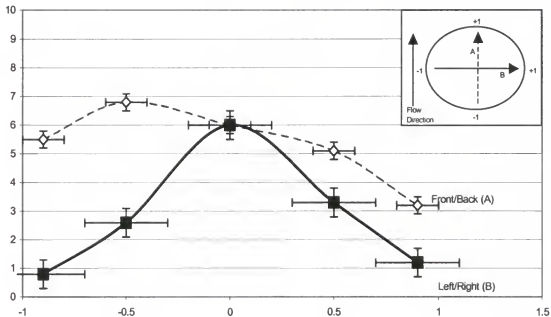


Fig. 3-44. HVPE Thickness variation across a 2" diameter wafer, as measured by cross-sectional SEM.

A representative PL distribution of a 2 hour HVPE growth on a 2" diameter Al_2O_3 wafer is shown in Figure 3-45. Of note are both the wavelength distribution and the FWHM distribution. Despite a very nonuniform thickness distribution, the band-edge

peak is very uniform across the wafer, suggesting that the H-MOVPE technique is feasible for LED production, at least. The thickness variation across the wafer may be seen, however, in the distribution of the FWHM of the band-edge peak, which is shown at lower right in Figure 3-46. The peak is broadest in areas of the film that are the thickest, and the variation in thickness may be clearly inferred from the FWHM distribution. For this particular wafer, the thickness distribution is unavailable.

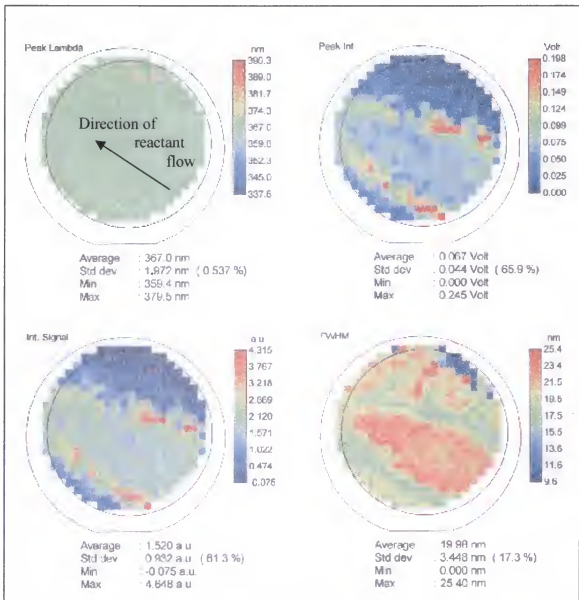


Fig. 3-45. Photoluminescence map of 2" HVPE/sapphire film.

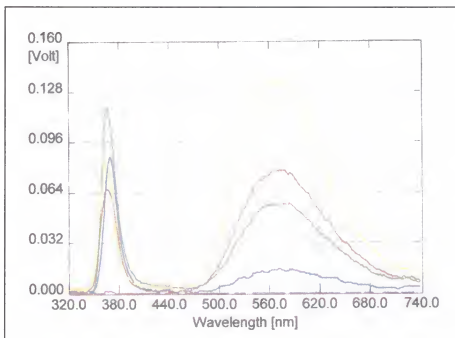


Fig. 3-46. Photoluminescence spectrum from several points on 2" HVPE GaN/sapphire film. Green scan (most intense) corresponds to thinnest film location sampled.

Summary

The envelope of growth regimes possible within the H-MOVPE system was explored, with increased attention focused upon the single-crystal growth regimes. A series of parametric experiments were conducted to identify the crystal growth behavior of the H-MOVPE chemistry, and to provide benchmarks for crystallinity, surface roughness, impurity concentrations, and photoluminescence. The best set of process conditions were found to be 950°C (the highest possible temperature in this growth system), a 2:1 HCl/Ga ratio, and a 500 sccm NH_3 flow rate for films grown upon sapphire substrates.

Using these conditions, thick films were grown on 2" sapphire wafers by MOCVD and HVPE techniques. Generally good morphology balanced poor uniformity

for these films. Adequate but not superior photoluminescence results were obtained from the resulting films.

CHAPTER 4

EQUILIBRIUM MODELING OF THE H-MOVPE REACTOR CHEMISTRY

The purpose of this chapter is to explore details of chemical equilibrium in the gallium nitride H-MOVPE growth system. The study of thermodynamics provides insight into the driving forces of crystal growth. Primarily, it is used to examine the effects of temperature, pressure, composition, and reactant and carrier gas selection upon the phase composition, crystal structure, doping behavior, and maximum possible growth rate of the deposited solid films. In addition, solid solution and, with a point defect model, defect compositions can be estimated, to assist in understanding the effect of growth conditions upon crystal quality. Since the calculations are relatively straightforward, this can streamline the amount of experimental work.

Secondly, information on the stability of substrates, deposited films, and dopants can improve process design and highlight areas of concern. Items such as dopant solubility and miscibility gaps under process conditions can affect the reliability of the final device.

Finally, the deposition of GaN in HVPE has been shown to be limited by mass transfer at typical growth conditions. The gas-solid interface then is expected to be near equilibrium and the net input of species to the near surface region controlled by the relative mass transfer rates and deposition rate. Thus, thermodynamics estimates the growth rate, shape and uniformity of the growth surface, and whether crystal growth is constrained or unconstrained (stable or unstable under minor growth rate perturbations).

While the H-MOVPE system will not be modeled for these effects in this work, such studies are in fact possible.

This treatment, however, examines only the effects of change upon the temperature, pressure, and input compositions on the computed phase and chemical equilibria of the Ga-N-Cl-H-C system as well as the solid solution thermodynamics of gallium with indium and/or aluminum in the H-MOVPE system. This chapter will present the phase and chemical equilibria for the growth of GaN, and Chapter 5 will present the solid solution behavior of nitrides.

Equilibrium Calculations for the H-MOVPE System

Equilibrium Theory

In a closed chemical system in which the temperature and pressure are held constant, chemical equilibrium is defined as that condition under which the system possesses a minimum of Gibbs energy. Expressed mathematically, this condition is

$$\min G = \sum_{i=1}^N N_i \overline{G}_i(T, P, y_i) \quad (4-1)$$

where G is the total Gibbs energy, N is the number of species, N_i is the molar amount of species i , \overline{G}_i is the partial molar Gibbs energy of species i , and y_i is the mole fraction of species i in the gas phase [236]. This objective function is subject to the constraints that the molar amounts be nonnegative, and that the elemental abundances, b_j , at equilibrium are equal to those at the initial distribution among the input species. The latter is simply an atom balance. These constraints are mathematically represented as

$$\sum_{i=1}^N a_{ij} N_i = b_j \quad j = 1, 2, 3, \dots, C \quad (4-2)$$

and

$$N_i \geq 0 \quad i = 1, 2, 3, \dots, N \quad (4-3)$$

where a_{ij} is the stoichiometric coefficient of element j in species i , and C is the number of distinct elements.

At the low pressure and/or high temperature of HVPE/MOVPE, the assumption is made that the gas phase is an ideal gas mixture, so that the activity is equal to the gas phase mole fraction of each species. This simplifies the Gibbs energy equation [237] to

$$G = \sum_{i=1}^N N_i \underline{G}_i(T, P) + RT \sum_{i=1}^N N_i \ln y_i \quad (4-4)$$

for the gas phase. If condensed phases or solutions are present in the system, additional terms are added to Equation 4-4, so that it becomes

$$G = \sum_{i=1}^N N_i \underline{G}_i(T, P) + RT \sum_{i=1}^N N_i \ln y_i + \sum_{j=1}^N \left\{ N_j \underline{G}_j(T) + RT \ln \gamma_j(T, P, x_j) \right\} \quad (4-5)$$

where N_j is the molar amount of condensed species j , \underline{G}_j is the molar Gibbs energy of pure component j , γ_j the activity coefficient of j in solution, and x_j the mole fraction of j in the solution (if applicable). The pure component Gibbs energy, \underline{G}_j , for each species is calculated from thermodynamic data as follows:

$$\underline{G}_i = \underline{H}_i - T \underline{S}_i \quad (4-6)$$

where

$$\underline{H}_i = \underline{H}_i^0 + \int_{T_0}^T \underline{C}_{p,i} dT \quad (4-7)$$

and

$$\underline{S}_i = \underline{S}_i^0 + \int_{T^0}^T \frac{C_{p_i}}{T} dT \quad (4-8)$$

For these equations, \underline{H}_i^0 and \underline{S}_i^0 are the standard molar enthalpy of formation and absolute molar entropy of species i at reference temperature T^0 , and C_{p_i} is the molar heat capacity of the species i . Thus, the objective function G in Equation 4-4 may be expressed as a nonlinear expression of state variables (temperature and pressure) and atomic abundances.

Two numerical approaches to solving this problem exist, non-stoichiometric and stoichiometric algorithms. The difference between the two is that stoichiometric approaches transform the atom-conservation constraint into a set of extents of reaction for independent chemical reactions, and vary the extents to minimize the Gibbs energy of reaction [236]. Non-stoichiometric approaches attempt to directly minimize the Gibbs energy according to the constraints of Equations 4-2 and 4-3, as a nonlinear programming problem. ThermoCalc, the program used to carry out the equilibrium calculations for this chapter, uses the stoichiometric approach to minimizing the Gibbs energy of the system.

The process of specifying the temperature, pressure, and ratio of atom numbers consistent with the relative inlet molar flow rates of the reactant species defined the H-MOVPE reactant system according to the Gibbs Phase Rule.

The program used for these calculations was ThermoCalc version N, developed by Bo Sundmann. This program was created especially for computing chemical equilibrium of complex multiphase systems. The thermodynamic database used for these calculations was the S.G.T.E. database, which is a compilation of JANAF Thermochemical Database data [238] and European Consortium/collaboration data [239].

Computations were performed on a 233 MHz Dell computer equipped with an Intel Pentium III with 128 Mb of RAM, located in the Department of Chemical Engineering.

Equilibrium Calculations for the H-MOVPE System: Temperature Variation

The first investigation performed to understand the thermodynamic behavior of the H-MOVPE system explored the variation of the materials system over the range of temperature used a typical CVD system. Three systems were investigated (Table 4-1). In the first, the set of chemical species (Table 4-2) was restricted to the gas phase. In the second, condensed phases, with the exception of liquid gallium, were permitted to form. And finally, liquid gallium was added to the permitted condensed phases. These calculations were performed to determine which system containing condensed phases best fits the experimental growth data, and to determine the driving force for deposition (G_{dep}) for each system. Table 4-3 lists the thermochemical properties of each species.

Table 4-1. Phases present in three investigations for this work.

Gas phase	Gas and condensed, without Ga _(l)	Gas and condensed, with Ga _(l)
gas	gas GaN _(s) NH ₄ Cl _(s1) NH ₄ Cl _(s2)	gas GaN _(s) Ga _(l) NH ₄ Cl _(s1) NH ₄ Cl _(s2)

Table 4-2. Listing of dominant gas phase chemical species included in calculations. Trace species ($<10^{-15}$ mole fraction at all temperatures) were included in calculation, but for convenience are not listed here.

Ga-containing species	Cl-containing species [not including gallium chlorides]	Other species
Ga, GaH, Ga ₂ , GaCl, GaCl ₂ , GaCl ₃ , Ga ₂ Cl ₂ , Ga ₂ Cl ₄ , Ga ₂ Cl ₆	HCl, Cl, Cl ₂	N ₂ , H ₂ , NH ₃ , CH ₄ , C ₂ H ₆ , CH ₃ , H, H ₂ N, C ₂ H ₄ , C ₂ H ₂ , C ₂ N ₂ , C, N

Table 4-3. Thermochemical properties of species used in calculations

Species	ΔH_f^0 , 298K	S^0 , 298K	a	$b \times 10^3$	$c \times 10^5$	$d \times 10^{-5}$	Ref.
GaN(s)	-137112	-228.0	44.38	-12.60	0.00	-11.73	240
Ga(l)	-21312.3	-477.0	108.23	-454.31	71.15	-8.80	238
NH ₄ Cl _(s1)	-367409	-682.2	132.07	18.40	-7.29	-39.67	238
NH ₄ Cl _(s2)	-367409	-682.2	132.07	18.40	-7.29	-39.67	238
Ga _(v)	259072.3	-49.3	38.71	-21.08	-0.59	-6.77	238
GaH	207264.1	66.7	22.50	20.07	-0.74	1.42	238
Ga ₂ (v)	422882.4	69.8	33.73	18.74	-0.46	0.39	238
GaCl	-81425.6	25.0	37.59	0.18	0.01	-1.75	238
GaCl ₂	-239612	-31.0	58.25	-0.48	0.03	-3.83	238
GaCl ₃	-459466	-147.8	82.18	0.95	-0.02	-6.86	239
Ga ₂ Cl ₂	-246763	-121.6	83.10	0.02	0.00	-3.02	238
Ga ₂ Cl ₄	-644947	-341.9	132.77	0.13	0.00	-9.03	238
Ga ₂ Cl ₆	-1021673	-552.8	182.04	0.59	-0.01	-14.64	238
HCl	-100829	22.1	29.02	-1.96	0.47	0.26	238
Cl _(v)	113735.6	29.4	23.69	0.01	-0.14	-1.54	238
Cl ₂ (v)	-11735.2	14.6	36.25	1.91	-0.05	-2.53	239
N ₂	-8000.13	36.0	27.22	2.52	0.32	0.77	238
H ₂	-9522.97	-47.2	31.36	-5.52	0.45	-1.13	238
NH ₃	-53688.9	59.6	21.22	45.74	-1.08	1.53	238
CH ₄	-77295.6	149.3	2.23	96.93	-2.60	6.11	238
C ₂ H ₆	-90150.1	190.3	-2.38	192.40	-6.90	3.22	238
CH ₃	137013.4	34.8	25.84	42.49	-0.95	0.67	238
H	211801.6	-3.7	20.79	0.00	0.00	0.00	238
H ₂ N	181695.9	36.1	27.17	16.55	-0.03	1.58	238
C ₂ H ₄	47209.53	184.8	-1.51	159.28	-6.69	2.53	238
C ₂ H ₂	210657.4	-59.3	43.33	31.94	-0.66	-7.34	238
C ₂ N ₂	290548.4	-69.1	52.48	34.71	-0.99	-4.32	238
C _(v)	710430.9	38.7	20.98	-0.40	0.02	-0.03	238
N	466446.2	34.3	20.89	-0.17	0.01	-0.06	238

In all cases, solid gallium and liquid and solid (graphite, diamond) carbon phases were excluded from the calculation. Solid gallium was excluded because it melts very close (30°C) to room temperature and unlike liquid gallium at high temperature, does not affect the deposition or processing of gallium nitride. The carbon phases were excluded because, although graphite may be deposited upon the inlet by decomposition of TMG, during normal crystal growth no carbon of any sort is deposited. Although an extremely

stable phase such as graphite or diamond may be thermodynamically favored, exclusion yielding a more accurate model of the system should be preferred for practical purposes.

Gas phase

The first system explored was the gas phase, without any condensed phases. This represents the system with the highest Gibbs energy configuration. The energy difference between the Gibbs energy of this system and the system containing $\text{GaN}_{(s)}$ is the driving force for deposition. For this reason, and for the insight provided into speciation trends with temperature, the gas phase is a valuable subject for study.

The two chemical mixtures under study are listed in Table 4-4. The atmospheric-pressure MOVPE (AP-MOVPE) and low-pressure MOVPE (LP-MOVPE) systems contain the same initial species, but the pressure condition is 760 Torr for the AP-MOVPE system and 76 Torr for the LP-MOVPE system.

Figure 4-1 shows the variation of the most abundant ($> 10^{-6}$ mole fraction at some temperature) chemical species with temperature for the HVPE chemistry. Figures 4-2, 4-3, and 4-4 show the variation with temperature of the gallium-containing, chlorine-containing, and carbon-containing species, respectively.

Table 4-4. Initial chemical mixtures for HVPE and MOVPE cases.

HVPE Chemistry		MOVPE Chemistry	
N_2	2874 sccm	N_2	2874 sccm
NH_3	500 sccm	NH_3	500 sccm
TMG	1.6 sccm	TMG	0.16 sccm
HCl	3.3 sccm		

The most significant trends are the loss of ammonia with increasing temperature and the transition from GaCl_3 to GaCl as the predominant gallium species. The decreased amount of NH_3 at equilibrium parallels the decomposition of NH_3 , and subsequent availability of reactive nitrogen at higher temperatures. The importance of the gallium trend is that crystal growth is slightly more efficient in the mass-transfer-controlled regime, as GaCl diffuses faster through the boundary layer than GaCl_3 [153], and no HCl -related etching or Ga desorption occurs [231]. Also, the higher concentration of chlorine at the interface would tend to retard growth, as free Cl , HCl , or Cl_2 would tend to remove gallium from the surface. A side effect of this would be improved crystal quality, if surface diffusion was rapid enough, but this is not the case for GaN grown in the H-MOVPE reactor.

The speciation of the AP-MOVPE and LP-MOVPE cases follows the same general trends as the HVPE case, with one exception. Gallium is found principally as GaH , or $\text{Ga}_{(v)}$ at higher temperatures, because these and $\text{Ga}_2_{(v)}$ represent the only possible Ga -containing vapor-phase species. For the HVPE case, either GaCl_3 or GaCl is the predominant vapor-phase species. Other species, such as N_2 , H_2 , NH_3 , and CH_4 , are essentially similar in the HVPE and AP-MOVPE cases.

In terms of speciation, the differences between the atmospheric-pressure and low-pressure cases are twofold. First, the NH_3 mole fraction is a full order of magnitude lower at low pressure. From a practical perspective, this increased NH_3 decomposition means more active nitrogen is present at the wafer surface. Secondly, the transition from GaH to $\text{Ga}_{(v)}$ occurs at lower temperature, and the mole fraction of $\text{Ga}_{(v)}$ is slightly (20.3%) higher.

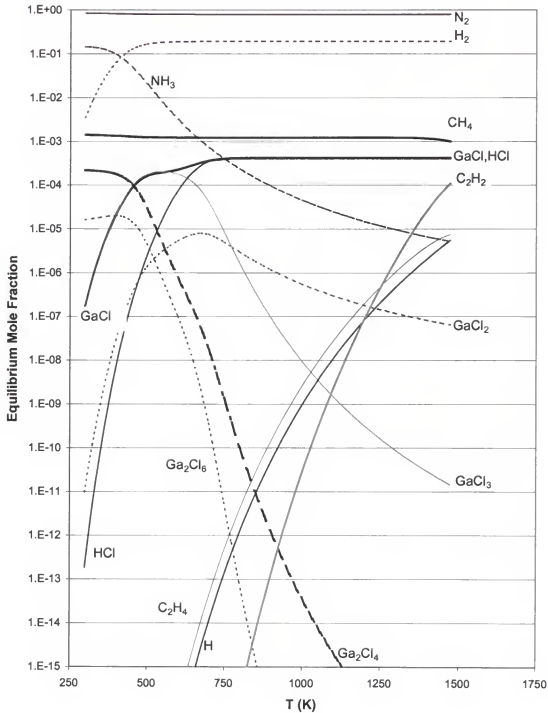


Fig. 4-1. Concentrations of most abundant equilibrium species as a function of temperature for HVPE gas-phase case. Fixed parameters were $P = 1$ atm, $T = x$ axis, $C/Ga = 3$, $Cl/Ga = 2.0$, and $y_{NH_3}^0 = 0.147$ (corresponding to $F_{NH_3} = 500$ sccm).

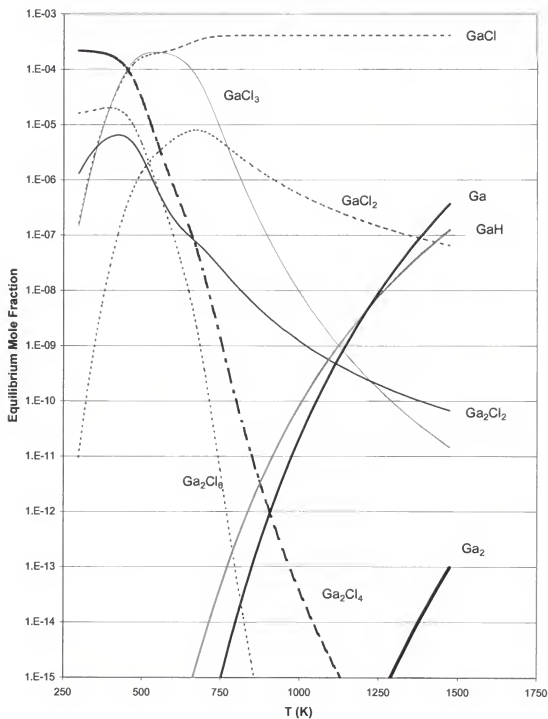


Fig. 4-2. Concentration of gallium-containing species with temperature for HVPE gas-phase case. Fixed parameters were $P = 1$ atm, $T = x$ axis, $C/\text{Ga} = 3$, $\text{Cl}/\text{Ga} = 2.0$, and $y_{\text{NH}_3}^0 = 0.147$ (corresponding to $F_{\text{NH}_3} = 500$ sccm).

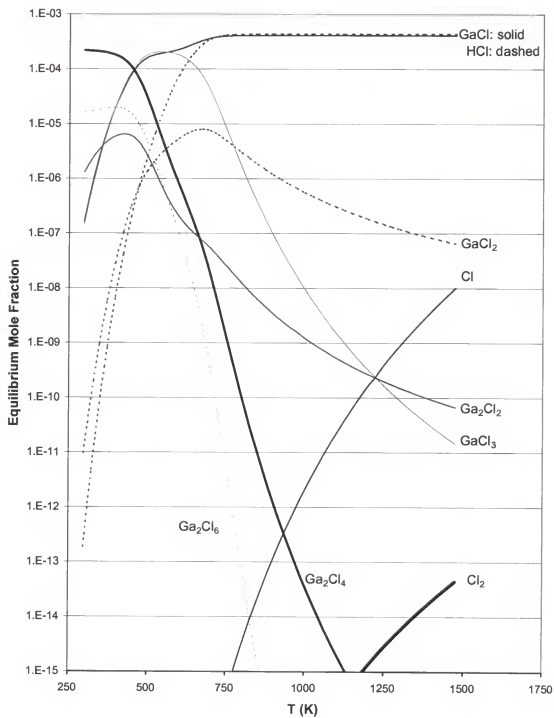


Fig. 4-3. Variation of chlorine-containing species with temperature for HVPE gas-phase case. Fixed parameters were $P = 1$ atm, $T = x$ axis, $C/Ga = 3$, $Cl/Ga = 2.0$, and $y_{NH_3}^0 = 0.147$ (corresponding to $F_{NH_3} = 500$ sccm).

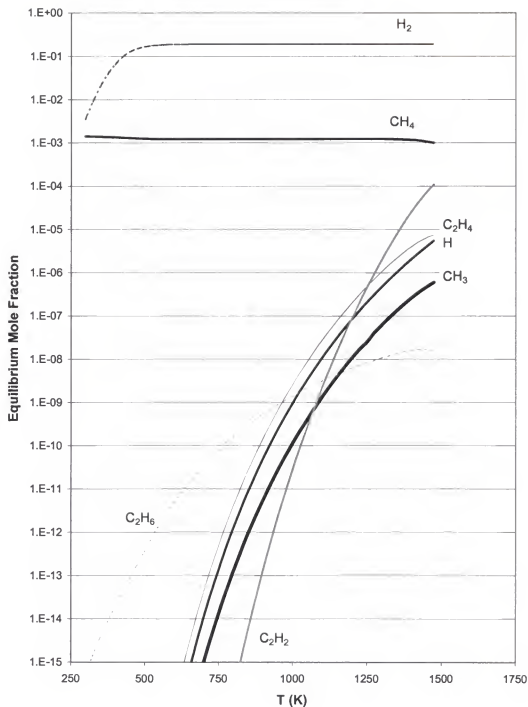


Fig. 4-4. Variation of hydrocarbon and hydrogen species with temperature for HVPE gas-phase case. Fixed parameters were $P = 1$ atm, $T = x$ axis, $C/Ga = 3$, $Cl/Ga = 2.0$, and $y_{NH_3}^0 = 0.147$ (corresponding to $F_{NH_3} = 500$ sccm).

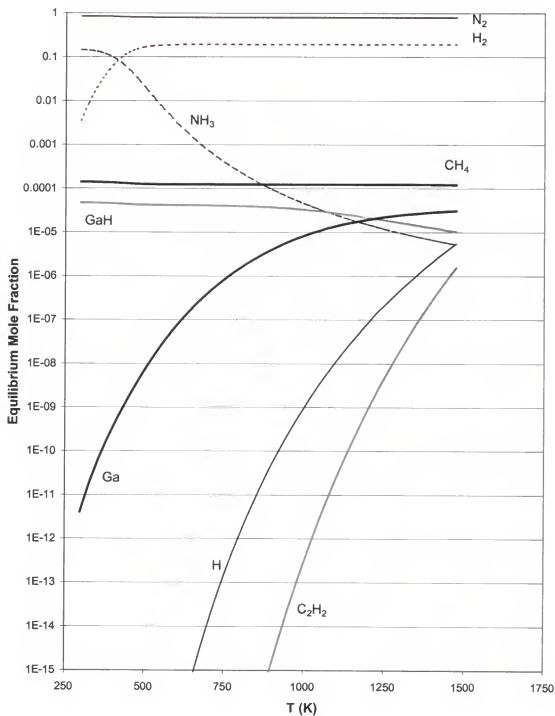


Fig. 4-5. Concentrations of most abundant equilibrium species as a function of temperature for AP-MOVPE gas-phase case. Fixed parameters were $P = 1$ atm, $T = x$ axis, $C/\text{Ga} = 3$, $\text{Cl}/\text{Ga} = 0$, and $y_{\text{NH}_3}^0 = 0.147$ (corresponding to $F_{\text{NH}_3} = 500$ sccm).

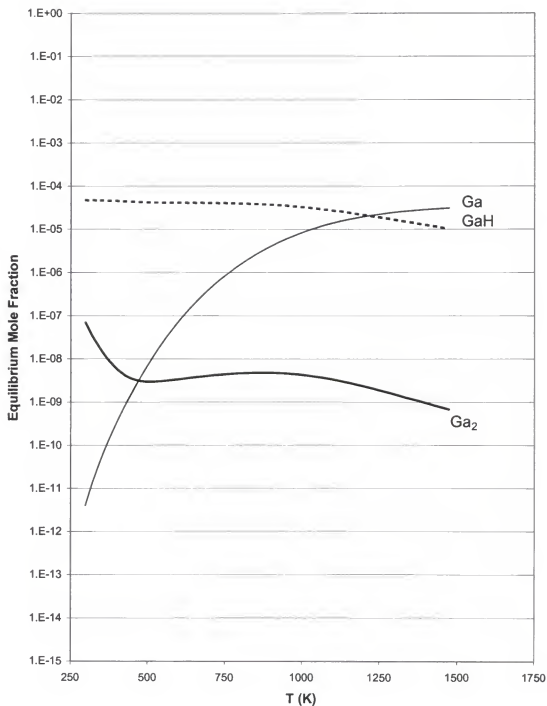


Fig. 4-6. Concentration of gallium-containing species with temperature for AP-MOVPE gas-phase case. Fixed parameters were $P = 1$ atm, $T = x$ axis, $C/Ga = 3$, $Cl/Ga = 0$, and $y_{NH_3}^0 = 0.147$ (corresponding to $F_{NH_3} = 500$ sccm).

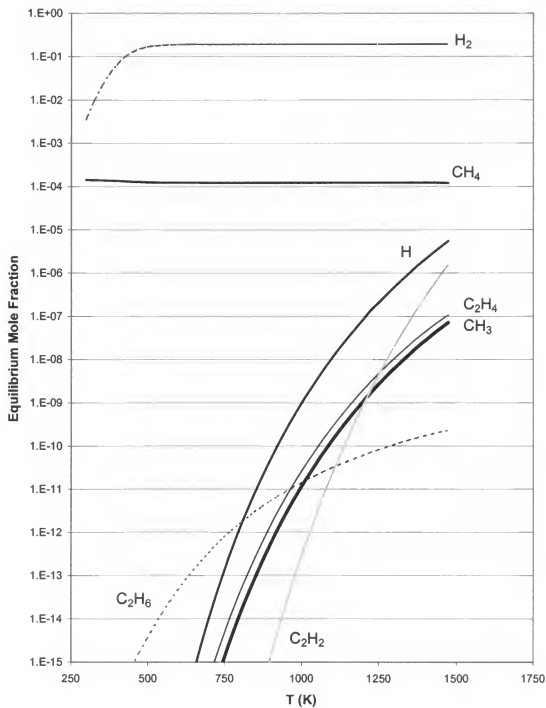


Fig. 4-7. Variation of hydrocarbon and hydrogen species with temperature for AP-MOVPE gas-phase case. Fixed parameters were $P = 1$ atm, $Cl/Ga = 0.0$, $y_{NH_3}^0 = 0.147$ (corresponding to $F_{NH_3} = 500$ sccm).

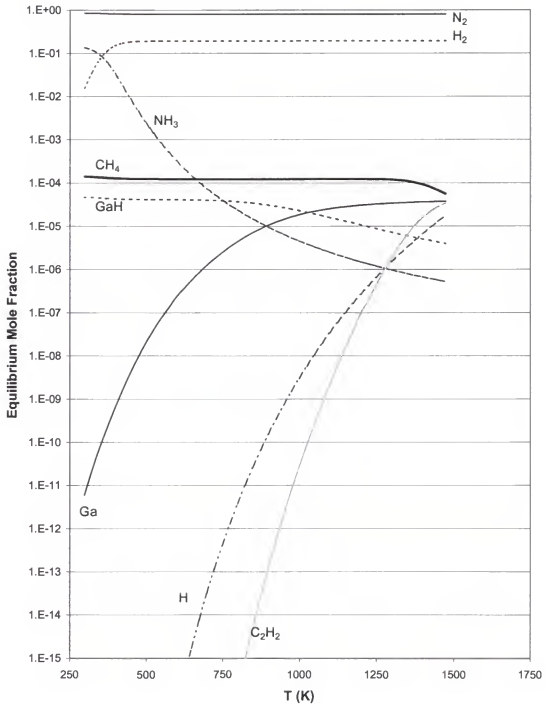


Fig. 4-8. Concentrations of most abundant equilibrium species as a function of temperature for LP-MOVPE gas-phase case. Fixed parameters were $P = 0.1$ atm, $T = x$ axis, $C/Ga = 3$, $Cl/Ga = 0.0$, and $y_{NH_3}^0 = 0.147$ (corresponding to $F_{NH_3} = 500$ sccm).

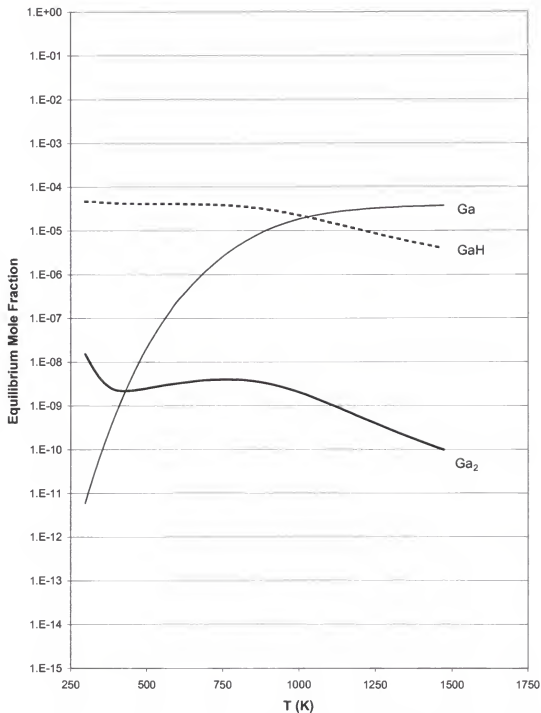


Fig. 4-9. Concentration of gallium-containing species with temperature for LP-MOVPE gas-phase case. Fixed parameters were $P = 0.1$ atm, $T = x$ axis, $C/Ga = 3$, $Cl/Ga = 0.0$, and $y_{NH_3}^0 = 0.147$ (corresponding to $F_{NH_3} = 500$ sccm).

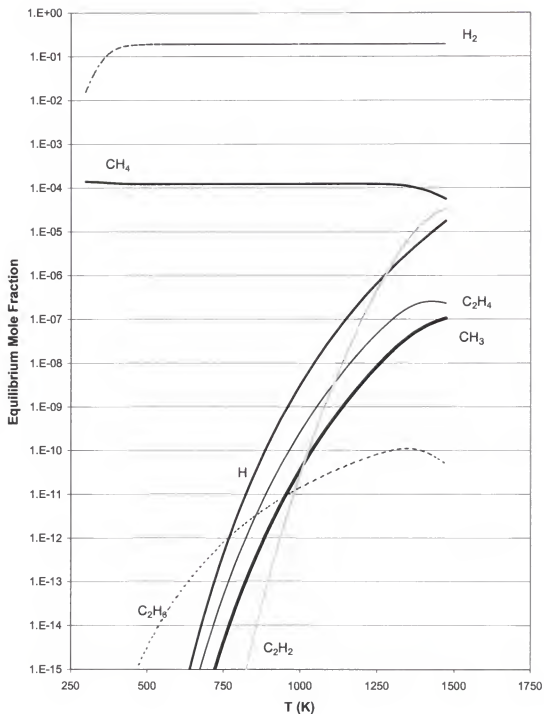


Fig. 4-10. Variation of hydrocarbon and hydrogen species with temperature for LP-MOVPE gas-phase case. Fixed parameters were $P = 0.1$ atm, $T = x$ axis, $C/Ga = 3$, $Cl/Ga = 0.0$, and $y_{NH_3}^0 = 0.147$ (corresponding to $F_{NH_3} = 500$ sccm).

The gas phase for HVPE, AP-MOVPE, and LP-MOVPE growth regimes were modeled primarily to provide baselines for comparison with thermodynamic systems that included condensed phases. From the analysis, speciation trends were predicted that were comparable to reported trends in the literature [153].

Calculations with liquid phase rejection

The next step toward modeling the thermodynamic behavior of the H-MOVPE system involved including solid phases, specifically ammonium chloride and $\text{GaN}_{(s)}$, in addition to the gas phase. This system most nearly represents the actual growth conditions, as these are the complete set of phases found in GaN deposition in the H-MOVPE reaction system in the temperature range. While liquid phase gallium is possible—GaN can decompose, for instance, in H_2 atmospheres at high temperature—the growth rates typically encountered in experimental growth are much higher than the decomposition rate [230]. Furthermore, excess chlorine tends to remove liquid gallium from the reaction system. Therefore, from a practical modeling perspective, this system is the most descriptive of the three investigated.

Figure 4-11 shows the P-T phase diagram for the HVPE case. All allowed phases are present. Three results are apparent from this diagram. First, at typical growth temperatures, only the gas phase is present. This result is not predictive, but rather indicative that GaN is unstable or metastable at typical growth temperature. The markers indicate experimental results where $\text{GaN}_{(s)}$ formed in the H-MOVPE growth system.

This result further indicated that the second feature of the graph, the positive slope of the gas/gas+GaN phase boundary, was not an accurate predictor of the GaN deposition regime. This line also showed that GaN is more stable at higher pressures.

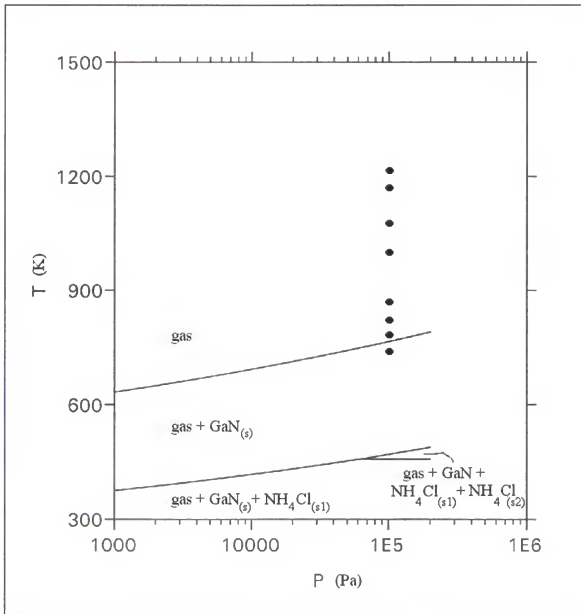


Fig. 4-11. P-T phase diagram for HVPE GaN growth under standard flow conditions of 500 sccm NH_3 and 2.0 HCl/Ga ratio, constrained without gallium liquid. Pressure range from 1 to 20 kPa (0.01 to 2 atm) is displayed. Markers indicate formation of $\text{GaN}_{(s)}$ in H-MOVPE experiments.

Finally, Figure 4-11 predicts the formation of one or two types of ammonium chloride at low temperature for the HVPE case. This, at least, is predictive. Ammonium chloride deposits on all cooler parts of the reactor, including the gate valve, exhaust lines, and even (by thermal diffusion) the most upstream section of the inlet.

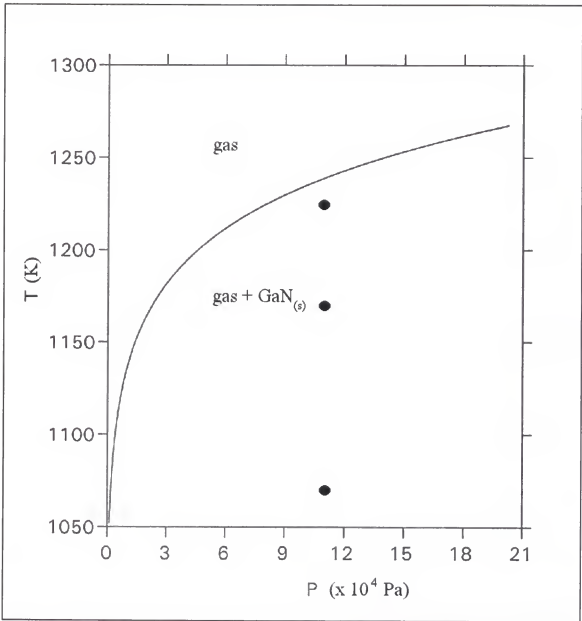


Fig. 4-12. P-T phase diagram for MOVPE GaN growth under standard flow conditions of 500 sccm NH_3 , constrained without gallium liquid. Pressure range from 1 to 20 kPa (0.01 to 2 atm) is displayed. Markers indicate formation of $\text{GaN}_{(s)}$ in H-MOVPE experiments.

Figure 4-12 shows the P-T phase diagram for the MOVPE case. Over the range of pressure examined, the range of temperature conducive to GaN growth is much higher than for the HVPE case, and the maximum growth temperature is significantly higher. Although the H-MOVPE system only reaches temperatures of $\sim 950^\circ\text{C}$ (1223 K), reports

of other researchers have a deposition temperature under similar conditions of up to 1100°C (1373 K) [241, 242]. Thus this diagram also underestimates the stability of GaN.

The speciation of the HVPE system is diagrammed in Figures 4-13 through 4-15. The most salient feature of these graphs results from the sublimation of ammonium chloride above 448 K. From a growth perspective, the equilibrium amount of gallium nitride in the system decreases significantly as the amount of chlorine found in the gas phase increases twenty-fold, as seen in Figure 4-13 below. Also notable in this figure is the decrease of GaN with increasing temperature, and the predicted upper limit of growth as 748K at a 2:1 Cl/Ga ratio.

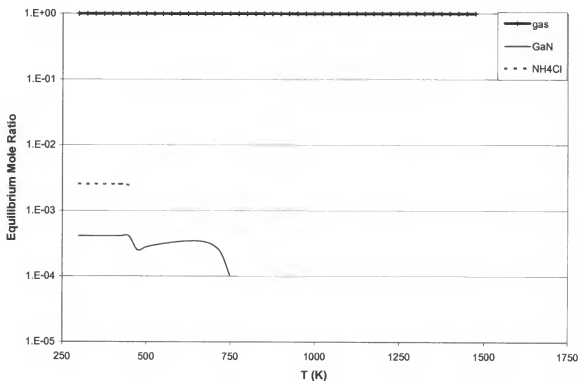


Fig. 4-13. Relative abundance of phases as a function of temperature for HVPE case, constrained without gallium liquid. Fixed parameters were $P = 1$ atm, $T = x$ axis, $C/Ga = 3$, $Cl/Ga = 2.0$, and $y_{NH_3}^0 = 0.147$ (corresponding to $F_{NH_3} = 500$ sccm).

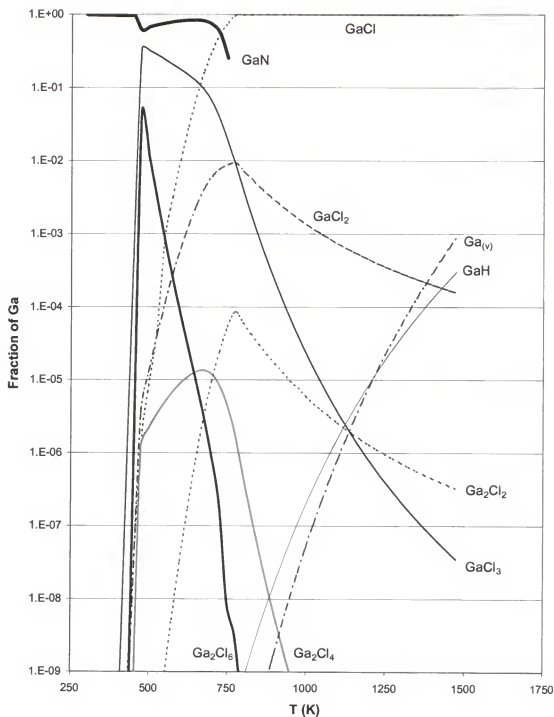


Fig. 4-14. Relative distribution of gallium in gallium-containing species, as a function of temperature for HVPE case, constrained without gallium liquid. Fixed parameters were $P = 1$ atm, $T = x$ axis, $C/Ga = 3$, $Cl/Ga = 2.0$, and $y_{NH_3}^0 = 0.147$ (corresponding to $F_{NH_3} = 500$ sccm).

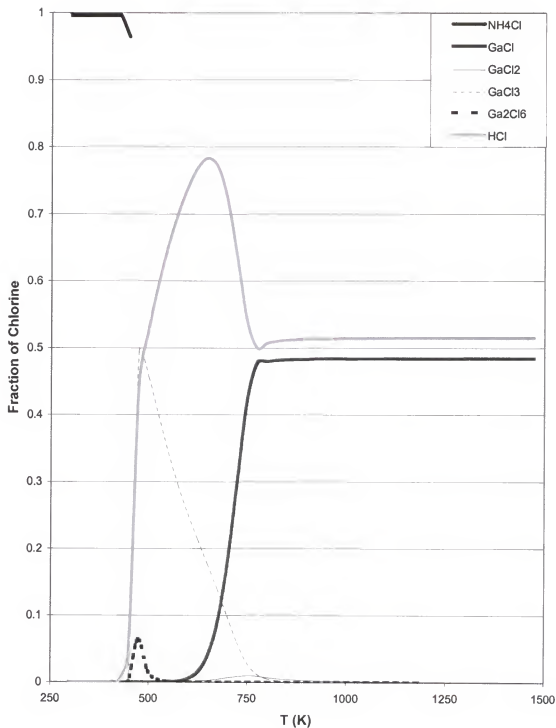


Fig. 4-15. Relative distribution of chlorine in chlorine-containing species, as a function of temperature for HVPE case, constrained without gallium liquid. Fixed parameters were $P = 1$ atm, $T = x$ axis, $C/Ga = 3$, $Cl/Ga = 2.0$, and $y_{NH_3}^0 = 0.147$ (corresponding to $F_{NH_3} = 500$ sccm).

The other speciation trends found in Figures 4-14 and 4-15 also reflect this onset of abundant chlorinated species from evaporation of the ammonium chloride. Gallium trichloride becomes the repository of a majority of the gallium in the gas phase, and HCl and GaCl₃ become the predominant chlorine-containing species at 448 K. GaCl becomes increasingly abundant, as well, at higher temperatures as GaCl₃ becomes less so.

The phase behavior and speciation trends with temperature (Figs. 4-16 through 4-19) for the AP-MOVPE and LP-MOVPE cases are somewhat less interesting. In both cases, the predicted deposition amount of gallium nitride is unaffected by temperature until near the decomposition temperature for the given pressure (Figs. 4-16 and 4-18). By means of comparison, the value of 99.9% of the horizontal asymptotic value (4.1×10^{-5} mole fraction) occurs at 1073 K for the atmospheric-pressure case, and 998 K for the low-pressure case. The mole fraction decreases further, until the decomposition temperature is reached.

Speciation trends for both MOVPE cases were practically identical to the gas phase analyses, but for the gallium-containing species. As shown in Figures 4-17 and 4-19, GaN is the principal Ga-containing species up to the decomposition temperature, at which point Ga_(v) and to a lesser extent GaH become abundant.

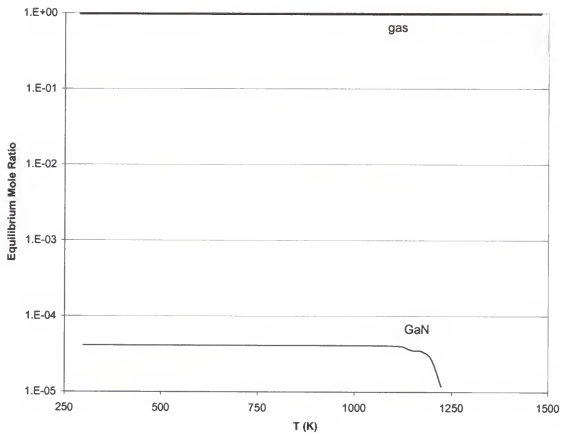


Fig. 4-16. Relative abundance of phases as a function of temperature for AP-MOVPE case, constrained without gallium liquid. Fixed parameters were $P = 1$ atm, $T = x$ axis, $C/Ga = 3$, $Cl/Ga = 0.0$, and $y_{NH_3}^0 = 0.147$ (corresponding to $F_{NH_3} = 500$ sccm).

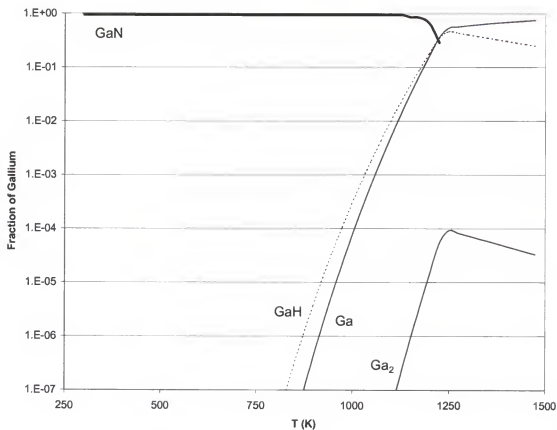


Fig. 4-17. Relative distribution of gallium in gallium-containing species, as a function of temperature for AP-MOVPE case, constrained without gallium liquid. Fixed parameters were $P = 1$ atm, $T = x$ axis, $C/Ga = 3$, $Cl/Ga = 0.0$, and $y_{NH_3}^o = 0.147$ (corresponding to $F_{NH_3} = 500$ sccm).

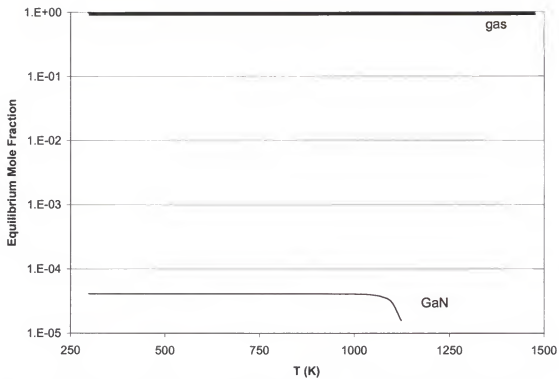


Fig. 4-18. Relative abundance of phases as a function of temperature for LP-MOVPE case, constrained without gallium liquid. where $P = 0.1$ atm, $T = x$ axis, $C/Ga = 3$, $Cl/Ga = 0.0$, and $y_{NH_3}^0 = 0.147$ (corresponding to $F_{NH_3} = 500$ sccm).

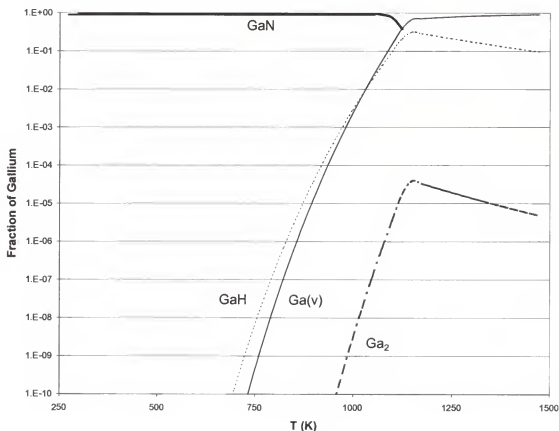


Fig. 4-19. Relative distribution of gallium in gallium-containing species, as a function of temperature for LP-MOVPE case, constrained without gallium liquid. Fixed parameters were $P = 0.1$ atm, $T = x$ axis, $C/Ga = 3$, $Cl/Ga = 0.0$, and $y_{NH_3}^0 = 0.147$ (corresponding to $F_{NH_3} = 500$ sccm).

The overall analysis of the phase behavior and speciation trends of the HVPE, AP-MOVPE, and LP-MOVPE systems revealed that the equilibrium analysis predicts that MOVPE permits deposition at higher growth temperature than HVPE, and higher pressures also permit higher growth temperature. Trends in the distributions of chemical species were similar to the gas phase, but for gallium-containing species and chlorine-containing species just above the sublimation temperature of ammonium chloride.

Calculations with liquid phase present

The final system analyzed included liquid gallium ($\text{Ga}_{(l)}$) among the condensed phases, as well as those mentioned previously. While this phase generally doesn't appear in typical HVPE or MOVPE growth, except as a reactant in the source zone of HVPE, it is a potential decomposition product of GaN at high temperature.

For the HVPE case, no difference was found in either speciation or the phase diagram. For the typical case of $\text{Cl}/\text{Ga} = 2.0$, sufficient chlorine was present to restrain the gallium to the GaN and the set of gallium chloride species.

The difference in the phase behavior upon the addition of $\text{Ga}_{(l)}$ occurs for the MOVPE case. $\text{Ga}_{(l)}$ exists at a higher temperature than $\text{GaN}_{(s)}$ exists under the previous (no $\text{Ga}_{(l)}$) case. Furthermore, in this case the $\text{GaN}_{(s)}$ is present only until ~ 1023 K, in contrast to the ~ 1223 K phase boundary when $\text{Ga}_{(l)}$ is excluded.

Figure 4-20 shows the P-T phase diagram for the MOVPE case. From this figure, it is seen that, depending upon pressure, there is a 250 to 300K window at any given pressure where the gas+ $\text{Ga}_{(l)}$ mixture is stable. This region is astride the phase boundary for the gas/gas+ $\text{GaN}_{(s)}$ phases for the previous treatment. This figure also shows the increased stability of the condensed phases with increased pressure.

As may be seen from the figure, and comparison with Figure 4-12, the experimental data support the contention that the methodology of rejecting the liquid phase from the calculations is the most accurate method for the prediction of phase behavior during crystal growth.

Figure 4-20 shows the difference in Gibbs energy (G_{dep}) as a function of temperature between the gas phase and condensed phase systems for all cases, with and

without the liquid gallium phase added to the computations. G_{dep} is defined as the Gibbs energy of the solid phase system less the Gibbs energy of the gas phase system ($-G_{\text{dep}}$ is the actual quantity plotted, in order to aid in presentation). For systems that result in deposition, this energy difference should be negative, as energy is released upon condensation.

Strictly speaking, G_{dep} should be used only for equilibria that form GaN(s) , but for convenience it will be applied to all equilibria. Since addition of the liquid phase to the HVPE case resulted in no change in the results, only one line is plotted. The results are plotted against a constant gallium flux to normalize the results. The kinked nature of the MOVPE lines occurs due to rounding error in the database; error bars of $6.25 \times 10^3 \text{ J/mol}$ are omitted for clarity.

Several features are apparent from this graph, and go far toward understanding the thermodynamic behavior of the system. First, when G_{dep} is zero, no deposition occurs since the only stable phase is the gas phase. This conclusion ignores surface energies of formation, stress, and polarity effects, which can affect the actual temperature locus where G_{dep} is zero. Further discussion of these effects may be found in Mastro [230].

Points A, B, and C on Figure 4-20 are phase transitions. Point A is the boundary between the $(\text{gas} + \text{GaN}_{(\text{s})} + \text{NH}_4\text{Cl}_{(\text{s})})$ region of stability and the $(\text{gas} + \text{GaN}_{(\text{s})})$ region. Points B and C are the bifurcation where liquid Ga becomes stable with increased temperature, instead of solid GaN, in calculations where $\text{Ga}_{(\text{l})}$ was retained as a condensed phase.

Finally, both MOVPE chemistries are farther away from equilibrium—their G_{dep} is an order of magnitude higher—than the HVPE chemistry. This is well known in the

literature [229]. As a general rule, the closer the system is to equilibrium (i.e. $G_{\text{dep}} = 0$), the higher the crystal quality, and therefore HVPE should have the potential for production of GaN films of better crystallinity than MOVPE.

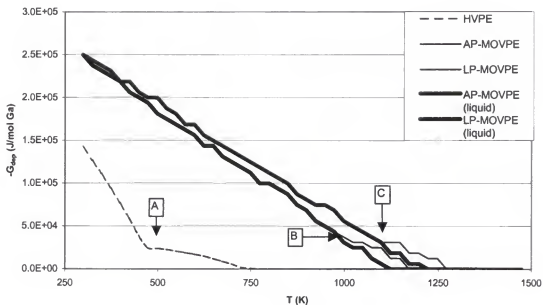


Fig. 4-20. Variation with temperature of the magnitude of G_{dep} , the difference in Gibbs energies of the gas-phase-only and the condensed-phase systems, for HVPE, AP-MOVPE, and LP-MOVPE. Gibbs energies are plotted per mole of TMG reactant. Point A is the phase transition where NH_4Cl disappears from the system. Points B and C are the bifurcation where liquid Ga is stable, instead of solid GaN, in calculations where $\text{Ga}_{(l)}$ was retained as a condensed phase.

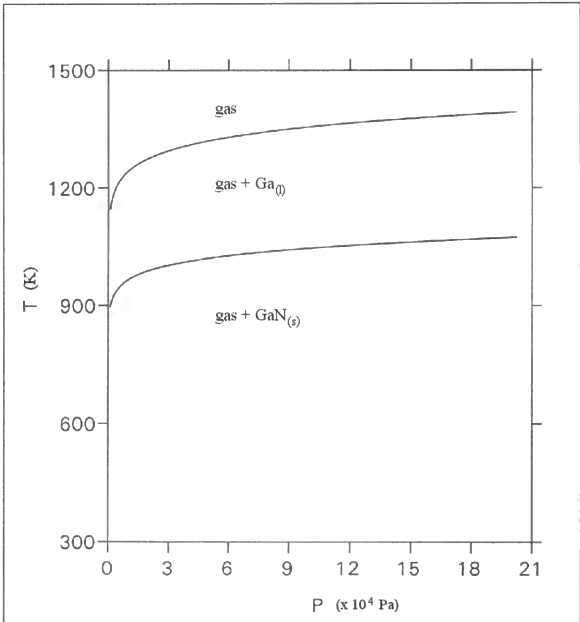


Fig. 4-21. P-T phase diagram for MOVPE GaN growth under standard flow conditions of 500 sccm NH_3 , gallium liquid included. Pressure range from 1 to 20 kPa (0.01 to 2 atm) is displayed. Fixed parameters were $P = x$ axis, $T = y$ axis, $C/\text{Ga} = 3$, $Cl/\text{Ga} = 0.0$, $y_{\text{NH}_3}^0 = 0.147$ (corresponding to $F_{\text{NH}_3} = 500$ sccm).

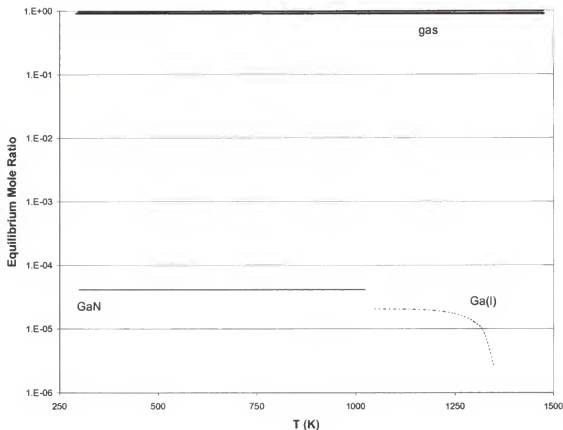


Fig. 4-22. Relative abundance of phases as a function of temperature for AP-MOVPE case, gallium liquid included. Fixed parameters were $P = 1$ atm, $T = x$ axis, $C/\text{Ga} = 0$, $\text{Cl}/\text{Ga} = 0.0$, $y_{\text{NH}_3}^0 = 0.147$ (corresponding to $F_{\text{NH}_3} = 500$ sccm).

Figure 4-22 and 4-23 respectively show the phase behavior and speciation of the Ga-containing species for the AP-MOVPE case. Of significance is the phase transition from $\text{GaN}_{(s)}$ to $\text{Ga}_{(l)}$ at 1048K. This immediately results in half as many moles of atoms in the condensed phase (as the N reverts to the gas), though the great majority of the Ga merely changes from $\text{GaN}_{(s)}$ to $\text{Ga}_{(l)}$ as seen in Figure 4-22. While this effect is not seen in film deposition, it has been described in annealing studies [230]. Thus, with enough time GaN will dissociate at high temperatures; however, during typical crystal growth, the growth rate far outpaces the decomposition rate, and thus the effect is not observed.

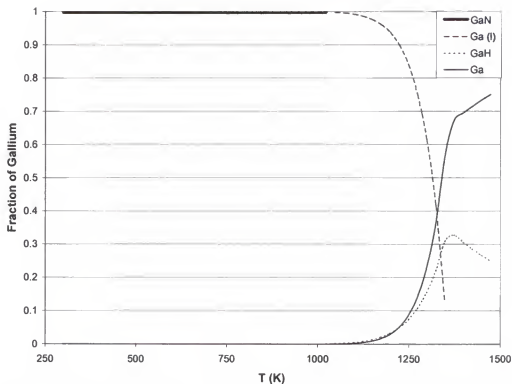


Fig. 4-23. Relative distribution of gallium in gallium-containing species, as a function of temperature for AP-MOVPE case, gallium liquid included. Fixed parameters were $P = 1$ atm, $T = x$ axis, $C/Ga = 3$, $Cl/Ga = 0.0$, $y_{NH_3}^0 = 0.147$ (corresponding to $F_{NH_3} = 500$ sccm).

The LP-MOVPE behavior with liquid gallium included in the computations is shown in Figures 4-24 and 4-25. Compared to the AP-MOVPE case, $Ga(l)$ occurs at a lower temperature. Furthermore, when compared to the liquid-excluded case, the condensed phases (here specifically $Ga_{(l)}$) extend to higher temperatures, but the high-temperature limit of $GaN(s)$ stability is much lower. Both of these results expand upon the phase diagram (Fig. 4-21). The speciation trends also are similar to those in the liquid-excluded case (Fig. 4-19).

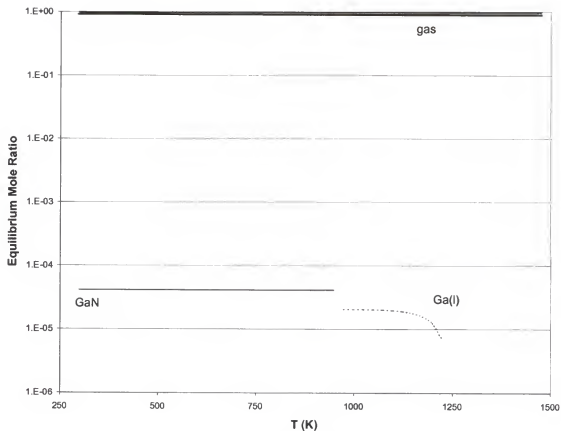


Fig. 4-24. Relative abundance of phases as a function of temperature for LP-MOVPE case, gallium liquid included. Fixed parameters were $P = 1$ atm, $T = x$ axis, $C/Ga = 3$, $Cl/Ga = 0.0$, $y_{NH_3}^0 = 0.147$ (corresponding to $F_{NH_3} = 500$ sccm).

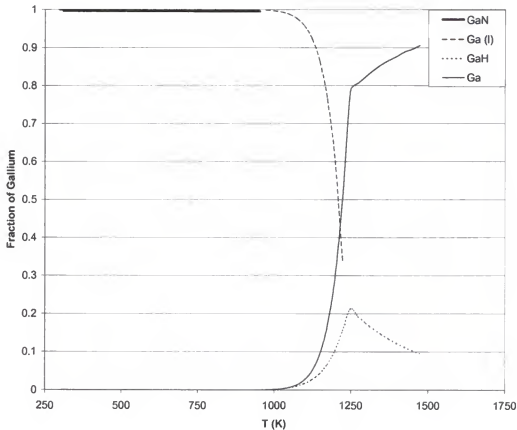


Fig. 4-25. Relative distribution of gallium in gallium-containing species, as a function of temperature for LP-MOVPE case, gallium liquid included. Fixed parameters were $P = 0.1$ atm, $T = x$ axis, $C/Ga = 3$, $Cl/Ga = 0.0$, $y_{NH_3}^0 = 0.147$ (corresponding to $F_{NH_3} = 500$ sccm).

Conclusions

A complete thermodynamic investigation was performed on the subject of the response of the H-MOVPE chemistry to temperature variation. HVPE, AP-MOVPE, and LP-MOVPE growth regimes were examined, and the phase behavior and speciation trends for each were examined and compared. It was found that, while the approach of including liquid gallium as a possible reactant was strictly correct, it was less accurate for the description of growth experiments than the approach of rejecting the liquid phase

from the computations. Experimental growth data supported liquid phase rejection, while annealing studies confirmed GaN decomposition. Thus, the preferable description of the system depends upon whether the desired insight pertains to the growth behavior or to the post-growth film stability.

Equilibrium Calculations for the H-MOVPE System: Cl/Ga Variation

Aside from the state variables of temperature and pressure, the H-MOVPE growth system contains species representing the five elements of chlorine, gallium, hydrogen, nitrogen, and carbon. To analyze the variation of flows upon the phase and speciation behavior of the system, four natural ratios of elements emerge. Since the gallium flow is kept invariant throughout all of the analyses in this work, and since GaN growth rates are generally determined by the gallium flow rate, it becomes natural to adopt gallium as the denominator in all parameters. Thus, the natural ratios are: N/Ga, C/Ga, Cl/Ga, and H/Ga.

The variation of N/Ga has been studied extensively by Davydov, and will not be repeated here [6, 238]. The amount of carbon in the system is constrained by the amount of gallium, because the only reactant source for carbon is TMG, which is also the only reactant source for gallium. Thus, for this system, the ratio of carbon to gallium is a constant and invariable 3:1. The two natural ratios that will be studied in this work are Cl/Ga and tangentially, H/Ga.

The Cl/Ga ratio was investigated for insight into its thermodynamic behavior. As mentioned in Chapter 3, this parameter directly affects growth rate, crystal quality, and surface morphology. In practical terms, this parameter is represented by the HCl flow rate, given a constant TMG flow rate. Unless otherwise specified, the system was

calculated for the standard HVPE conditions of 1223 K (950°C), atmospheric pressure, and a start composition of 2894 cm³ of N₂, 1.6 cm³ TMG, 500 cm³ NH₃, and 0 to 9.6 cm³ HCl. For this treatment, the starting amount of TMG was kept constant, and N₂ was displaced to increment HCl. These values represented the total reactant flows for one minute of HVPE growth in the H-MOVPE system.

Figure 4-26 shows the phase diagram describing the variation with temperature and Cl/Ga ratio. Four regions are present: two low-temperature regions with ammonium chlorides, a region where GaN(s) is stable, and a region where the gas phase is the only stable phase. Overset on this diagram are H-MOVPE experimental data points.

The most significant feature of the phase boundaries is the transition from mixed MOVPE/HVPE to HVPE behavior at Cl/Ga = 1.0. This boundary describes the condition for which sufficient Cl is in the system to react all the less-stable TMG to GaCl. GaCl is replacing TMG in a one-to-one correspondence, and the abruptness of this transition represents the stability of the GaCl molecule relative to GaN under these conditions, when compared to TMG relative to GaN.

Two other features not apparent upon this plot, but reflected in the equilibrium calculations, were the linearly increasing quantity of GaN from the gas+GaN_(s)/gas transition line to the Cl/Ga = 0 (MOVPE) line, and the linearly increasing quantity of ammonium chloride at low temperature with increasing Cl/Ga. Both of these trends result from the inherent stability of these compounds at the given temperature; in effect, these compounds act like an eigenvalue or sink for an element (Ga, Cl) in the system, in that each contains almost the totality of a particular element in the system under the given conditions, up to nearly the limits of composition.

The experimental data are from system qualification and optimization runs (Chapter 3). Open circles in Figure 4-26 represent runs in which no GaN growth occurred on the sapphire wafer. No data are plotted outside of the growth temperature range of $723\text{ K (}450^{\circ}\text{C)} < T_g < 1223\text{ K (}950^{\circ}\text{C)}$. The lower limit is constrained by the kinetic decomposition rate of NH_3 , and the upper is the highest attainable growth temperature. As may be seen, while the slope of the theoretical curve is approximately followed by the experimental data, wide discrepancy exists for the location of the $\text{gas}+\text{GaN}_{(s)}/\text{gas}$ boundary.

This discrepancy illustrates the fact that GaN CVD growth occurs far from thermodynamic equilibrium. The driving force for CVD deposition is generally high, compared to near-equilibrium techniques such as LPE [229]. The rate of decomposition/sublimation/etching of GaN is so much lower— $0.5\text{ }\mu\text{m/hr}$ in hydrogen and negligible in nitrogen, according to Mastro et al. [230]—than the rate of deposition that the experimental data is skewed toward increased stability for GaN in the solid phase. While beyond the scope of this work, this behavior can be modeled by the addition of a temperature-dependent kinetic barrier to the thermodynamic stability of the $\text{GaN}_{(s)}$ species, thus artificially decreasing the Gibbs energy. Further investigation of this concept is one of the recommendations of this work.

Figure 4-27 shows the phase diagram for the case where $\text{Ga}_{(l)}$ is included in the calculations of equilibrium under the aforementioned standard HVPE conditions. Experimental results are overlaid upon the plot. The only significant difference between this phase diagram and the previous one (Fig. 4-26) is the existence of a $\text{gas}+\text{Ga}_{(l)}$ region bounded between $\text{Cl/Ga} = 0.0$ and (generally) 1.0 , and at the lower temperature limit by T

~ 1050 K ($\sim 875^\circ\text{C}$). Also, while the semi-sigmoid shape of this region is similar to the $\text{gas} + \text{GaN}_{(s)}$ region of the previous diagram, the upper boundary with the gas phase is everywhere at a higher temperature.

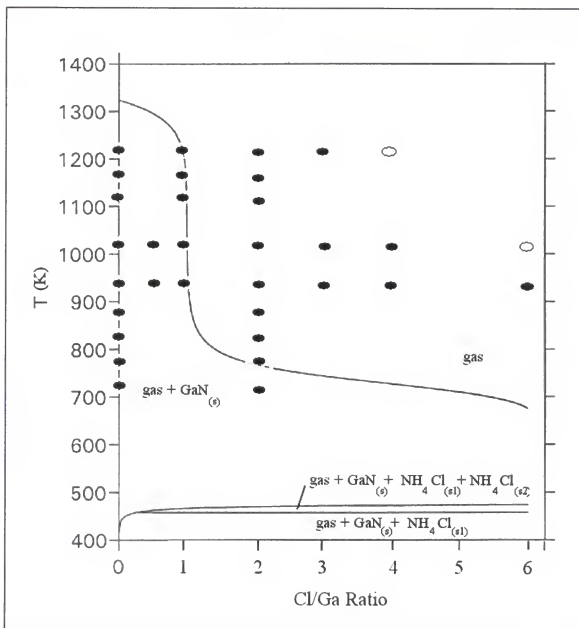


Fig. 4-26. Phase diagram showing variation in phase behavior with Cl/Ga ratio, constrained without liquid gallium. Closed circles indicate GaN(s) deposition in experiments, while open circles indicate no deposition. Fixed parameters were $P = 1$ atm, $T = y$ axis, $C/\text{Ga} = 3$, and $y_{\text{NH}_3}^0 = 0.147$ (corresponding to $F_{\text{NH}_3} = 500$ sccm).

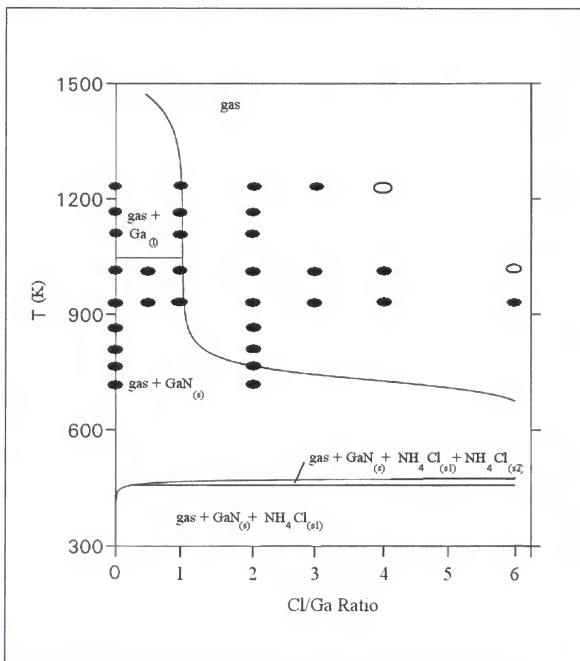


Fig. 4-27. Phase diagram showing variation in phase behavior with Cl/Ga ratio, constrained with liquid gallium. Closed circles indicate GaN(s) deposition in experiments, while open circles indicate no deposition. Fixed parameters were $P = 1$ atm, $T = y$ axis, $C/Ga = 3$, and $y_{NH_3}^0 = 0.147$ (corresponding to $F_{NH_3} = 500$ sccm).

The experimental data clearly delineate which calculation works better for modeling growth conditions. Under no growth conditions was liquid gallium observed on the substrate or in the reactor. MOVPE growth ($\text{Cl}/\text{Ga} = 0$) produced GaN(s) films under all temperature conditions. While this suggests that rejecting liquid gallium from the calculations produces a more descriptive model, the case may again be made that the growth system is not in thermodynamic equilibrium, and thus while the model is descriptive it is not accurate.

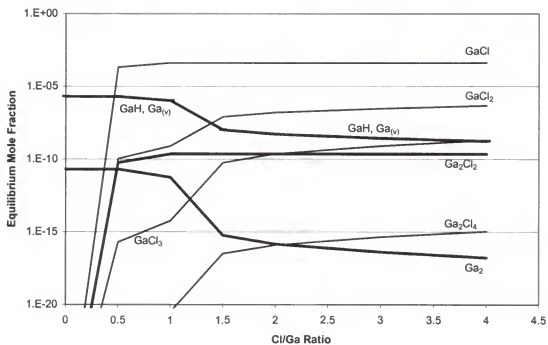


Fig. 4-28. Relative distribution of gallium in gallium-containing species, as a function of Cl/Ga ratio, for computations including gallium liquid. Fixed parameters were $T = 1223\text{K}$ (950°C), $P = 1\text{ atm}$, $\text{C}/\text{Ga} = 3$, and $y_{\text{NH}_3}^0 = 0.147$ (corresponding to $F_{\text{NH}_3} = 500\text{ sccm}$).

Figures 4-28 through 4-30 show the trends in speciation with increasing Cl/Ga. The most descriptive feature is shown in Figure 4-29. From this diagram, it may be seen that gallium monochloride substitutes in a one-to-one basis for gallium liquid as the principal gallium species, and that beyond the 1:1 Cl/Ga ratio, additional chlorine primarily forms HCl.

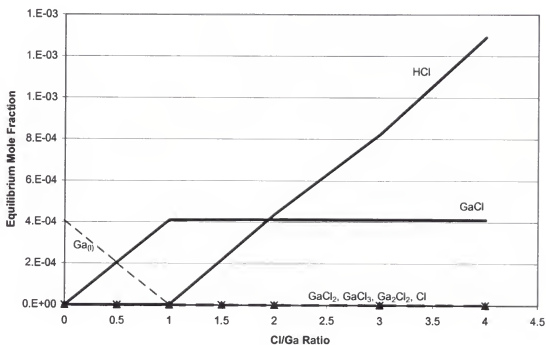


Fig. 4-29. Linear plot of chlorinated species abundance as a function of Cl/Ga ratio. Liquid gallium plotted for reference. Fixed parameters were $T = 1223\text{K}$ (950°C), $P = 1$ atm, $C/\text{Ga} = 3$, and $y_{\text{NH}_3}^0 = 0.147$ (corresponding to $F_{\text{NH}_3} = 500$ sccm).

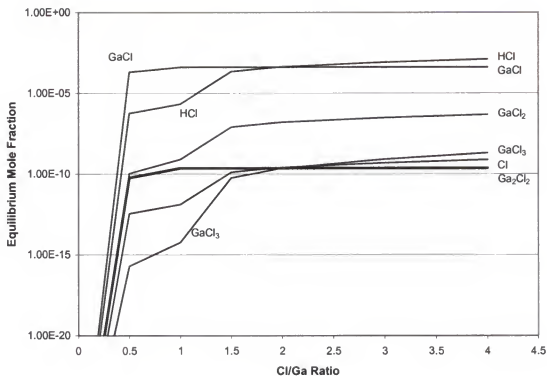


Fig. 4-30. Logarithmic plot of chlorinated species abundance as a function of Cl/Ga ratio, for computations including gallium liquid. Fixed parameters were $T = 1223\text{K}$ (950°C), $P = 1\text{ atm}$, $C/\text{Ga} = 3$, and $y_{\text{NH}_3}^0 = 0.147$ (corresponding to $F_{\text{NH}_3} = 500\text{ sccm}$).

In conclusion, the Cl/Ga behavior of the H-MOVPE system was modeled, and the theoretical phase behavior was compared with growth experiments. It was found that the modeling was most accurate when the liquid phase was excluded from the calculations, although large differences between predicted and experimental behavior existed. Speciation graphs showed that gallium was found principally as GaCl to the limit of the chlorine present, and that excess gallium was distributed principally as GaN or Ga_(l) depending upon the constraints imposed upon the calculations.

Equilibrium Calculations for the H-MOVPE System: NH_3 Variation

Of the natural parameters for the HVPE system, N/Ga and H/Ga are the most complicated, as nitrogen and hydrogen occur in multiple input species, and thus the increase of a single reactant species does not necessarily proportionally affect the N/Ga or H/Ga ratio. Furthermore, NH_3 provides the anion in the $\text{GaN}_{(s)}$ pure compound, and thus NH_3 significantly affects both N/Ga and H/Ga ratios. Despite this caveat, the bulk of the hydrogen (95% or more) atoms present in the chemistry react from the NH_3 precursor, and since this was a natural process variable, NH_3 was used as the basis to explore the system thermodynamics.

The speciation graphs for variation of the NH_3 flow are shown in Figures 4-31 and 4-32. The most important feature of these graphs is the predicted decomposition of NH_3 and subsequent effect of the H_2 generated according to



This H_2 tends to shift the equilibrium of all species save for HCl and GaCl . Multiple-chlorinated species such as GaCl_3 shift their equilibria toward GaCl plus HCl . Carbon is nearly completely found as CH_4 , so its mole fraction changes only minutely, but free $\text{C}_{(v)}$ in the gas phase decreases significantly, as expected, from



These shifts upon increasing ammonia flow rate, and thus, increasing equilibrium hydrogen mole fraction, are presented in Figure 4-33 for the most abundant and most sensitive species, and in Figure 4-34 for the gallium-containing species. The figures represent the ratio of the gas phase mole fraction of a particular species at a given NH_3 flow to its mole fraction at $F_{\text{NH}_3} = 500$ sccm.

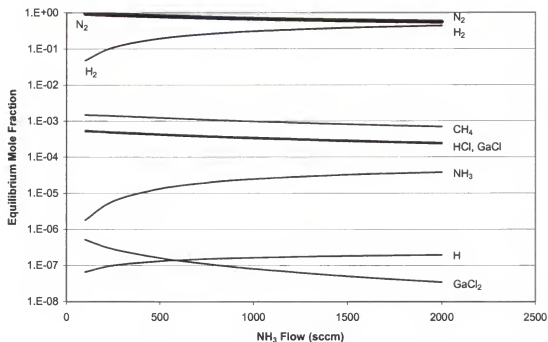


Fig. 4-31. Variation of gas phase composition with ammonia flow rate. Fixed parameters were $T = 1223\text{K}$, $P = 1\text{ atm}$, $F_{\text{NH}_3} = x\text{ axis}$, $C/\text{Ga} = 3$, and $\text{Cl}/\text{Ga} = 2.0$.

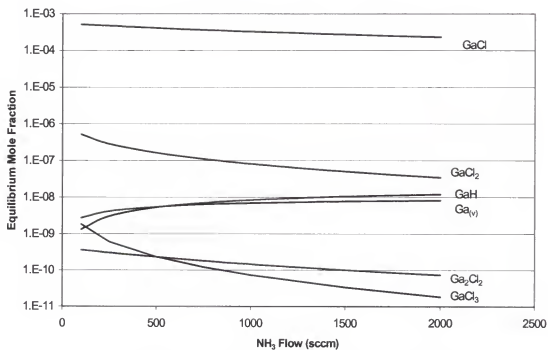


Fig. 4-32. Variation of gallium-containing species with ammonia mole fraction. Fixed parameters were $T = 1223\text{K}$, $P = 1\text{ atm}$, $F_{\text{NH}_3} = x\text{ axis}$, $C/\text{Ga} = 3$, and $\text{Cl}/\text{Ga} = 2.0$.

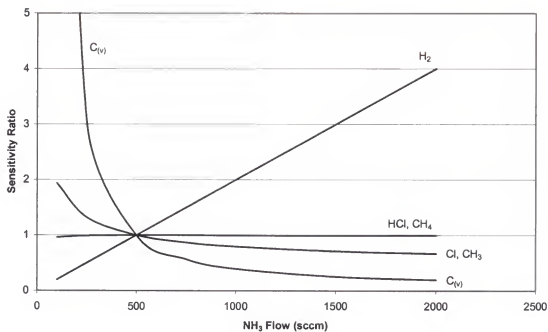


Fig. 4-33. Sensitivity of various major chemical species to NH₃ input mole fractions, shown in correspondence with equivalent process flow. Sensitivity ratio is the ratio of gas phase equilibrium mole fraction at the given input mole fraction of NH₃, to the gas phase equilibrium mole fraction at $y_{\text{NH}_3}^0 = 0.147$ (corresponding to $F_{\text{NH}_3} = 500$ sccm).

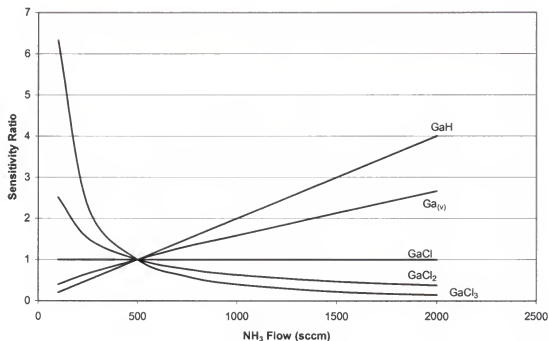


Fig. 4-34. Sensitivity of various gallium-containing species to NH_3 input mole fractions, shown in correspondence with equivalent process flow. Sensitivity ratio is the ratio of gas phase equilibrium mole fraction at the given input mole fraction of NH_3 , to the gas phase equilibrium mole fraction at $x_{\text{NH}_3}^0 = 0.147$ (corresponding to $F_{\text{NH}_3} = 500$ sccm).

Summary

The complex chemical equilibrium of the H-MOVPE system have been explored for both HVPE and MOVPE growth regimes. Equilibria were calculated for cases that restricted all species to the gas phase, that permitted condensed phases but for liquid gallium, and that permitted condensed phases including liquid gallium. Phase diagrams were generated for ranges of temperature and pressure, and to study the effect of changing system parameters such as Cl/Ga ratio and NH_3 flow rate. These predictions were then compared with experiment, and it was found that experimental data most

closely followed the calculations in which condensed phases were permitted except for liquid gallium.

Speciation plots were generated showing the variation of species with temperature, Cl/Ga ratio, and NH_3 flow rate. These graphs showed that the introduction of chlorine into the system acted as a sink for the gallium, and that the increase in hydrogen resulting from increasing the process ammonia flow rate would significantly affect the equilibrium behavior of the gallium chlorides and free carbon in the vapor.

CHAPTER 5

MODELS OF NITRIDE SOLID SOLUTIONS

The purpose of this chapter is to explore details of the thermodynamics of solid solutions of (B,Al,In)GaN alloys. Models describing nitride solutions reported in the literature are based upon relationships between the lattice constants and heats of atomization of pure component, covalent cubic semiconductors. Unfortunately, nitrides are generally neither entirely covalent nor cubic, and thus the assumptions must be questioned upon which the previous models rest.

To remedy this shortcoming, two models of nitride solid solutions were developed to predict interaction energies for the regular solution model. First, the heat of atomization data were evaluated strictly for the wurtzite semiconductors, instead of using a database that combined data from both cubic and wurtzite structures. Secondly, a model was developed to account for ionic contributions to bonding energy.

Thermodynamics of [B,Al, In]GaN Solid Solutions

Compound semiconductor solid solutions are generally engineered to provide a specific band gap energy, index of refraction, or lattice parameter to layers in electronic devices. Each of these properties depends upon the composition of the solid solution. Thermodynamics offers the CVD process engineer a tool to predict the compositions of these solutions from standard process variables such as temperature, pressure, and flow rates of gaseous reactants. Also, thermodynamics may be used to identify stable and

unstable alloy compositions, which provides insight into potential materials failure mechanisms, such as diffusion and phase separation.

This section will briefly review the primary models of solution thermodynamics, and explore the thermodynamic behavior of nitride solid solutions.

The Delta Lattice Parameter Model

Solid solution thermodynamics of compound semiconductors are typically modeled using regular solution theory and the Delta Lattice Parameter (DLP) model to predict the interaction energy [243]. Under this theory, the distribution of atoms on a binary group-III lattice is random, and therefore the excess entropy of mixing is zero. Furthermore, the enthalpy of mixing for the binary solution is given by the relation

$$\Delta H^M = x(1-x)\Omega_{AB} \quad (5-1)$$

where x is the mole fraction of component A or B and Ω is the temperature independent interaction energy [244]. The interaction parameter Ω_{AB} is evaluated by noting that

$$\Delta H^M = (1-x)\Delta H_A^{at} + x\Delta H_B^{at} - \Delta H_{alloy}^{at} \quad (5-2)$$

where ΔH^{at} is the enthalpy of atomization, corresponding to a bonding energy. Using the Phillips-Van Vechten model of dielectric bonding in covalent cubic semiconductors, Stringfellow then posited the bonding energy to be related to the lattice parameter a_0 by

$$\Delta H^{at} = K a_0^{-2.5} \quad (5-3)$$

The -2.5 power law dependence of ΔH^{at} upon the lattice constant originates from covalent bonding theory [245]. Realizing that $\Omega_{AB} = 4\Delta H^M$ at the equimolar composition, and transforming variables $\Delta = a_A - a_B$ and $\bar{a} = \frac{1}{2}(a_A + a_B)$, this becomes

$$\Omega_{AB} = 4.375K \frac{\Delta^2}{(\bar{a})^{4.5}} \quad (5-4)$$

Fitting Equation 5-3 to experimental data for binary phosphide, arsenide, antimonide, IV-IV, and available II-VI cubic systems yielded to Stringfellow a mean value for K of 4.81×10^7 J/mol (1.15×10^7 cal/mol). Using this value for K , the interaction parameters for the nitride alloys are given in Table 5-1. The second row of values lists the interaction parameters calculated by Matsuoka, who recomputed K by adding atomization energies for wurtzitic nitrides to the data set used by Stringfellow [246,247]. To get the equivalent cubic lattice constant, Matsuoka transformed the wurtzite lattice constants by geometric means described later [248-250]. The larger set of values is believed to be a computational error, as the lesser set agrees with calculations, is proportional to the greater, and is most recently referenced. While this recomputed K , 3.18×10^7 J/mol (7.6×10^6 cal/mol), fits InGaN miscibility gap data very well, Edgar claims that Stringfellow's original proportionality constant optimally fits the accumulated nitride solution data [246, 247].

Table 5-1. Interaction parameters for several nitride alloys (cal/mol). Values in bold were calculated using reported linearizations constants K , but not mentioned in reference text. Matsuoka's larger set of interaction parameters were likely calculation errors.

	AlN	AlGa	InGa	BGa	AlIn	References
Basic DLP	54,900	1,090	9,600	70,700	18,600	246, 247
Matsuoka	33,400	672 1,090	6,560 10,700	43,100	11,400 18,500	248, 249 250

The Valence Force Field Model

While the DLP model is semi-empirical, continuing increases in computer processing power have recently permitted first-principles calculations of mixing energies.

The only model applied to calculate interaction parameters for nitride solutions at the time of this writing is the Valence Force Field (VFF) model of Keating [251].

This model describes the alloy crystalline lattice using statistical mechanics, by approaching the crystal as a series of N-centered tetrahedra. Each of the different vertices of a tetrahedron is permitted to be any of the cations (Al, Ga, In). These tetrahedra are fixed at positions determined by the virtual-crystal approximation (VCA), which entails a perfect crystalline lattice. The several permutations are given probabilities in this fashion.

The strain energy E_m is written for each tetrahedron as

$$E_m = \frac{3}{8} \sum_{i=1}^4 \alpha_i \frac{(d_i^2 - d_{i0}^2)^2}{d_{i0}^2} + \frac{6}{8} \sum_{i=1}^4 \sum_{j=i+1}^4 \frac{\beta_i + \beta_j}{2} \frac{(\mathbf{d}_i \cdot \mathbf{d}_j + d_{i0} d_{j0} / 3)^2}{d_{i0} d_{j0}} \quad (5-5)$$

where d_i is the distance between the center atom and a corner atom in the tetrahedron, and the $d_{i,j0}$ are the equilibrium bond lengths in the pure binary nitride. α and β are the bond stretching and bond bending force constants. To obtain the enthalpy of mixing, the product of the strain energies and their respective probabilities are summed over the permutation space for each of the unique linearizations.

This model was applied to [In, Ga]N systems by Ho and Stringfellow, using force constants from Kim et al. [252] By permitting the lattice to relax from the VCA to minimize the strain energy, they found an interaction parameter that was compositionally dependent, as well as dependent upon the number of shells relaxed. In the dilute limit, the indium-rich solution (InN:Ga) interaction parameter was calculated to be 5.63 kcal/mole, and the gallium-rich solution (GaN:In) interaction parameter was calculated to be 6.32 kcal/mole. Ho and Stringfellow used the average value, 5.98 kcal/mole, in subsequent calculations of GaN:In solubility, binodal and spinodal curves, and critical

temperature for phase separation [253-255]. The VFF model was applied to other alloy systems, and while detailed analyses of these systems were not given, select interaction parameters are listed in Table 5-2.

Takayama et al. recently applied the VFF theory to the whole range of [B,Al,Ga,In]N ternaries to generate interaction parameters for BAlN, BGaN, and BInN, as well as those already calculated [256]. Interestingly, the interaction parameter for InGaN was different from those calculated by Ho and Stringfellow (7.81 vs. 5.98 kcal/mol). This may be the result of using slightly different lattice constants for the pure compounds as the d_{io} and d_{jo} terms in the strain energy expression ($a = 3.162\text{\AA}$ vs. $a = 3.189\text{\AA}$ for GaN, for instance), since the force constants used were identical.

Table 5-2: Nitride interaction parameters (kcal/mol) predicted by the VFF model.

Alloy	Ω_{AB} (DLP)	Ω_{AB} (VFF)	Reference
AlGaN	1.19	0.87	253, 254
		0.72	256
AlInN	17.45	11.44	253, 254
		13.5	256
InGaN	9.60	5.98	253, 254
		7.81	256
AlPN	19.68	36.56	253, 254
AlAsN	57.93	53.42	253, 254
GaPN	28.90	27.38	253, 254
GaAsN	42.78	36.84	253, 254
InPN	19.68	16.33	253, 254
InAsN	26.71	21.87	253, 254
BAlN	54.87	30.40	256
BGaN	70.73	45.20	256
BInN	--	93.20	256

Other Numerical Modeling

Outside of the calculation of interaction parameters to describe binary nitride solutions, two groups have attempted to use first-principles calculations to predict other aspects of solid solution behavior.

Ito used the empirical Khor-Das Sarma (KD) expression for the interatomic potential V_{ij} to model solution thermodynamics at 0 K [257-259]:

$$V_{ij} = A \exp \left[-\beta(r_{ij} - R_i)\gamma \right] \left[\exp(-\theta r_{ij}) - B_0 \exp(-\lambda r_{ij}) G(\eta) / Z_i^\alpha \right] \quad (5-6)$$

In the above expression, r_{ij} is the interatomic distance, Z_i the coordination number of atom i , R_i the minimum interatomic distance, and $G(\eta)$ a bond bending term. According to Ito, A , B_0 , θ , λ , α , β , and γ are empirical parameters determined by the enthalpy of formation, cohesive energy, bulk modulus, and the relative stabilities of various crystal structures.

The principal results of the calculation were equilibrium lattice parameters and 0 K mixing energies. A partial listing of results is shown in Table 5-3, and the 0 K mixing energy was multiplied by four to obtain the interaction parameter. No calculational details were presented in their papers, save that the modeled lattice was a monolayer cubic (forced $c = a$) superlattice [257]. No attempts were specifically made to account for the wurtzite structure of the nitrides, ionicity, or multiple superlattices.

Ito attempted to compare the results with the DLP theory, and obtained comparable though consistently lower enthalpies of mixing. A problem in his calculations was that his interaction parameters calculated using Stringfellow's DLP constant consistently disagreed with Stringfellow's calculations by up to 74% (for AlNP), especially for Al-containing compounds [229]. This suggests that the lattice constants

used for the Ito's DLP analysis (which weren't explicitly reported), were incorrect for (at least) AlN. Despite this discrepancy with Al-containing compounds, the KD potential yields similar results to the DLP theory.

Table 5-3. Nitride mixing energies at equimolar compositions and interaction parameters predicted by the KD potential, in kcal/mol [257]. ΔH^m (S-DLP) are those calculated from Stringfellow [229], and ΔH^m (I-DLP) are those reported from Reference [257]. N. c. = not calculated in reference.

Alloy	ΔH^m (S-DLP)	ΔH^m (I-DLP)	ΔH^m (KD)	Ω_{AB} (KD)
AlGaN	0.30	0.00	0.00	0.02
AlInN	4.36	2.71	1.75	7.02
AlNP	4.92	8.58	6.57	26.29
AlNAs	14.48	11.73	9.62	38.48
AlNSb	n.c.	19.30	16.62	66.47
InGaN	2.40	2.41	1.54	6.14
GaN _P	7.23	8.04	5.93	23.70
GaNAs	10.70	10.96	8.28	33.12
GaNSb	n.c.	18.22	13.43	53.73
InNP	4.92	4.99	3.91	15.63
InNAs	6.68	6.61	5.19	20.75
InNSb	n.c.	11.46	9.91	39.66

The second group to investigate several aspects of nitride solid solutions was Zunger and coworkers, who used the VFF model with large (512 to 32768 atoms) supercells to model nitride/arsenide solid solutions [260]. While no interaction parameters were calculated, the band structures [260-263], surface energies [264], and ordering thermodynamics (short-range vs. long-range order) [262] were investigated.

A Wurtzite DLP Model

Despite this treatment, there is a potentially serious shortcoming to application of the DLP theory to nitride semiconductors. The DLP model was developed for cubic covalent systems, which have different, and more, symmetries in their band structure [83,

84]. The nitride family [B, Al, Ga, In]N is neither highly covalent nor most stable in the cubic structure.

By definition, any model that is based upon lattice constants must have a mechanism for adapting for different crystal structures. There are two approaches to transmutation. The first is to simply assume that the bonding distance in a compound is constant for any lattice structure that keeps the molar volume constant. Edgar and coworkers have used this approach [246, 247]. Both the wurtzite (hexagonal close packed) and zinblende (face-centered cubic) structures have the same molar volume, with packing factors of 0.866. By using geometry, the corresponding pseudocubic lattice constant for a wurtzite crystal is

$$a_{pc} = \sqrt[3]{3^{1/2} a^2 c} \quad (5-7)$$

Another possible approach is to repeat Stringfellow's analysis of the power law relationship and proportionality constant by using the data for covalent bonding energies of only the wurtzite semiconducting compounds. Either the 'a' or 'c' lattice constants could be used as bases for the relationship, if the volumes of the unit cell scaled as the cubes of these values. This recomputation could be performed for the pseudocubic case, as well. Matsuoka et al. [248-250] recomputed K, the coefficient in Equation 5-3, expressly for the nitrides, but did not restrict the atomization data to wurtzite semiconductors. He transformed the wurtzite compounds into cubic form by using Equation 5-7, and obtained a value of 3.18×10^7 J/mol (7.6×10^6 cal/mol). This work is the first to reevaluate the DLP theory using only wurtzite compounds.

Method

To calculate a new DLP coefficient expressly for wurtzite semiconductors, the enthalpy of atomization was obtained from Phillips for the following wurtzite semiconductors: BN, AlN, GaN, InN, ZnO, ZnS, CdS, CdSe, SiC [264]. The wurtzite-type mercury semiconductors HgS, HgSe, and HgTe were excluded from the data set, as their semi-metallic character ($E_g \sim 0$ eV) complicates the thermodynamic description of their bonding and atomization energies.

Table 5-4. Lattice constants for wurtzite compounds.

Material	Lattice constant (Å)			Ref.
	a	c	a_{pc}	
BN	2.556	4.205	3.624	246
AlN	3.112	4.982	4.372	185
GaN	3.189	5.186	4.505	110
InN	3.530	5.960	5.048	185
ZnO	3.250	5.207	4.567	266
ZnS	3.823	6.258	5.411	266
CdS	4.136	6.713	5.837	266
CdSe	4.299	7.012	6.078	266
SiC (4H)	3.076	5.048	4.357	266

The enthalpy of atomization ΔH^{at} was then plotted as a function of lattice parameter for 'a', 'c', and ' a_{pc} ' lattice constants [Table 5-4], and the best-fit power law relationship was found by the gradient-search method. In all cases, the $-2.5 (\pm 0.03)$ power law relationship was found, similar to the standard DLP model. Plotting the enthalpy of atomization against (lattice constant)^{-2.5} linearized the data, and the coefficient K was the slope of this line. The interaction parameter was then summarily computed from Equation 5-4 for each variation of lattice constant. Table 5-5 presents the results at the end of this section.

Regression vs. 'a' lattice constant

The power law relationship between the 'a' lattice constant and the heats of atomization for the wurtzite semiconductors, and their linearizations, are shown in Figures 5-1 and 5-2. The K value was found to be $3.174 \pm 0.001 \times 10^6 \text{ kcal/mol-}\text{\AA}^{-2.5}$. Three powers are plotted to demonstrate the variation with different powers, and to show that only a -2.5 exponential relates the heat of atomization to the lattice constant while having the required zero intercept (corresponding to an infinite lattice parameter and thus non-bonding). The abscissa, "reduced lattice constant," is merely the lattice constant of the compound raised to the appropriate power.

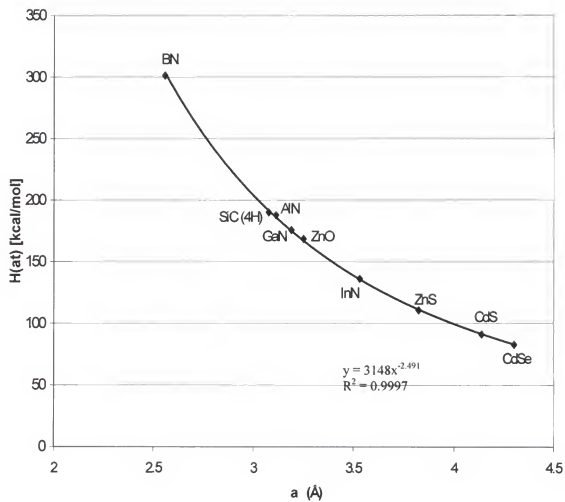


Fig. 5-1. Power law relationship between wurtzite 'a' lattice constant and enthalpy of atomization.

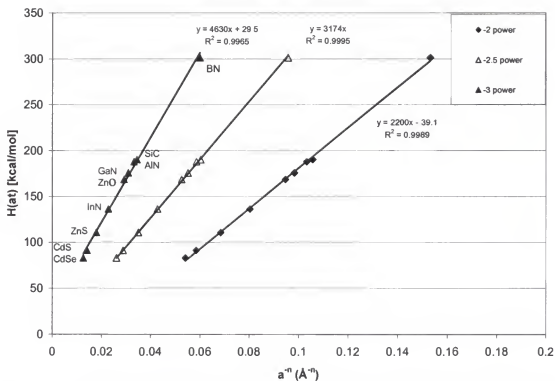


Fig. 5-2. Linearization of heat of atomization data against several powers of wurtzite 'a' lattice constant.

Regression vs. 'c' lattice constant of wurtzite compounds

The power law relationship between the 'c' lattice constant and the heats of atomization for the wurtzite semiconductors, and their linearizations, are shown in Figures 5-3 and 5-4. The K value was found to be $1.081 \pm 0.0029 \times 10^7 \text{ kcal/mol-}\text{\AA}^{-2.5}$.

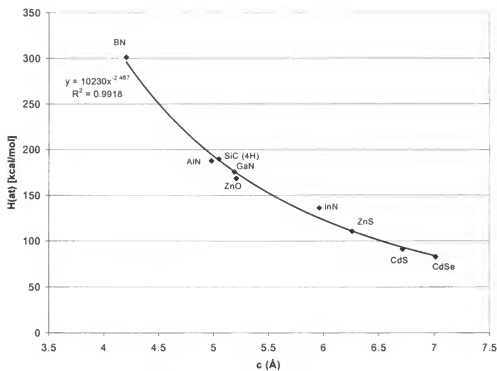


Fig. 5-3. Power law relationship between 'c' lattice constant and enthalpy of atomization.

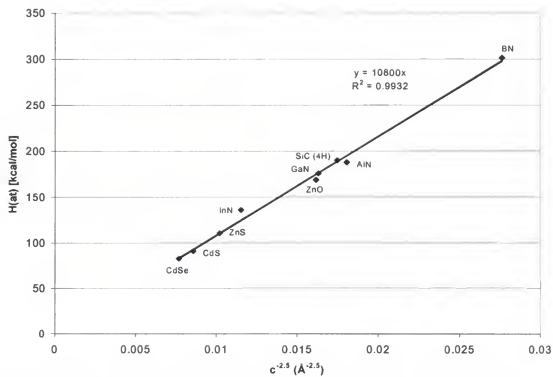


Fig. 5-4. Linearization of enthalpy of atomization data against 'c' lattice constant.

Regression vs. 'a_{pc}' lattice constant

This transformation uses Equation 5-14 to convert the lattice parameters for the wurtzite structure into a pseudo-cubic lattice parameter, similar to Edgar's and Matsuoka's work. The proportionality constant K was found to be $7.535 \pm 0.0031 \times 10^6$ kcal/mol-Å^{-2.5}, very similar to the 7.6×10^6 kcal/mol-Å^{-2.5} found by Matsuoka when using both cubic and wurtzite semiconductors. The power-law and linearizations graphs are shown in Figures 5-5 and 5-6.

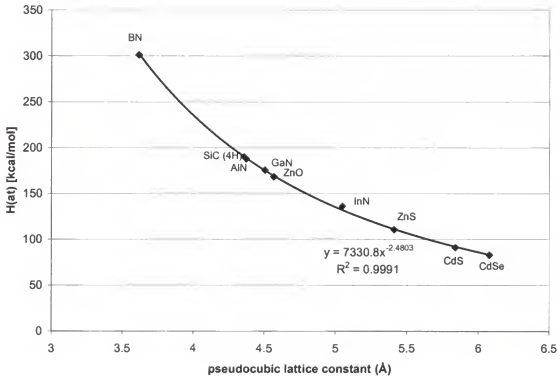


Fig. 5-5. Power law relationship between pseudocubic lattice constant and enthalpy of atomization.

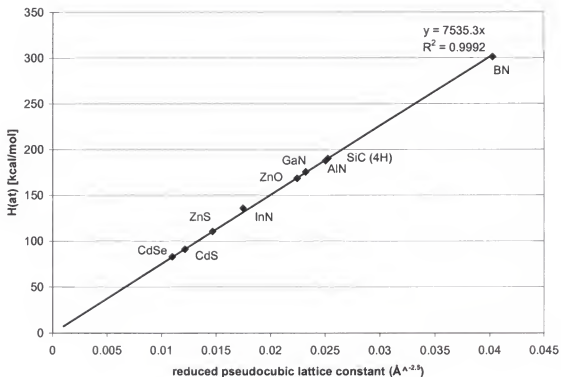


Fig. 5-6. Linearization of enthalpy of atomization data against pseudocubic lattice constant ' a_{pc} '.

Table 5-5. Proportionality constant and interaction parameters (in cal/mol) for three regressions of enthalpy of atomization data in the wurtzite DLP model.

	'a'	'c'	' a_{pc} '
K value ($\times 10^6$ kcal/mol- $\text{\AA}^{-2.5}$):	3.174 ± 0.001	10.810 ± 0.029	7.535 ± 0.0031
Ω_{AlGaIn}	471	1,344	708
Ω_{InGaIn}	6,916	12,331	8,560
Ω_{AlInIn}	10,945	29,759	14,104
Ω_{BAlIn}	39,531	29,957	36,157
Ω_{BGaIn}	48,219	43,453	46,525

The spinodal diagram for the $\text{In}_y\text{Ga}_x\text{Al}_{1-x-y}\text{N}$ system from the predicted interaction parameters for the wurtzite DLP model is shown in Figure 5-7, using the pseudocubic lattice parameters. All ternary interaction parameters are assumed to be zero. The mixing rule results used were from the strictly regular solution approximation (SRSA) of Onabe [268]:

$$(RT)^2 - 2RTM - (1 - x - y)xyL = 0 \quad (5-8)$$

$$M = (1 - x - y)x\Omega_{\text{InN-GaN}} + xy\Omega_{\text{GaN-AlN}} + (1 - x - y)y\Omega_{\text{AlN-InN}} \quad (5-9)$$

$$L = \Omega_{\text{InN-GaN}}^2 + \Omega_{\text{GaN-AlN}}^2 + \Omega_{\text{AlN-InN}}^2 - 2(\Omega_{\text{InN-GaN}}\Omega_{\text{AlN-InN}} + \Omega_{\text{GaN-AlN}}\Omega_{\text{AlN-InN}} + \Omega_{\text{AlN-InN}}\Omega_{\text{InN-GaN}}) \quad (5-10)$$

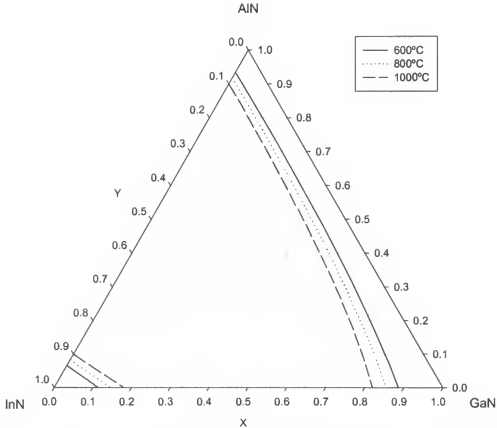


Fig. 5-7. Spinodal diagram for $\text{In}_y\text{Ga}_x\text{Al}_{1-x-y}\text{N}$, calculated from the pseudocubic wurtzite model interaction parameters.

Ionic + Covalent (I + C) Model

The DLP model is based upon thermodynamic data from systems in which bonding is either completely (C, Sn, Ge, Si) or predominantly ([Al,Ga, In][P, As, Sb], others) covalent. Electrons are shared nearly equally between the anion and the cation in covalent semiconductors. This simplifies the bond energy expression

$$E_g = E_h + iC, \quad (5-11)$$

where E_g is the total bond energy, E_h is the homeopolar (covalent) bonding energy, and C is the Pauling ionicity, which is a measure of the ionic bond strength. For covalent systems, $E_g \sim E_h$, since by taking the complex conjugates,

$$E_g^2 = E_h^2 + C^2 \quad (5-12)$$

By ignoring the contribution of the ionic term in Equation 5-19, the enthalpy of atomization is underestimated for ionic compounds in the DLP theory. A complete discussion of the relevance of the ionic character, especially in reference to oxides and nitrides, may be found in Phillips [245]; this theory merely attempts to explore an empirical inclusion of ionicity into the regular solution model.

To assess the interaction parameter accurately, the power relationship of ΔH^{at} and the lattice constant should be recomputed as well, since shape of the curve clearly changes, as may be seen in the top function in Figure 5-8. The other plotted functions are the ionic + covalent H^{at} for the cubic compounds, and below that just the covalent H^{at} for all compounds. An interesting feature of this graph is that wurtzite and cubic semiconductors clearly separate into two different functions.

The linearizations method used to generate the interaction parameters of the wurtzite-only model was applied to this hypothesis. Because the power dependency on

lattice constant changed from -2.5 to -1.5 , the complete expression for the interaction parameter was retained in Equations 5-1 and 5-2, instead of transforming variables per the DLP theory to an expression similar to Equation 5-4. The power law dependence was found to be -1.5 ± 0.04 , as shown in Figure 5-8. As a result, the expression for the interaction parameter became the following:

$$\Omega = 4.375K \left(\frac{1}{2} (a_a^{-1.5} + a_b^{-1.5}) - \left(\frac{a_a + a_b}{2} \right)^{-1.5} \right) \quad (5-13)$$

The same linearization procedure was used to calculate K as was used for the wurtzite-only data regression. A value of $2.33 \pm 0.392 \times 10^6 \text{ kcal/mol-}\text{\AA}^{-1.5}$ was calculated. A list of predicted interaction parameters for this model appears in Table 5-6.

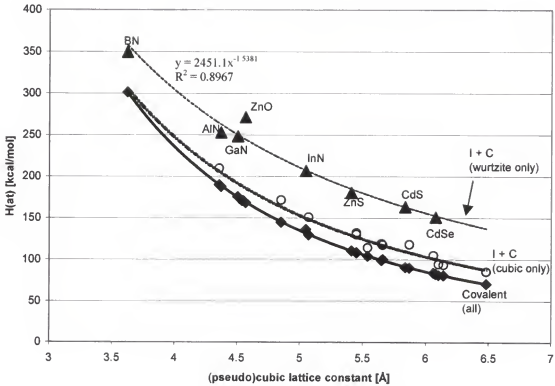


Fig. 5-8. Comparison of enthalpies of atomization for cubic and wurtzite semiconductors, with and without ionic contributions.

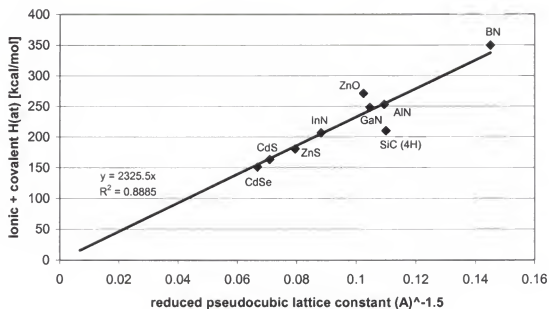


Fig. 5-9. Linearization of ionic + covalent enthalpies of atomization.

Table 5-6. Interaction parameters predicted by the ionic + covalent model with $K = 2.33 \times 10^6 \text{ kcal/mol-}\text{\AA}^{-1.5}$.

Alloy	Interaction parameter (cal/mol)
Ω_{AlGaIn}	416
Ω_{InGaIn}	5,430
Ω_{AlInIn}	8,850
Ω_{BAlIn}	19,300
Ω_{BGaIn}	25,400

Results and Discussion

One numerical and four semi-empirical models for the interaction parameter in the regular solution model have been presented either in the available literature or this work. Of the four semi-empirical models, three differ by the type of data used to

calculate the single fitting parameter, and the fourth expands the model to include ionic bonding. All are summarized in Table 5-7.

Table 5-7. Summary of interaction parameter predictions for various theories (cal/mol).

	DLP [245,246]	DLP with Nitride H ^{at} [247-249]	Wurtzite H ^{at} only, this work	I + C, Wurtzite H ^{at} , this work	Valence force field [251,253];[255]
$\Omega_{\text{AlGa}}\text{N}$	1,091	672	708	416	870; 720
$\Omega_{\text{InGa}}\text{N}$	9,600	6,559	8,560	5,431	5,980; 7,810
$\Omega_{\text{AlIn}}\text{N}$	18,636	11,366	14,104	8,846	11,440; 13,500
$\Omega_{\text{BAl}}\text{N}$	54,872	33,400	36,157	19341	30,400
$\Omega_{\text{BGa}}\text{N}$	70,730	43,053	46,525	25400	45,200

There are three typical techniques used to evaluate data for enthalpies of mixing for crystalline semiconductors: calorimetry, observation of miscibility gaps (phase separation), and regression of solid-vapor equilibrium (SVE) data. The latter two methods may be used to evaluate each of the models. Calorimetry cannot be used at this time, because pure-component boron, aluminum, and gallium nitride liquids require higher pressures than are currently available. Dissolution of alloys in liquid gallium, while calorimetrically possible, has not been reported in the literature.

Spinodal Diagrams: InGaN

Predictions of miscibility gaps are primarily accomplished by the use of spinodal diagrams. Growth of alloys with compositions inside the parabolic spinode cannot be performed by equilibrium or near-equilibrium growth techniques, because the alloy is unstable and will separate into regions of two phases. Figure 5-10 shows spinodes for InGaN for each of the model parameters presented in Table 5-7, along with literature data from cross-sectional transmission electron microscopy for several InGaN alloy

compositions and growth temperatures [249,270]. While care must be taken, as kinetic barriers may prohibit unstable compositions from segregating, those compositions that do not segregate may be used to establish the upper compositional limit of stability. Figure 5-11 shows the pseudo-ternary spinodal decomposition diagram for AlGaInN, using the same mixing rule as for the wurtzite model (see Equations 5-15 through 5-17).

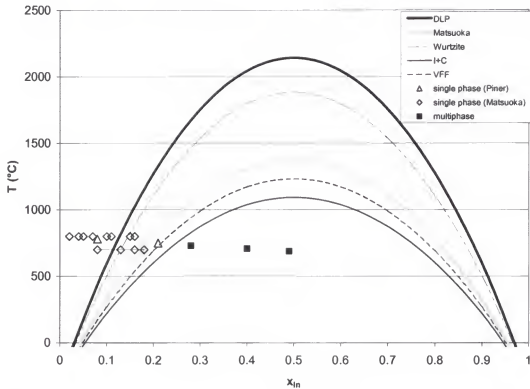


Fig. 5-10. Spinodal diagram showing spinodes of InGaN for several estimated values of Ω_{InGaN} . Data from Refs. [249],[270].

With the above caveat in mind, Figure 5-10 suggests that the DLP, wurtzite, and Matsuoka's re-regressed DLP models do not adequately predict the miscibility gap data, and only the VFF and ionic + covalent parametric values are within the upper compositional limit derived for the miscibility gaps for InGaN.

Several features are apparent from Figure 5-11. For all of the curves, the stability increases in the order $\text{AlInN} < \text{InGaN} < \text{AlGaIn}$, as seen from the length of the unstable segment along each axis. No segment exists along the AlGaIn axis, for any curve, indicating that AlN and GaIn are completely miscible at $T = 600^\circ\text{C}$.

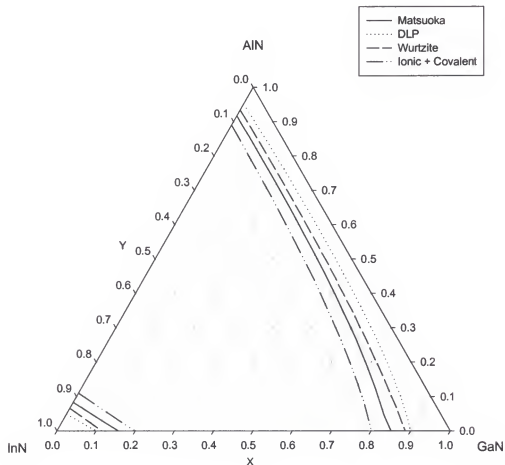


Fig. 5-11. Pseudoternary spinodal diagram at $T = 600^\circ\text{C}$ for several methods of estimating Ω .

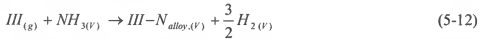
Solid-Vapor Equilibria: InGaIn

The final evaluator of thermodynamic methods to be used in this treatment is the compatibility of the model predictions of solid-vapor equilibria with experimental data

from crystal growth. Given a set of input partial pressures or flow rates of the group III species, each of these models should be able to predict the resultant solid solution for various process parameters such as pressure, temperature, and V/III ratio.

A starting point for the derivation of solid solution composition as a function of input partial pressures is that the growing film is in equilibrium at the solid-vapor interface, and therefore equilibrium constants can describe the reaction thermodynamics. Another assumption is that the diffusion rates through the boundary layer are equivalent for both group III precursor reactants.

Applying these assumptions near the boundary layer to the equilibrium reactions



where III is the group III atom in the vapor phase, leads to the equilibrium expression

$$K = \frac{a_{III-N} a_{H_2}^{3/2}}{a_{III} a_{NH_3}}, \quad (5-13)$$

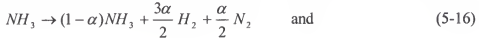
where a_k is the activity for each of the given species. Further assuming that the near-surface vapor phase is an ideal mixture of ideal gases, which is reasonable for typical VPE growth conditions, this expression becomes

$$K = \frac{a_{III-N} P_{H_2}^{3/2} P_{tot}^{1/2}}{P_{III} P_{NH_3}}. \quad (5-14)$$

The partial pressures of ammonia and hydrogen are not independent, however. At typical growth temperature, ammonia decomposes into hydrogen by the reaction



Koukitu et al. [270, 271] treated this complication by including the extent of reaction into the thermodynamic expression for K, Equation 5-14, such that



$$K = \frac{a_{III-N} ((1.5\alpha)P_{NH_3}^0)^{3/2} P_{tot}^{1/2}}{P_{III} (1-\alpha)P_{NH_3}^0}, \quad (5-17)$$

where P_i^0 is the input pressure of species i, and P_{tot} is the system pressure.

The expression for the activity of III-N in the solid solution, a_{III-N} is generated from the regular solution model. At constant temperature and pressure,

$$a_{IIIa-N} = x \exp\left\{\frac{\Omega_{IIIa-IIIb}(1-x)^2}{RT}\right\} \quad (5-18)$$

for the activity of III_aN in a binary solution $III_a III_{b_{1-x}}N$, where R is the gas constant, T is the absolute temperature, and x is the mole fraction of the given group III cation in the film.

Given this preliminary framework, the expression for x, the molar composition of the solid, can be consolidated:

$$x = \frac{P_{IIIa}^0 - P_{IIIa}}{(P_{IIIa}^0 - P_{IIIa}) + (P_{IIIb}^0 - P_{IIIb})} \quad (5-19)$$

Then, if y is the fractional distribution of the given group III cation in the vapor,

$$\begin{aligned} \frac{x}{1-x} &= \frac{P_{IIIa}^0 - a_{a-N}(1.5\alpha)^{3/2}(P_{NH_3}^0)^{3/2}P_{tot}^{1/2}/(1-\alpha)K_a P_{NH_3}}{P_{IIIb}^0 - a_{b-N}(1.5\alpha)^{3/2}(P_{NH_3}^0)^{3/2}P_{tot}^{1/2}/(1-\alpha)K_b P_{NH_3}} \\ &= \frac{y - a_{a-N}(1.5\alpha)^{3/2}(P_{NH_3}^0)^{1/2}/(1-\alpha)K_a P_{tot}^{1/2}}{(1-y) - a_{b-N}(1.5\alpha)^{3/2}(P_{NH_3}^0)^{1/2}/(1-\alpha)K_b P_{tot}^{1/2}} \end{aligned} \quad (5-20)$$

As gallium, aluminum, and boron all have low vapor pressures, the second term in the denominator is much less than $(1-y)$, and can be ignored, as $P_{III}^0 \sim P_{III}$. To simplify this expression, $P_{NH_3}^0$ and P_{tot} were also grouped with K into a new constant K' , because of the uniformity of the pressures and partial pressures across the analyzed experimental data. These parameters were maintained in the actual calculation, however. Using these simplifications,

$$\frac{x}{1-x} = \frac{y - K'_a a_{a-N}}{(1-y)} = \frac{y - K'_a x \frac{(1.5\alpha)^{3/2}}{(1-\alpha)} \exp\left\{\frac{\Omega(1-x)^2}{RT}\right\}}{(1-y)}, \quad (5-21)$$

which, upon simplification, finally becomes

$$y = x + K'_a x (1-x) \frac{(1.5\alpha)^{3/2}}{(1-\alpha)} \exp\left\{\frac{\Omega(1-x)^2}{RT}\right\}. \quad (5-22)$$

An additional simplification can exist. For the simple case where $P_{III} \ll P_{III}^0$ for both group III species, the ratio of vapor pressures between the group III elements is equivalent at the growth surface and in the far-field vapor phase, assuming diffusion to be equivalent for both species. Thus,

$$\frac{y}{1-y} = \frac{P_{IIIa}^0}{P_{IIIb}^0} \approx \frac{P_{IIIa}}{P_{IIIb}}, \quad (5-23)$$

and from Equation 5-14,

$$\frac{P_{IIIa}}{P_{IIIb}} = \frac{a_{a-N} P_{H_2}^{3/2} P_{NH_3}^{1/2} / K_a P_{NH_3}}{a_{b-N} P_{H_2}^{3/2} P_{NH_3}^{1/2} / K_b P_{NH_3}} = \frac{a_{a-N} K_b}{a_{b-N} K_a}. \quad (5-24)$$

Thus, combining this result with Equations 5-14 and 5-16,

$$\frac{y}{1-y} = \frac{K_b}{K_a} \frac{x}{1-x} \exp\left(\frac{\Omega}{RT} (1-2x)\right). \quad (5-25)$$

Note that this result requires no accommodation to the vapor pressures of hydrogen and ammonia, because the dependence for each species contributes equally in numerator and denominator of Equation 5-33. There is no difference between input and equilibrium pressures to complicate the expression.

If the vapor pressure of one or both of the group III elements is similar to the input partial pressure, the above proportionality breaks down. This case is most notable for indium nitride, as indium liquid has a vapor pressure of 10^{-5} Torr at $T = 664^{\circ}\text{C}$. Hence, the full expression for x must be used for pseudobinary solutions containing indium.

These final results from Equations 5-31 and 5-34 enable a comparison between the precursor partial pressures for the group III species and the resulting film composition. Differences may then be evaluated between the predicted interaction parameters for several models.

Figure 5-12 shows the solid-vapor equilibrium data used for the comparison of theory with experiment. Solid solutions of InGa₂N were used as a test case. Results for BGaN and BAlN solutions have been reported in the literature, but the clustering of the data due to low boron solubilities precluded a definite analysis. Individual points were not discernable in the data set; the [B,Al,Ga]₂N solution behavior could be investigated in this fashion, however.

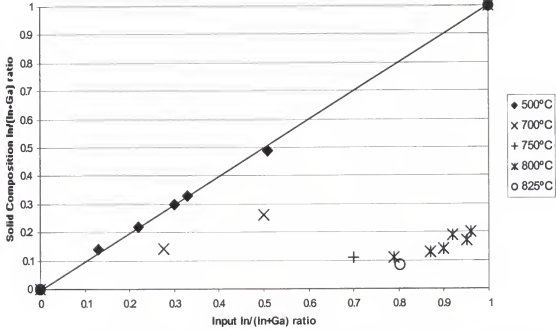


Fig. 5-12. InGa_N growth data used for statistical analysis. From references [250, 270-274].

Values for α in InGa_N solution development were taken from Matsuoka [247] and Koukitu [270-271]. The equilibrium constant K for each III-N formation reaction was computed for InN and AlN using data from Barin [240] and the JANAF tables [239], and for GaN using data from Davydov [238]. The computation was

$$\log_{10} K(T) = \sum_i^n \nu_i \log_{10} K_{f,i}(T) \quad (5-26)$$

where ν_i were the stoichiometric coefficients of Equation 5-21 and $\log_{10} K_{f,i}(T)$ are either taken straight from Barin [240] and JANAF [239] or calculated, in the case of GaN, by

$$\log_{10} K_f(T) = \frac{-\Delta G_f}{RT \ln 10} \quad (5-27)$$

With the equilibrium constant determined in this manner, the solid-vapor equilibrium distribution curves predicted by each interaction parameter could be determined. The experimental data for the solid indium content were subtracted from the applicable curves to give a statistical distribution of data. Effectively, each of these functions was treated like a sample mean of a $x = f(y,T)$, and the interaction parameters were different treatments to which an analysis of variation (ANOVA) could be applied. The underlying assumption in this type of analysis was that errors were distributed in a random fashion. From Figure 5-13, it may be seen that the distribution of errors was a skewed normal curve, but that the median of the sample data was very close to zero. This suggested that the ANOVA approach could be applied to the experimental data.

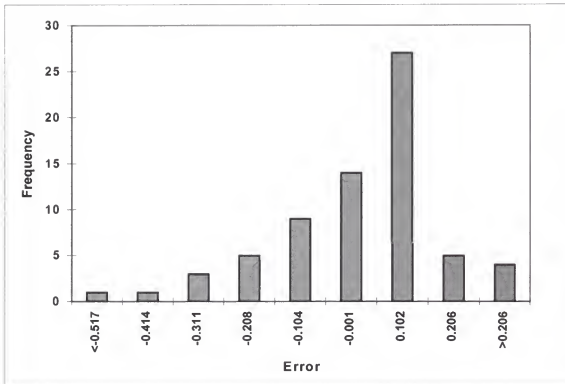


Fig. 5-13. Histogram of errors between theoretical curves and experimental data, for all treatments. X-axis bins represent upper bound of category.

Although not used in this analysis, standard deviations for the DLP interaction parameters were reported in the literature to be 240 cal/mol. The standard deviation of the ionic + covalent interaction parameter, 70 cal/mol, was estimated from the uncertainties in the heat of atomization data and the values for lattice constants for each of the binary compounds.

The results table for the analysis of variation is shown in Table 5-8. The preliminary hypothesis (H_0) was that the interaction parameters were not significantly different. Using the F-test, with over a 99% degree of certainty, the difference between theoretical and experimental data showed a statistically significant difference between interaction parameters. The other parameters for the F-test are the number of treatment degrees of freedom, and the number of data points minus the number of treatment degrees of freedom. The value of $F(0.01; 4, 80)$ was 3.6, which meant that ANOVA results higher than that indicated rejection of the hypothesis that all of the interaction parameters were statistically indistinguishable. The data and treatment for the DLP theory, which gave the worst predictions, were then removed from consideration.

The ANOVA analysis was then repeated without the DLP interaction parameter (Table 5-9). Again, to a 99% confidence interval, the interaction parameters were dissimilar [$F(0.01; 3, 64) \sim 4.1$]. Again, an interaction parameter (the wurtzite model) was eliminated.

In the resulting case (Table 5-10), which compared the Matsuoka, Ionic + Covalent, and VFF models of the interaction parameter, the F-value was 2.375. This was much less than the 99% confidence interval F-value of 4.1, and thus the hypothesis that the three interaction parameters were statistically indistinguishable was kept.

Table 5-8. Analysis of variation (ANOVA) table for comparison of InGaN interaction parameters: Matsuoka, DLP, Wurtzite, Ionic+Covalent, VFF models.

	Sum of squares	Degrees of freedom	Mean square	F
Treatment	0.6271398	4	0.156785	10.7185
Error	1.1702012	80	0.014628	
Total	1.797341	84		

Table 5-9. Analysis of variation (ANOVA) table for comparison of InGaN interaction parameters: Matsuoka, Wurtzite, Ionic+Covalent, VFF models.

	Sum of squares	Degrees of freedom	Mean square	F
Treatment	0.3423061	3	0.114102	7.417987
Error	0.9844356	64	0.015384	
Total	1.3267417	67		

Table 5-10. Analysis of variation (ANOVA) table for comparison of InGaN interaction parameters: Matsuoka, Ionic+Covalent, VFF models.

	Sum of squares	Degrees of freedom	Mean square	F
Treatment	0.0886872	2	0.044344	2.375245
Error	0.8961154	48	0.018669	
Total	.9848026	50		

Summary

Two new models of solid solution thermodynamics for wurtzite semiconductors were developed and evaluated against experimental thermodynamic data. The first model applied enthalpy of atomization data purely for wurtzite semiconductors to the regular solution model, and generated a set of binary interaction parameters using this data. Previous models combined enthalpy of atomization data from cubic-type compounds

with that of wurtzitic semiconductors to generate these interaction parameters. This work is the first to confine the thermodynamic basis of these predictions to wurtzite species.

The second model, called the “ionic + covalent model,” attempted from a primarily empirical standpoint to include a contribution from the ionic character of bonding to the alloy thermodynamics. Since current models of mixing thermodynamics are based upon cubic covalent systems, their applicability to nitride systems could thus be extended.

These two models were compared with theoretical and numerical models described in the literature. Both phase separation and solid-vapor equilibrium data were used to check the validity of each of the models. From the InGaN miscibility gap predicted from phase separation data, both the Valence Force Field model in the literature, and the ionic + covalent model are consistent with the available data. The most commonly used model, the DLP model, predicts the miscibility data the worst, followed by the model using only wurtzitic atomization data.

The solid-vapor equilibrium data was used to statistically compare the different interaction parameters. Using the difference between predicted and experimental values for the solid composition of $\text{In}_x\text{Ga}_{1-x}\text{N}$ as a function of the input vapor pressures, an analysis of variation (ANOVA) was performed. From this and subsequent analyses, both the DLP and wurtzite predictions of interaction parameters were found to not be descriptive of the experimental data. On the other hand, no statistical difference was found, with 95% confidence, between the DLP model of Matsuoka, the Ionic + Covalent model, and the Valence Force Field model. All were descriptive of the experimental data.

CHAPTER 6

GROWTH OF FREE-STANDING GALLIUM NITRIDE SUBSTRATES ON LITHIUM GALLIUM OXIDE AND LITHIUM ALUMINUM OXIDE SUBSTRATES

The ultimate purpose of this work is to explore the feasibility of using lithium gallium oxide (LGO) and lithium aluminum oxide (LAO) substrates as templates for crystal growth of thick gallium nitride films. These films could potentially be removed and subsequently used as substrates for growth of GaN-based devices.

As mentioned in the literature review (Chapter 2), LGO and LAO have significant advantages over the commonly used sapphire when used as substrates for GaN growth. The primary advantage is the close lattice match to GaN, 0.1% for LGO and 1.7% for LAO, which potentially reduces misfit dislocations between substrate and epitaxial film [111]. Other advantages are the close thermal expansion match (which reduces cracking) and solubility in acids (which provides a removal process).

The first experiments upon these substrates explored the thick film growth upon LGO substrates. This material was investigated first, because its lattice constant was most nearly identical to GaN, and previous MOCVD growths by Dr. Kryliouk suggested that GaN films grown upon LGO would possess superior structural quality compared to films grown upon LAO and especially sapphire.

Thick Films on Lithium Gallium Oxide

Thick film growth has been attempted in two different reactors (H-MOVPE and Nippon Q-MOCVD) and three different modes (HVPE, hot-wall MOCVD, MOCVD).

The following growth schemes were investigated: HVPE on (001) LGO; MOCVD, then HVPE on (001) LGO; HVPE on GaN/LGO grown in the Nippon Q-MOCVD system; MOCVD/HVPE/MOCVD on (001) LGO on (001) LGO; and MOCVD/HVPE/MOCVD on reverse-side-coated (001) LGO. All films were cleaned by the standard RCA clean, 5 minutes each of 1,1,1-trichloroethylene, acetone, and methanol, and then blown dry with house nitrogen

HVPE on LGO

The first of these processes, HVPE growth directly on nitrided, but unprotected, LGO, consisted of a growth schedule of 10 minutes of ammonia flow at the growth temperature, followed by a several-hour hydride growth. The growth temperature was 850°C, and the operating pressure was atmospheric. The NH₃ flow rate was 2 slpm, and the HCl/Ga ratio was 2:1.

This sequence, as predicted, resulted in polycrystalline, brittle film that always disintegrated upon removal from the substrate. The as-grown film was always yellow, indicative of oxygen contamination, and had very rough surface morphology, with pyramidal features typically several microns in size. These results occurred at both 850 and 950°C.

It was believed that the poor stability of the GaN film was a result of substrate decomposition upon exposure to HCl. To protect the surface of the film, and in addition to create a stable nucleation layer for thick film growth, two pathways were explored for employing an initial MOCVD layer before HVPE thick film growth. These pathways were first, using an existing MOCVD GaN film on LGO as a substrate, and secondly

growing the MOCVD layer *in situ*, then starting the thick film growth without removing the substrate.

MOCVD/HVPE on LGO

The next attempt to grow high-quality GaN thick films used a GaN/LGO heterostructure substrate created in a conventional GaN MOCVD system. The GaN/LGO substrate used was grown at 850°C and 76 Torr in the Nippon Q-MOCVD system. The thickness of the GaN film was 0.3 to 0.4 μm .

The growth schedule for this sequence consisted of 10 minutes of nitridation by ammonia flow once the substrate attained the growth temperature, followed by 2 hours of HVPE GaN growth. The HVPE flow conditions were the same as before.

The thick films grown by this method spontaneously delaminated from the LGO substrates, and generally—but not always—fragmented into several pieces of variable size, when removed from the substrate. Each film was 200 to 300 μm in thickness and laterally uniform, and was an opaque canary yellow in color. None of the as-grown films were transparent. The growth surface of the films was uniformly rough and three-dimensional, consisting of pyramidal hillocks over the entire surface.

X-ray diffraction (XRD) of the film proved the epilayer to be monocrystalline (Fig. 6-1). After a minute of sputtering to remove surface contaminants, AES of the free-standing film near the surface showed that the epilayer was heavily contaminated with oxygen, with the same oxygen concentrations at the substrate/layer and free surfaces.

This sequence was attempted only three times, due to a scarcity of GaN/LGO substrates.

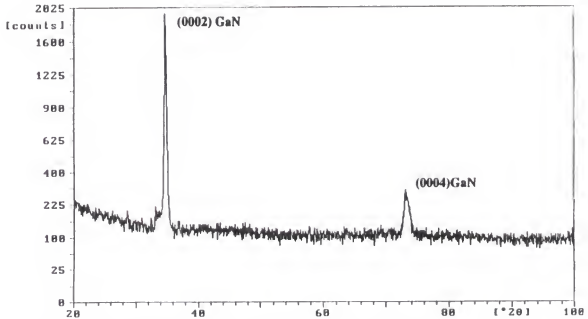


Fig. 6-1. Low-resolution XRD of HVPE film on MOCVD GaN/LGO substrate.

In Situ MOCVD/HVPE on LGO

The next sequence investigated involved hot-walled MOCVD growth upon a nitrided LGO film, followed by a thick hydride growth of several hours in the same reactor. It was believed that a protective layer of MOCVD-grown GaN would both create a high-quality nucleation layer for subsequent thick film growth and better protect the substrate from HCl attack. Performing both MOCVD and HVPE growth steps *in situ* would eliminate thermal cycling of the MOCVD layer, which was a potential source of microcracks.

The substrate was nitrided in 500 sccm of ammonia for ten minutes, followed by an MOCVD GaN step of 15 or 30 minutes, and completed by a several-hour hydride step. The growth temperature was 850°C, and the operating pressure was atmospheric. The HVPE flow conditions were the same as before.

From a qualitative standpoint, all of the films grown *in situ* were structurally similar to the film grown *ex situ* using the second technique. Handling of the free-standing film generally resulted in fragmentation, even when great care was used.

X-ray diffraction showed single-crystalline film with a FWHM of 46.7 for an ω -scan of the (0002) GaN peak (Fig. 6-2). Auger Electron Spectroscopy showed a very high (~10%) concentration of oxygen in the film, quite similar to the previous method (Fig. 6-3).

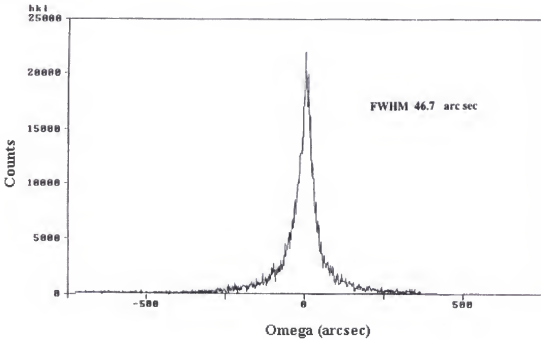
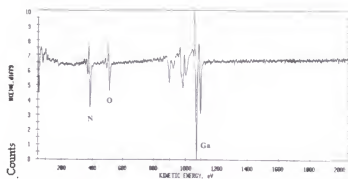


Fig. 6-2. HR-XRD spectrum of an in situ MOCVD/HVPE GaN/LGO film.



GaN film as grown (top)

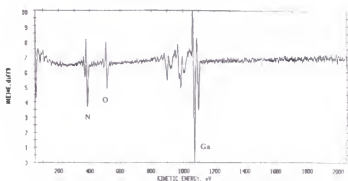
GaN / LiGaO₂ interface

Fig. 6-3. AES spectra of an in situ MOCVD/HVPE GaN/LGO film.

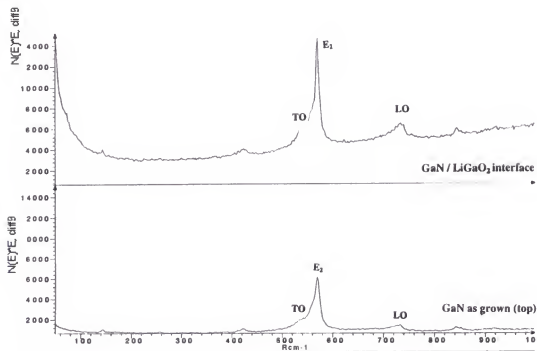


Fig. 6-4. Raman spectra of MOCVD/HVPE GaN/LGO film.

Raman spectroscopy indicated a film of high quality, as shown in Figure 6-4. Identifiable in this figure are the TO, E2, and LO phonons at 545, 569, and 735 cm^{-1} , respectively. Of particular interest is the lack of shifting of the E2 peak from interface to free surface. This indicates that very little stress is present in the film. Furthermore, the FWHM of the E2 peak is narrow, indicative of film with high structural quality.

Atomic force microscopy on these samples showed a highly uniform surface, with a surface roughness of 0.3 nm. This sequence was supplanted by the nitridation/MOCVD/HVPE/MOCVD technique, in an attempt to improve the surface morphology of the film.

MOCVD/HVPE/MOCVD on LGO

Another attempt to grow free-standing film used MOCVD as a final “capping” step to improve the surface morphology of the previous method. This sequence was the same as the nitridation/MOCVD/HVPE step, but a final MOCVD step of 15 or 30 minutes was added. The growth conditions were the same as the previous techniques.

Qualitative, films grown with this technique resembled films grown by the MOCVD/HVPE techniques, but the growth surfaces were much smoother, and the thickness across the wafer was more uniform. No pyramidal features were noticeable with the naked eye, although pyramidal mesas did appear under observation with SEM.

This improvement in surface morphology was quantified by AFM. RMS roughness decreased from 0.3 to 0.03 nm. While this roughness figure is still not suitable for use as a substrate, it represents a significant improvement upon the previous

technique. Figure 6-5 shows the best film produced with this sequence, obtained by the sacrificial etch of the GaN/LGO wafer with aqueous HCl.

X-ray diffraction of these thick films confirmed their high structural quality. The best films showed a FWHM of ~50 arc-seconds, approximately twice the theoretical minimum for gallium nitride. Typical films showed FWHM of 100 to 300 arc-seconds. AES analyses of the films were similar to those of the nitridation/MOCVD/HVPE sequence, showing high levels of oxygen incorporation.

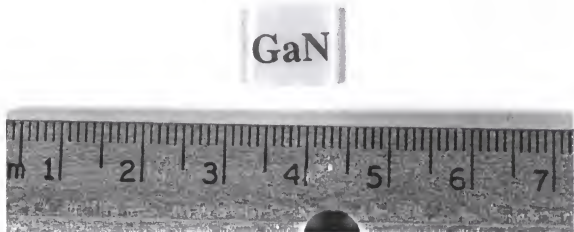


Fig. 6-5. Free-standing GaN crystal produced by the MOCVD/HVPE/MOCVD schedule.

Secondary ion mass spectroscopy (SIMS) was used to identify trends in impurity incorporation for this method. SIMS depth profiles were acquired in a Perkin-Elmer PHI

6600 SIMS system using a 5 keV Cs^+ primary ion beam and negative secondary acquisition. Emission currents of 202 and 103 nA were used, and raster sizes of between 250 and 350 μm square were used. Sputtering proceeded from the GaN/LGO interface, and all surveys showed the initial discontinuity from sputtering the rough surface.

The SIMS analysis showed detectable amounts of carbon, chlorine, lithium, and oxygen. Depth profiles of MOCVD and MOCVD/HVPE/MOCVD films using identical sputtering parameters are shown in Figures 6-6 and 6-7. Since GaN standards were not available for quantification of carbon, chlorine, lithium, or oxygen concentrations, the impurity intensities were scaled to that of gallium-87, which was very nearly constant throughout the GaN matrix.

Each of the contaminants had multiple possible sources. Lithium was principally present in the LGO substrate, but could also have been present as a trace contaminant in either the “blue” (99.999% purity, plus Na for oxygen removal) ammonia or the trimethylgallium. Carbon was predominantly from the trimethylgallium and its decomposition products, but could have also been from Viton O-ring seals. Oxygen was a component of the substrate, but could also be found in the quartz walls. At high temperatures, quartz will react with HCl to form volatile silicon chlorides and oxygen or SiO , so this reaction was known to be present, although not to a significant degree based upon the oxygen contamination of GaN grown upon sapphire substrates.

Chlorine may have been adsorbed on the reactor walls or inlet lines, but the majority of the chlorine in the reactor was present downstream in the form of ammonium chloride (NH_4Cl), which was a byproduct of the hydride reaction. Excess ammonia and HCl from the GaN HVPE formation reaction (Equation 3-5) react, then condense in low-

temperature locations in the reactor. Regular reactor cleaning was performed to minimize this effect, but NH_4Cl was an omnipresent reaction product, and continual reactor cleaning (i.e. after each run) was impractical due to the reactor size and downtime for bakeout. As a result, since heroic measures would have been necessary to proscribe the presence of chlorine, its presence was tolerated. The relatively high concentration of chlorine in Figure 6-6 may reflect this fact.

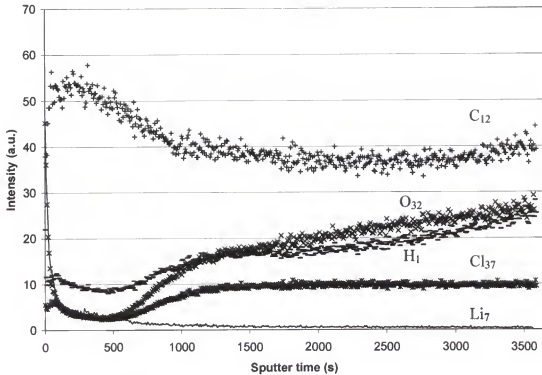


Fig. 6-6. SIMS depth profile of free-standing MOCVD GaN grown on LGO. Profile shows interface ($t = 0$ s) transition to bulk.

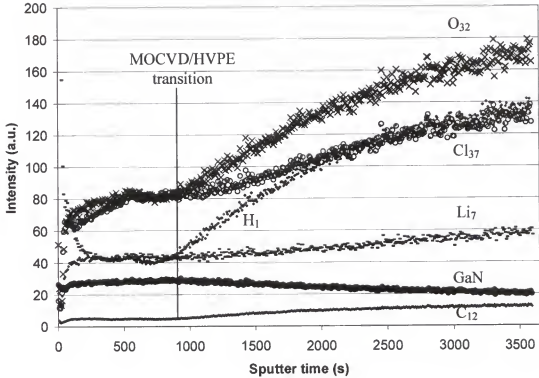


Fig. 6-7. SIMS depth profile of MOCVD/HVPE/MOCVD film showing transition of interface to MOCVD nucleation/protection layer to HVPE thick film.

Several trends were apparent from Figure 6-7. The first was the presence of high concentrations of lithium near the interface, when compared to the bulk. However, this feature may be surface contamination, due to the ubiquitous nature of Li as a contaminant. The second attribute of this profile was nearly constant amounts of carbon, oxygen, lithium, and chlorine in the protective MOCVD film. The final characteristic of this profile was the rise in carbon, oxygen, lithium, and chlorine at a sputter time of $t = 900$ s. From the etch rate at this amperage ($\sim 12 \text{ \AA/s}$), this transition began $\sim 1 \text{ }\mu\text{m}$ from the interface. This was consistent with the thickness of an MOCVD growth of 15-minute duration. Thus, it was reasonable that this discontinuity is due to the start of HVPE

growth. The increase in chlorine concentration reflected the increase of chlorine in the gas phase (although the transition in the film occurred more gradually than the rapid change in the gas phase composition).

After the HVPE growth begins, the amount of lithium and oxygen in the film increased, and the amount of GaN (scaled to gallium) decreased. The only interpretation of the latter fact was a significant (percent, not ppm) decrease in nitrogen fraction on the group-V sublattice. Any change in the gallium sublattice would cancel with the gallium nitride signal, as the intensity of the two signals would move in tandem in the raw data. In light of this fact, since carbon and lithium generally inhabit group-III sites, and oxygen inhabits group-V sites, the concentration of oxygen in the HVPE film was very high.

This last conclusion, taken in tandem with the increased amount of lithium in the film, was highly suggestive that the LGO substrate decomposed upon exposure to HCl. It is possible that the MOCVD layer was discontinuous; for instance, the sides and reverse of the substrate were likely not completely covered. Exposure to HCl may have caused LGO decomposition on the sidewalls and reverse of the substrate. Although SIMS was not performed upon MOCVD/HVPE films, it was conjectured that this decomposition mechanism was also responsible for the high amounts of oxygen detected by AES.

Reverse Side MOCVD Coatings

The most promising sequence for the production of gallium nitride thick films on LGO substrates relied upon a protective reverse side coating to prevent HCl attack. The reverse side of the LGO wafer was nitrided, then coated with a 1 to 2 μm film of GaN, deposited by MOCVD at 900°C. The substrate was turned over, and the bare surface was grown upon using the nitridation/MOCVD/HVPE schedule at a growth temperature of

900°C. All other growth conditions were the same as conducted previously. As this procedure was very time-intensive, requiring two days of reactor scheduling time, it was attempted but once.

Immediately upon removal from the reactor, two differences between the two-sided and MOCVD/HVPE/MOCVD films were immediately apparent. First, the film was not yellow and opaque, but rather was colorless and transparent, suggestive of less oxygen contamination than the previous films. Also, a circular region in the center of the film was mirror-smooth, which never occurred for thick films grown by other techniques. Previously, films of $<15\text{ }\mu\text{m}$ were occasionally mirror-smooth, but thin film substrates were nearly impossible to manipulate.

Unfortunately, the thick film demonstrated very broad cracks visible to the naked eye, possibly due to thermal strain from temperature cycling. Cracking was anisotropic, and the cracks generally ran parallel to each other in the (100) direction. Under inspection by SEM, the flakes that this cracking produced were cohesive, mirror-smooth and showed few microcracks.

Proceeding under the assumption that XRD would not yield useful information due to the ubiquitous cracking of the film which would create either broad (002) GaN peaks or several near-(0002) peaks, the composition and surface morphology were investigated by SIMS and AFM. The oxygen and carbon composition, and perhaps the associated yellow luminescence, would determine whether this technique met the objective of minimizing substrate decomposition during growth.

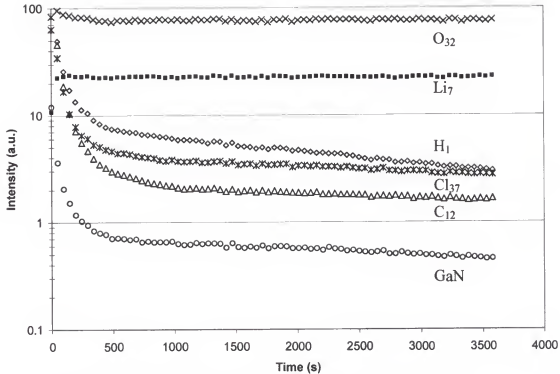


Fig. 6-8. SIMS depth profile of reverse-side-coated GaN/LGO thick film.

Since SIMS performed upon the reverse-side-coated film was confined to a region between cracks, the film can be compared to films grown by the other methods because the GaN matrix was the same. Figure 6-8 shows the composition of the film from the top surface into the bulk of the film. Most notable in this figure are the oxygen and carbon concentrations. When compared to the MOCVD GaN/LGO reference from the H-MOVPE reactor, this film has much less carbon. More importantly, the reverse-side-coated film has only 37% of the oxygen concentration of the MOCVD/HVPE/MOCVD sample, which indicates that the concept of protecting the reverse side from HCl exposure aids in lowering the oxygen content.

Figure 6-9 shows the resultant photoluminescence spectrum of the top side of the reverse-side-coated GaN/LGO thick film. The signal was not intense, especially when

compared to spectra from GaN/sapphire, but four peaks stand out. Two, the emission peak at 350 nm and its second-order peak at 700, were attributable to the 350 nm source. The broad peak at 420 nm was likely due to imperfect screening of the fluorescent room lighting, but may also be due to the as-yet-unidentified peak present in several of the GaN/sapphire optimization films. The wide peak at 500 nm was, however, sample-related, and was the “yellow luminescence” commonly found in GaN films. Interestingly enough, no band-edge peak at ~ 370 nm was present; it was hidden by the intensity of the yellow luminescence.

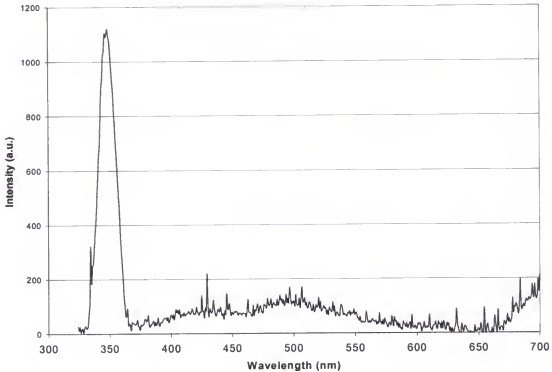


Fig. 6-9. Photoluminescence spectrum of GaN film upon reverse-side-coated LGO.

Although the film was mirror-smooth from a macroscopic viewpoint, the surface was surprisingly rough when measured by AFM. Figure 6-10 shows one of the pair of scans used to calculate the surface roughness of the film. While the average root-mean-

square roughness of 8.7 nm is much less than gallium nitride films grown on sapphire under these conditions (see Chapter 3), this value is greater than the roughness of the MOCVD/HVPE and MOCVD/HVPE/MOCVD films by almost three orders of magnitude.

This is the only technique to date that has generated colorless, mirror-smooth GaN film on LGO substrates, qualities which are both desirable for use as substrates. The lack of yellow color in this film suggested a low oxygen content, which was confirmed by SIMS. Unfortunately, cracking and flaking of the epitaxial film due to LGO substrate growth defects (twins, dislocations) has prevented this technique from producing free-standing large substrates.

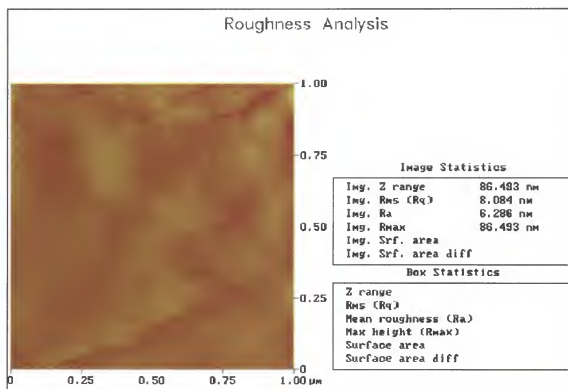


Fig. 6-10. Atomic force microscopy roughness analysis of top side of reverse-side-coated GaN/LGO thick film.

Summary of LGO Results

While films grown upon LGO substrates were highly crystalline, smooth, and uniform, no transparent thick films could be grown without extremely high oxygen concentrations from substrate decomposition. Films were never mirror-smooth. Often, the thick films peeled or crumbled under the amount of force necessary to lift them from the wafer holder to the sample box. The thicker (300 to 400 μm) MOCVD/HVPE and MOCVD/HVPE/MOCVD films generally stayed intact during characterization, however, which is categorized as “fair” in the summary table below.

While high conductivity resulting from the high oxygen doping could be beneficial toward forming ohmic contacts, the same doping could be deleterious to efficiencies of photonic devices, should oxygen be the underlying cause for yellow luminescence in gallium nitride. This, combined with the brittleness of these films, suggested that LAO was a more promising substrate. Despite the higher lattice mismatch, the chemical stability of LAO recommended it as an alternative.

Table 6-1. Summary of LGO Results.

	HVPE	MOCVD HVPE (<i>ex-situ</i>)	MOCVD HVPE (<i>in-situ</i>)	MOCVD HVPE MOCVD	Reverse side coated (top side)
Color	yellow	yellow	yellow	yellow	clear
Transparency	opaque	opaque	opaque	opaque	transparent
Mechanical Stability	poor	fair	fair	fair	fair
XRD FWHM (arcsec)	—	single crystal	46.7 (best)	~50 (best) 100 to 300 ave.	—
Roughness (nm)	—	—	0.3	0.03	8.754
Contaminants [SIMS, scaled to MOCVD GaN/LGO]	—	C, O, Cl [AES]	C, O, Cl [AES]	C: 17% O: 730% Cl: 910%	C: 2% O: 270% Cl: 28%
Notes	fragmented				cracking

Thick Films on Lithium Aluminum Oxide

Once the use of LGO was found to be inadequate for the production of GaN substrates, attention was turned to lithium aluminate (LAO). Although LAO possesses a greater lattice and thermal expansion mismatch to gallium nitride than LGO (-1.7% vs. 0.1% and 27% vs. 7%) [111], lithium aluminate is more chemically stable than LGO. From a practical consideration, this means that HCl and H₂ do not decompose the substrate. Hydrogen may be used as a carrier gas, both to getter any oxygen in the system, and to promote the decomposition of NH₃ to provide reactive nitrogen at the wafer surface.

The plan of research for thick film growth upon LAO films was to investigate the effect of carrier gas, with the goal of using hydrogen or a hydrogen/nitrogen mixture to improve the film quality. From that initial stage, variation of the growth methods would take place to determine if an initial MOCVD layer was necessary, and the optimal layer thickness for high-quality thick GaN film growth.

Carrier Gas Investigations

A series of experiments was performed to test the stability of LAO, and also to observe the effect of using hydrogen-containing carrier gases upon the oxygen content of the gallium nitride film.

Films were grown at 900°C in a nitrogen carrier gas under both MOCVD and HVPE conditions. The MOCVD films were generally uniform, transparent, and mirror-smooth, but possessed a yellowish tint indicative of oxygen contamination in the films.

The HVPE films grown produced an even more intense yellow (perhaps due to the greater thickness), and possessed a rough but uniform surface.

With the idea that reducing atmospheres could significantly lessen this oxygen contamination, attention was turned toward changing the carrier gas from N_2 to H_2 for the gallium nitride growth. Although it was surmised that LAO was chemically more stable than LGO, the extent of this stability was unknown, especially in high temperature reducing atmospheres. To investigate this topic, test pieces of each substrate were exposed to pure hydrogen at 900°C . Even from visual observation, the LGO appeared markedly different from its as-received form, while the LAO was substantially the same. The LGO wafer turned a deep gray, and the surface appeared very rough. The LAO showed very slight discoloration, but the previously-polished surface retained its mirror-smoothness. When exposed to HCl in nitrogen at 900°C , the LGO similarly showed surface degradation, while the LAO appeared generally unchanged.

This stability suggested that hydrogen, or at least a hydrogen mixture, could be used as a carrier gas for LAO substrates. The obvious benefit of this would be that hydrogen would scavenge any free oxygen in the system, improving the quality of the gallium nitride film. This process would be impossible with LGO, because the substrate would decompose.

First, hydrogen was chosen as a carrier gas. Hydride vapor phase epitaxy on LAO substrates at 900°C produced transparent, mirror-smooth, colorless gallium nitride films. When MOCVD was attempted using hydrogen, however, premature decomposition of the trimethylgallium occurred in the inlet of the reactor, and GaN films grew unpredictably, slowly, and unevenly when they grew at all. This was due to the lower decomposition

temperature for TMG in hydrogen as opposed to nitrogen. Unfortunately, this problem could not be overcome with the hot-wall reactor design.

Next, a 4% H_2 /96% N_2 gas mixture was tried. Again, the HVPE of thick GaN films on the LAO substrate produced transparent, mirror-smooth, colorless films. In contrast to MOCVD attempts using nitrogen or pure hydrogen, films grown using the 4% mixture were consistently uniform, mirror-smooth, colorless, and transparent. Hence, a 4% H_2 /96% N_2 mixture was optimal for MOCVD growth, while either the mixture or pure hydrogen could be used for HVPE growth.

Growth Sequences

With the issue of carrier gas investigated, attention was turned toward investigating the optimal growth process for producing free-standing gallium nitride substrates using LAO templates. The primary goals for this battery of experiments was the investigation of the effects upon crystal quality and surface morphology of different growth techniques, and the reduction of oxygen contamination in the free-standing GaN films when compared to free-standing GaN films grown upon LGO.

The possibilities being investigated were: HVPE on nitrided LAO; MOCVD then HVPE on nitrided LAO (MOCVD/HVPE); and MOCVD then HVPE then a final, capping layer of MOCVD-grown GaN (MOCVD/HVPE/MOCVD) on nitrided LAO. The duration of the initial MOCVD step was kept constant at 30 minutes, while the HVPE step was 120 minutes for all films. The final MOCVD step was 15 minutes long, which was the same duration as the best-morphology results for LGO. For the nitridation and MOCVD steps, the carrier gas would be the 4% H_2 mixture, and for the HVPE steps, the carrier gas would be hydrogen. All film growths would take place at 900°C.

After completion of the growth steps, NH_3 was flowed for 10 minutes in a nitrogen carrier gas to prevent surface degradation from any residual hydrogen, while the hydrogen was displaced as the carrier gas. The wafer cooling was generally paused at 800°C for 45 minutes to anneal the film, and then it was permitted to continue to room temperature over a period of 8 hours.

Using this procedure, films grown by HVPE, MOCVD/HVPE, and MOCVD/HVPE/MOCVD were generally mirror-smooth, transparent, and colorless. The lack of color suggestive of negligible oxygen contamination indicates that LAO is more promising than LGO for the production of free-standing gallium nitride films.

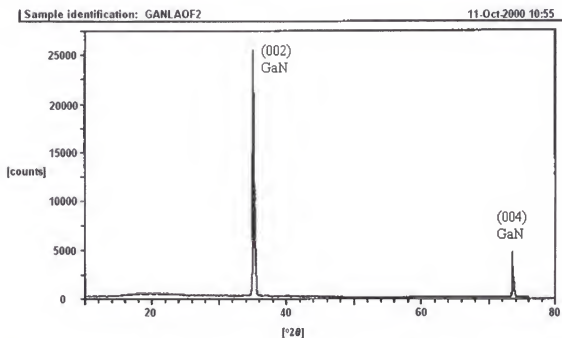


Fig. 6-11. Low-resolution XRD spectrum of free-standing MOCVD/HVPE GaN grown upon LAO substrate.

Low-resolution 2θ XRD scans performed on these films indicated that all schedules produced gallium nitride that was single-crystalline and of high structural

quality (Fig. 6-11). High-resolution XRD showed that, despite this high quality, significant mosaic spread existed in the ω -scan of these free-standing films. The FWHM of these films was lowest for the MOCVD/HVPE growth schedule, at ~ 2200 arc-seconds. The crystallinity of the film capped by the 15-minute MOCVD layer was very similar, while the film grown by HVPE without any MOCVD intermediate layer exhibited the worst crystallinity with over an arc-degree of spread.

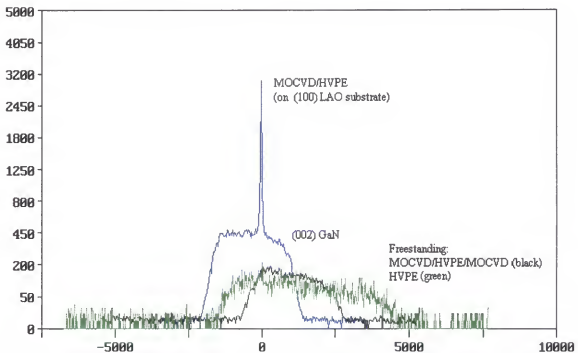


Fig. 6-12. High-resolution XRD spectra of different growth schedules for free-standing GaN films grown upon LAO substrates.

These crystallinity results indicated that providing a high-quality nucleation layer such as an MOCVD layer before the subsequent HVPE growth would result in improved crystallinity throughout the film. Furthermore, it was apparent that simply nitriding the LAO surface through exposure to ammonia was insufficient for the production of a satisfactory nucleation layer.

Although the crystallinity of films grown by the MOCVD/HVPE schedule was poorer than substrates grown by high-pressure techniques [109], it compared well with the literature reports of free-standing gallium nitride films grown by sublimation sandwich or HVPE [108, 170]. These XRD results still compare unfavorably with the crystallinity of the thick films grown upon LGO substrates, which generally had FWHMs of a few hundred arc-seconds.

The surface morphology produced by the three techniques was in all cases similar, consisting of a uniform surface that was faceted. Because of the faceting, AFM results varied widely among the several techniques. This was due to the tendency for the AFM tip to image either the crown of the pyramidal facet, or the valley between facets. Scans were performed twice on different areas of the film, and the rms roughness averaged between the two scans. The slopes of the facet yielded a rms roughness of ~ 3 to 4 nm for a $1\ \mu\text{m} \times 1\ \mu\text{m}$ area, and a rms roughness on the order of 20 nm for a $5\ \mu\text{m} \times 5\ \mu\text{m}$ area, when $5\ \mu\text{m} \times 5\ \mu\text{m}$ could be imaged at all. While these roughnesses are an order of magnitude higher than free-standing gallium nitride films grown upon LGO substrates, they are quite similar to roughnesses of GaN films grown upon sapphire substrates at 900°C , indicating that no surface morphology benefit accrues to the use of LAO as a template. A typical AFM plot, for the HVPE-grown film, is shown in Figure 6-13.

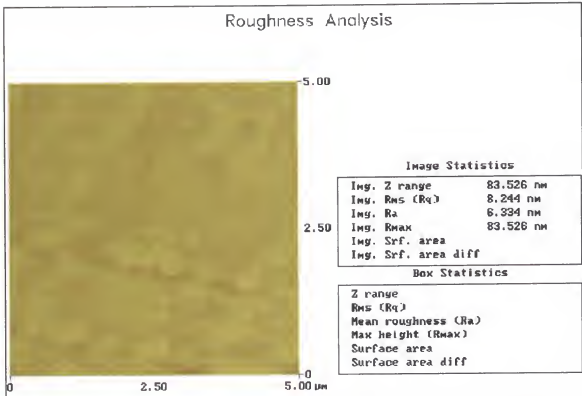


Fig. 6-13. Surface roughness of free-standing HVPE GaN grown upon nitrided LAO. Figure shows a 5 μm x 5 μm area.

In similar fashion to the LGO growths, SIMS analysis was performed upon the free-standing GaN films grown upon LAO. The dividing line shown in Figure 6-14 again denoted the transition from MOCVD to HVPE growth methods. From this figure, several results are apparent. First, insignificant amounts of lithium were detected in the film, in the mass survey. When compared to the appreciable amount of lithium detectable in the films grown upon LGO, this result further suggested that LAO was a much more stable GaN substrate than LGO.

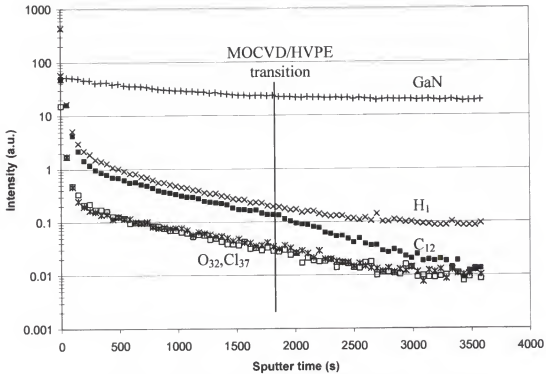


Fig. 6-14. SIMS depth profile of free-standing MOCVD/HVPE GaN grown on LAO. Profile shows interface transition ($t = 0$ s) to MOCVD nucleation/protection layer to HVPE thick film.

Another trend revealed by the SIMS data provided information upon the difference between HVPE and MOCVD growth chemistries. The thick films grown on LGO by the MOCVD/HVPE technique showed a significant increase in chlorine, carbon, and especially oxygen as soon as the HVPE technique started. By contrast, the films grown upon LAO continued the same monotonic decrease in oxygen and chlorine from the MOCVD segment of the growth. The incorporation of carbon fell off even more rapidly with the onset of HVPE growth.

These findings were interpreted to provide evidence of LGO substrate decomposition upon the initiation of HVPE growth, as the preeminent lithium source in the growth system was the LGO substrate. Lithium was not found in the GaN/LAO free-

standing film, the O_{32}/Ga signal ratio did not increase when the HVPE segment of the growth began, and the GaN/Ga signal was constant, all of which supported the contention that the LAO substrate did not decompose.

An alternate explanation for this data would be for the Li and O to form more stable gas-phase species in a 4% H_2/N_2 mixture, while the LAO decomposes. For instance, H_2O could be formed which is stable and has a high vapor pressure. However, under these conditions the most stable Li-containing species in the gas phase, according to modeling with ThermoCalc (which primarily uses JANAF [239] and Barin [240]), is $LiCl$. Because Li would incorporate from $LiCl$ into the GaN film and would thus be detectable by SIMS, this explanation is unsupported by fact.

The decrease in carbon concentration warrants more interest. Using 100% N_2 with LGO caused the carbon content to rise upon the start of HVPE growth; using 4% H_2/N_2 with LAO caused the carbon content to fall. Two possible explanations exist for this trend. First, the presence of Li, O, or Cl could cause carbon to contaminate the film more readily. Unfortunately, studies of the incorporation kinetics and mechanisms of impurities have not yet progressed to this complexity. In principle, ESCA could be used to distinguish differences in bonding character, for instance between C-N and C-O, but the task would be beyond the scope of this work, and could be studied in the future.

Alternately, the presence of H_2 , in addition to gettering any O present, may reduce the amount of carbon in the film, possibly by facilitating the production of methane (CH_4) from the CH_3 groups attached to the Ga in trimethylgallium. In this manner, the carbon would be in its most thermodynamically stable form (for this pressure and temperature). In a pure nitrogen environment, TMG decomposes at higher temperatures,

and by the adduct formation mechanism (Reactions 3-4 to 3-7) with lower methane selectivity. With higher concentrations of less stable C-containing compounds, more C would be incorporated with 100% N₂ carrier gas than with using 4% H₂/N₂.

The most natural method to distinguish between the two possibilities is to expand the set of experiments to include 100% N₂ as the carrier gas for an LAO experiment, and to measure the concentrations by SIMS. Using 4% H₂/N₂ would not be a meaningful experiment because LGO decomposes even with this small concentration of hydrogen. Since this would release Li- and O-containing species upon initiation of the HVPE step, the experiment would not differentiate between the explanations for the change in carbon incorporation trends.

Finally, the most significant result from the SIMS data was the reduction of impurity concentrations from films grown upon LGO, by using LAO and 4% H₂/N₂. Lithium was undetectable in the MOCVD/HVPE film grown on LAO. Oxygen, chlorine, and carbon all had greatly lowered concentrations compared to film grown on LGO, and were comparable to GaN films grown upon sapphire. Table 6-2 shows the full magnitude of the reduction, for identical SIMS sputter conditions:

Table 6-2. Impurity concentrations for various isotopes, from SIMS. Values are intensity, scaled to gallium intensity. Results for the optimization baseline GaN/sapphire HVPE film are provided as a reference point. "+" indicates minimum value for a concentration that continued to rise throughout the HVPE portion of the scan.

Isotope	LGO MOCVD	LGO MOCVD/HVPE	LAO MOCVD/HVPE	Sapphire HVPE
O ₃₂	27+	170+	<0.01	<0.01
Cl ₃₇	10	130+	<0.01	<0.01
C ₁₂	40	13+	<0.01	<0.01
Li ₇	~1	60+	n. d.	n. d.

Initial MOCVD Times

The growth duration for the initial MOCVD layer was varied to determine the effect upon the crystallinity and stress of the hydride film. The films were grown with MOCVD durations of 0, 5, 15, and 30 minutes, and the films were analyzed by XRD and Raman spectroscopy. All films demonstrated single-crystal character, but for the 5-minute film. It is unknown why the resultant film was polycrystalline. High-resolution XRD was not attempted upon the 5-minute growth, for this reason. The 15-minute growth was later set aside for subsequent device growth, due to its crystallinity and superior surface morphology. Performing HR-XRD generally contaminated film surfaces with organic residue from the tape or oil used to mount the sample, and thus HR-XRD was postponed for this sample, as well.

Because compressive stress in gallium nitride films affects the wavelength of the Raman E2 exciton and its replicates, the location of these peaks may be used to determine the amount of stress in a film [194, 275, 276]. Toward this end, Raman spectroscopy was used to investigate the variation of stress with the duration, and therefore thickness, of the initial MOCVD layer. Samples were analyzed on a Jobin-Youn 1000 Raman system using the 488 nm line of a 100 mW argon ion laser in Stokes mode. The system was calibrated using the spectrum of (111) Si for a standard. The depth of focus used was 30 μm , and the beam was focused slightly above the top surface of the film, to further confine the analysis to the surface.

The spectra shown in Figure 6-15 demonstrated that the effect was small between the samples, but large when compared to the nearly lattice-matched LGO spectra from

Figure 6-4. Because the Raman system was set up in Stokes mode, the E2 shift due to compressive stress will decrease the wavenumber of stressed films. The stress-sensitive E2 line was, to a first approximation, the same for each sample, at 562 cm^{-1} , but was significantly shifted from the 569 cm^{-1} E2 line of free-standing GaN grown upon LGO substrates. This indicated that, while the GaN/LAO films were nearly lattice-matched (though not as well as LGO), residual stress was both apparent and measurable. The TO phonon appeared most prominent in the samples which had the longest MOCVD initial layers, which suggested higher quality than the HVPE or 5-minute initial MOCVD layered samples.

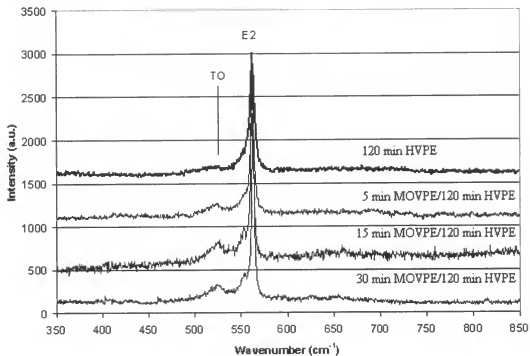


Fig. 6-15. Raman spectra of free-standing GaN films grown upon LAO substrates with different initial MOCVD growth times.

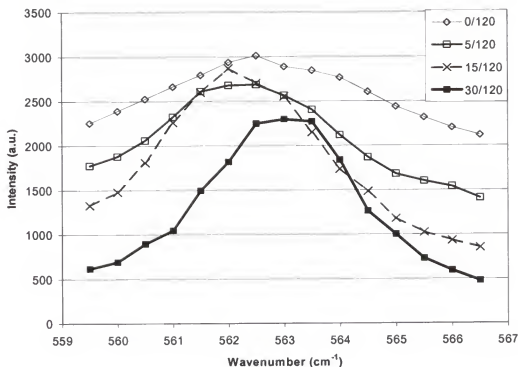


Fig. 6-16. Magnified view of E2 peak from Fig. 6-15 showing peak shift.

The fine detail of the E2 peak was further examined to confirm the lack of a stress-related shift between the LAO samples, and to investigate the behavior of the stress. Figure 6-16 demonstrated that each of the spectra above had its peak at 562 cm^{-1} with the exception of the 30-minute MOCVD initial layer. This film peaked at 563 cm^{-1} , which meant that the film was less stressed than each of the other films, although the difference was relatively small. This scan was repeated, and the difference confirmed.

Another investigation of the stress inherent in the films was undertaken by scanning the top and bottom surfaces of the free-standing 30-minute MOCVD/HVPE film. The top of the film was analyzed with an increment of 0.1 cm^{-1} , to increase the precision from the 0.5 cm^{-1} increment of the previous scans, and with a longer detection time to dampen any random fluctuations. The free-standing film was flipped, and the

measurement was performed on the interface side of the film, then flipped again to remeasure the Raman spectrum of the top of the film. Figure 6-17 presents the results.

From the figure, the Raman shift for the 30/120 MOCVD/HVPE schedule does not appear to be as great as in Figure 6-16. This is likely due to the increased resolution around the 562 and 562.5 cm^{-1} points. The slope of the 30/120 curve in Figure 6-16 is a skewed bell curve, unlike the others, and is shallower on the left than on the right, which suggests the possibility that resolution is an issue. The peak shift is still present in Figure 6-17, however, indicating that the top surface is less stressed than the GaN/LAO interfacial surface.

From this conclusion, the stress for the 30/120 film must have been relieved in one of two ways, as the film grew: either elastically by biaxial strain, which should show up as an asymmetric (0002) GaN peak under high-resolution XRD; or inelastically, through the formation of dislocations. From the symmetry of the HR-XRD ω -scan, the conjecture made (pending TEM observation, for instance) was that the 30/120 film is less stressed due to dislocation formation. Consequently, at least the free-standing GaN films grown upon LAO with a 30-minute MOCVD initial step are hypothesized to possess a higher dislocation density than free-standing GaN films grown upon LGO, which showed no peak shift. No such conclusion can be made for films grown upon LAO with shorter initial MOCVD times, because no evidence of a peak shift was present in the Raman spectra between the free surface and the interface surface.

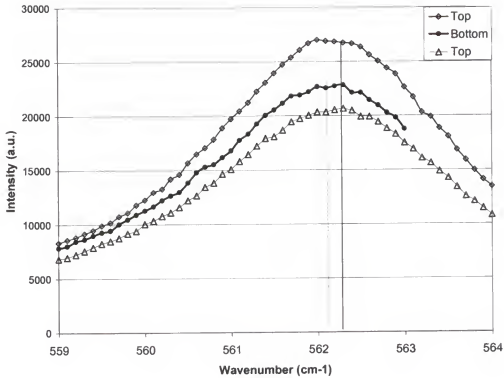


Fig. 6-17. Increased-resolution Raman scan of both sides of 30-minute MOCVD/120-minute HVPE film.

Summary of LAO Results

Lithium aluminum oxide was investigated as a template for growth of free-standing GaN substrates. Although LAO was known to possess a poorer lattice match to GaN than LGO, its chemical and thermal stability recommended it as an alternative to LGO, which decomposed during HVPE growth. Unlike LGO, LAO was found to be stable even in the most reactive chemical environments of H_2 and HCl .

Several 35 to 40 μm single-crystalline films were grown at 900°C using various growth schedules, in a fashion similar to the LGO study. All of the studied growth schedules—HVPE, MOCVD/HVPE, and MOCVD/HVPE/MOCVD—produced free-standing single-crystalline films. The films with the MOCVD initial layer had

significantly better crystal quality as measured by high-resolution XRD. Atomic force microscopy (AFM) results demonstrated surface roughnesses comparable to films grown on sapphire at this temperature. The chemical composition of the GaN films grown upon LAO was greatly improved upon the LGO films, for the MOCVD/HVPE schedule. Orders of magnitude less oxygen, carbon, and chlorine were present in the LAO films, demonstrating that the arrangement of the more stable LAO substrate and the inclusion of hydrogen in the carrier gas combined to reduce contamination of impurities in the resulting film.

Stress was also measured by Raman spectroscopy, for several films grown with various initial MOCVD layer thicknesses. It was found that all films were significantly stressed in comparison to the unstressed films grown upon LGO, and that the film with the thickest MOCVD layer was slightly less stressed than the rest.

Finally, the GaN/LAO films, although only $\sim 40\ \mu\text{m}$ thick, remained intact through the manipulation during characterization, which was not possible for films of this thickness grown upon LGO templates. In the summary table below, this mechanical stability is referred to as “good.”

Table 6-3. Summary of LAO results. Abbreviations: H = HVPE, M = MOCVD

Sequence	H	M/H	M/H	M/H	M/H/M
Time (min)	120	5/120	15/120	30/120	30/120/15
Color	clear	milky	milky	milky	milky
Transparency	semi	semi	semi	semi	semi
Mechanical stability	good	good	good	good	good
XRD FWHM (sec)	3600+	--	--	2200	2400
Roughness (nm)	2.79 (1 μm) 14.1 (5 μm)	18.16	1.68 (1 μm) 49.5 (5 μm)	14.34	4.09
Contaminants				trace O, Cl, C	

Summary of Results

Free-standing GaN films were grown by various techniques upon nearly lattice-matched LGO and LAO substrates. Substrates grown upon LGO substrates were found to be brittle, and generally optically opaque. However, they had extremely good crystallinity, with narrower X-ray diffraction FWHMs than any technique, other than high-pressure solution growth, which was reported in the literature. Surface morphologies indicated step-flow growth and very planar surfaces. GaN/LGO films possessed high concentrations of carbon, oxygen, and chlorine, likely due to substrate decomposition.

The GaN films grown upon LAO substrates were found to have worse crystallinity and poorer surface morphology than films grown upon LGO. The surface roughness was in fact comparable to GaN/sapphire grown at the same temperature. The two advantages that films grown upon LAO possessed, in comparison to those grown upon LGO substrates, were increased transparency and lower impurity concentrations, especially for oxygen. This last characteristic suggests that films grown upon LAO would be more readily dopable with p-type dopants than films grown upon LGO substrates.

Overall, use of LAO as a template for thick film substrate growth provides an intermediate possibility between the relative extremes of sapphire and LGO in terms of crystallinity, surface morphology, thermal, chemical, and mechanical stability, and impurity incorporation.

CHAPTER 7

SUMMARY AND CONCLUSIONS

A novel chemistry was investigated and characterized for the atmospheric-pressure deposition of gallium nitride films that combined the advantages of the high crystal quality of metalorganic vapor-phase epitaxy (MOVPE) with the high growth rate of hydride vapor phase epitaxy (HVPE). The limits of the hydride-metalorganic vapor phase epitaxy (H-MOVPE) growth envelope between 500°C and the furnace-limited 950°C were investigated, and compared to literature results. Variation of process parameters such as V/III ratio and HCl/Ga ratio were also researched, and the effects upon film quality were tabulated. Films were characterized by growth rate measurement, X-ray diffraction (XRD), atomic force microscopy (AFM), Auger electron spectroscopy (AES), secondary ion mass spectrometry (SIMS), and photoluminescence (PL). The best results for single-crystalline thick film growth were obtained at 950°C, an ammonia flow rate of 500 sccm, and an HCl/Ga ratio of 2:1.

Thick gallium nitride films were grown upon lithium gallium oxide (LGO) and lithium aluminum oxide (LAO) substrates, which were nearly lattice-matched to gallium nitride. While the films grown upon LGO possessed superior crystal quality and surface morphology, the films grown upon LAO possessed greater mechanical stability and much lower impurity concentrations. Oxygen incorporation, in particular, was very high for films grown upon LGO. Investigation by SIMS revealed evidence of decomposition of the LGO substrate during hydride growth, but no decomposition of the LAO.

Finally, the thermodynamics of both the growth chemistry and nitride solid solutions were investigated. Theoretical variations of growth rate with process parameters were predicted and compared with experiment. While general trends between theoretical and experimental growth rates were similar, the theoretical results were not descriptive of the experimental without arbitrarily increasing the stability of the gallium nitride solid phase. The solid solution behavior of the nitrides was modeled by regular solution theory, using several models for interaction parameters. An empirical model was developed for sole use with nitrides, and compared with literature models. Experimental results for the InGaN system proved the model statistically indistinguishable from numerical and theoretical models currently published.

CHAPTER 8

RECOMMENDATIONS

While several interesting questions have been posed and answered by this research, others have been generated that have sufficient import or significance to motivate further exploration. A great deal of research involved exploring the fundamental process envelope of the H-MOVPE growth system. The next battery of research issues should involve stepwise improvement in GaN/Al₂O₃ growth techniques, centered on the question of how GaN/Al₂O₃ film quality can be improved for this chemistry. For the medium-to-far future, the question to be asked is whether the H-MOVPE growth system is suitable for making devices, especially LEDs.

To accomplish these goals, the following suggestions are offered. First and foremost, the clamshell furnace surrounding the reactor should be replaced in favor of a model that can maintain a growth temperature higher than 950°C. Four-zone controls should be sufficient to control the temperature profile of the reactor. Increased growth temperature will improve film quality and permit greater gallium fluxes, enabling higher growth rates for free-standing GaN film growth.

Another research opportunity available especially to this system is a detailed investigation of buffer layers. Both HVPE and MOCVD buffer layers could be grown, enabling investigation into the effects of polarity upon crystal and device quality. Also, AlN could be used in the system upon installation of a trimethylaluminum bubbler,

enabling further comparisons. Other pretreatments, such as sputtered ZnO and GaCl pretreatments may be investigated as well.

Another topic worthy of investigation is dopant behavior in the H-MOVPE system. Both carbon and magnesium could be investigated as potential p-type dopants for this chemistry. As noted in Chapter 3, carbon incorporates increasingly well into H-MOVPE films with increased hydrogen chloride flow. Carbon could be used as a compensating dopant to reduce donor concentrations, and to investigate codoping of GaN films with oxygen. Magnesium would likely be the most suitable dopant for growing p-type layers. Even if the same difficulties arise in the H-MOVPE system as arose in early HVPE research—namely the high stability of MgCl_2 in the gas phase, and trouble controlling the compositional uniformity of the doping—p-type MOCVD layers could be grown with Cp_2Mg . The ability to switch between MOCVD and HVPE growth modes at-will could thereby enable device production with greater ease than conventional HVPE. Whether devices can be produced in the current system is an interesting question.

The thermodynamics of GaN deposition (Chapter 4) can be investigated by using increased molar HCl flow rates to shift the thermodynamically-limited growth regime to lower temperature. As mentioned in that chapter, published values for the Gibbs energy of formation of $\text{GaN}_{(s)}$ as a function of temperature are too high to account for the actual deposition results. Due to a kinetic barrier to decomposition—catalytically removed when $\text{Ga}_{(l)}$ is present, for instance—the deposition of $\text{GaN}_{(s)}$ is at least a constrained equilibrium process. By identifying the growth/no growth boundary at a series of temperatures, a working value for $G(T)$ for the metastable $\text{GaN}_{(s)}$ can be found, which

may then be included on (Ga + N) phase diagrams. This addition would greatly improve the practical utility of such phase diagrams.

Further research into the thermodynamics of nitride solid solutions (Chapter 5) involves the refinement, development, and comparative testing of the Matsuoka and Ionic + Covalent solution thermodynamic theories from this work. Investigating the two other major nitride systems that possess miscibility gaps, namely the pseudobinary InAlN and the pseudoternary BAlGa₂N, could test these theories. The BAlGa₂N system, especially, provides boron solubilities that should differentiate between the two theories. Some experimental data has been gathered regarding these systems [277, 278], but was reported without precision sufficient to draw conclusions.

The first recommendation for further research on GaN/LAO is to find a reliable supplier of single-crystalline substrates, preferably one who understands that “single-crystalline” does not equate to “predominantly single crystal.” The scarcity of single-crystalline LAO substrates precludes wide-ranging research upon GaN/LAO.

Secondly, more and larger-area thick films should be grown once more substrates are procured. Once free-standing single-crystalline GaN is cheaply available in bulk, the sky is the figurative limit as far as materials and device research is concerned. All of the basic material-related research is instantly made more practical, and opportunities to explore device design and improvement broaden. This researcher is especially interested in device results using substrates produced by this method.

The H-MOVPE chemistry is unique in its ability to easily switch between hydride and metalorganic vapor phase epitaxies. While this work has answered several questions regarding various aspects of H-MOVPE nitride growth, interesting challenges yet remain.

LIST OF REFERENCES

1. Maruska, H. P. and Tietjen, J. J., Appl. Phys. Lett. **15** (1969) 327.
2. Edgar, J. H., J. Mater. Res. **7** (1992) 235.
3. Schulz, H. and Thiemann, K. H., Solid State Commun. **23** (1977) 815.
4. Pankove, J. I., Bloom, S. and Harbeke, G., RCA Rev. **36** (1975) 163.
5. Alekseevski, N. E., Samsonov, G. V. and Shulisova, O. I., Sov. Phys. JETP **19** (1963) 950.
6. Davydov, A. V. and Anderson, T. J., J. Electrochem. Soc. **146** (1999) 237.
7. Madar, R., Jacob, G., Hallias, J. and Fruchart, R., J. Crystal Growth **31** (1975) 197.
8. Grzegory, I., Bokowski, M., Jun, J. and Figurny, P., High Press. Res. **7** (1991) 284.
9. Grzegory, I., Jun, J., Bokowski, M., Krukowski, S., Wroblewski, M., Lucznik, B. and Porowski, S., J. Phys. Chem. Solids **56** (1995) 639.
10. Grzegory, I., Jun, J., Krukowski, S., Bokowski, M. and Porowski, S., Phys. B **185** (1993) 99.
11. Jones, D. and Lettington, A. H., Solid State Commun. **11** (1972) 701.
12. Logan, R. A., White, H. G. and Weigmann, W., Sol. State Electronics **14** (1971) 55.
13. Lorimor, O. G. and Dawson, L. R., J. Electrochem. Soc. **118** (1971) 292C.
14. Karpinski, J., Jun, J. and Porowski, S., J. Crystal Growth **66** (1984) 1.
15. Karpinski, J. and Porowski, S., J. Crystal Growth **66** (1984) 11.
16. Thurmond, C. D. and Logan, R. A., J. Electrochem. Soc. **119** (1972) 622.
17. Bloom, S., J. Phys. Chem. Solids **32** (1971) 2027.
18. Bloom, S., Harbeke, G., Meier, E. and Ortenberger, I. B., Phys. Stat. Solidi **B66** (1974) 161.

19. Grimmeiss, H. G., Groth, R. and Maak, J., *Z. Naturf.* **15a** (1960) 199.
20. Osamura, K., Nakajima, K., Murakami, Y., Shingu, P. and Ohtsuki, A., *Solid State Commun.* **11** (1972) 617.
21. Mohammad, S. N., Salvador, A. A. and Morkoc, H., *Proc. IEEE* **83** (1995) 1306.
22. Self, K., *Proc. IEEE* **83** (1995) 1305.
23. Sze, S. M., Physics of Semiconductor Devices (John Wiley and Sons: New York, 1981).
24. Nakamura, S., Senoh, M., Nagahama, S., Iwasa, N., Yamada, T. and Matsushita, T., *Jap. J. Appl. Phys.* **35** (1996) L217.
25. Pankove, J. I. and Hutchby, J. A., *J. Appl. Phys.* **47** (1976) 5387.
26. Liu, S. S., Cass, T. R. and Stevenson, D. A., *J. Electron. Mater.* **6** (1977) 237.
27. Maruska, H. P., Anderson, L. J. and Stevenson, D. A., *J. Electrochem. Soc.* **121** (1974) 1202.
28. Maruska, H. P., Stevenson, D. A. and Pankove, J. I., *Appl. Phys. Lett.* **22** (1973) 303.
29. Liu, S. S. and Stevenson, D. A., *J. Electrochem. Soc.* **125** (1978) 1161.
30. Marasina, A., Pikhtin, A. N., Pichugin, I. G. and Solomonov, A. V., *Phys. Stat. Solidi A* **38** (1976) 753.
31. Maruska, H. P., Rhines, W. C. and Stevenson, D. A., *Mater. Res. Bull.* **7** (1972) 777.
32. Grimmeiss, H. G. and Monemar, B., *J. Appl. Phys.* **41** (1970) 4054.
33. Morimoto, Y., *Jap. J. Appl. Phys.* **13** (1974) 1307.
34. Pankove, J. I. and Levin, E. R., *J. Appl. Phys.* **46** (1975) 1647.
35. Lagerstedt, O. and Monemar, B., *Phys. Rev.* **B19** (1979) 3064.
36. Shintani, A. and Minagawa, S., *J. Electrochem. Soc.* **123** (1976) 1575.
37. Pankove, J. I., *RCA Rev.* **34** (1973) 336.
38. Ilegems, M., *J. Crystal Growth* **13/14** (1972) 360.
39. Matsumoto, T., Sano, M. and Aoki, M., *Jap. J. Appl. Phys.* **13** (1974) 373.
40. Crouch, R. K., Debnam, W. J. and Fripp, A. L., *J. Mater. Sci.* **13** (1978) 2358.

41. Jacob, G., Boulou, M. and Furtado, M., J. Crystal Growth **42** (1977) 136.
42. Ilegems, M., Dingle, R. and Logan, R. A., J. Appl. Phys. **43** (1972) 3797.
43. Pankove, J. I., J. Electrochem. Soc. **119** (1972) 1118.
44. Shintani, A. and Minagawa, S., J. Electrochem. Soc. **123** (1976) 1725.
45. Jacob, G., Madar, R. and Hallias, J., Mater. Res. Bull. **11** (1976) 445.
46. Jacob, G., Boulou, M. and Furtado, M., J. Lumin. **17** (1978) 263.
47. Akasaki, I., Amano, H., Sawaki, N., Hashimoto, M., Ohki, Y. and Toyoda, Y., in Japan Annual Reviews in Electronics, Computers, and Telecommunications, Vol. 19, (Ohmsha, Ltd., Tokyo, 1986), 295.
48. Ohki, Y., Toyoda, Y., Kobayashi, H. and Akasaki, I., Proc. 9th International Symposium on GaAs and Related Compounds, Oiso, **63** (1981) 479.
49. Madar, R., Michel, D., Jacob, G. and Boulou, M., J. Crystal Growth **40** (1977) 239.
50. Pankove, J. I. and Hutchby, J. A., Appl. Phys. Lett. **24** (1974) 281.
51. Pankove, J. I., Miller, E. A. and Berkeyheiser, J., J. Lumin. **5** (1972) 84.
52. Pankove, J. I., Miller, E. A. and Berkeyheiser, J., RCA Rev. **32** (1971) 383.
53. Pankove, J. I. and Lampert, M. A., Phys. Rev. Lett. **33** (1974) 361.
54. Pankove, J. I., Berkeyheiser, J., Maruska, H. P. and Wittke, J., Solid State Commun. **8** (1970) 1051.
55. Pankove, J. I. and Schade, H., Appl. Phys. Lett. **21** (1974) 53.
56. Martinelli, R. U. and Pankove, J. I., Appl. Phys. Lett. **25** (1974) 549.
57. Pankove, J. I. and Berkeyheiser, J., Proc. IEEE **60** (1972) 1456.
58. Pankove, J. I., Miller, E. A. and Berkeyheiser, J., J. Lumin. **6** (1973) 54.
59. Ilegems, M., Dingle, R. and Logan, R. A., Bull. Am. Phys. Soc. **17** (1972) 233.
60. Ejder, E. and Fagerstrom, P.-O., J. Phys. Chem. Sol. **36** (1975) 289.
61. Monemar, B. and Lagerstedt, O., J. Appl. Phys. **50** (1979) 6480.
62. Cunningham, R. D., Brander, R. W., Knee, N. D. and Wickenden, D. K., J. Lumin. **5** (1972) 21.

63. Monemar, B., Phys. Rev. **B10** (1974) 676.
64. Pankove, J. I., J. Lumin. **7** (1973) 114.
65. Lagerstadt, O. and Monemar, B., J. Appl. Phys. **45** (1974) 2266.
66. Pankove, J. I., Maruska, H. P. and Berkeyheiser, J. E., Proc. 10th International Conference on the Physics of Semiconductors, (1970) 593.
67. Pankove, J. I., Duffy, M. T., Miller, E. A. and Berkeyheiser, J. E., J. Lumin. **8** (1973) 89.
68. Metcalfe, R. D., Wickenden, D. and Clark, W. C., J. Lumin. **16** (1978) 405.
69. Monemar, B., (2000) <http://nsr.mij.mrs.org/news/Richmond.html>.
70. Ren, F., Abernathy, C. R., Hove, J. M. V., Chow, P. P., Hickman, R., Klaasen, J. J., Kopf, R. F., Cho, H., Jung, K. B., Roche, J. R. L., Wilson, R., Han, J., Shul, R. J., Baca, A. G. and Pearton, S. J., MRS Internet J. Nitride Semicond. Res. **3** (1998) 41.
71. Ponce, F. A., Gallium Nitride and Related Materials : the First International Symposium on Gallium Nitride and Related Materials held November 27-December 1, 1995, Boston, Massachusetts, U.S.A. (Materials Research Society: Pittsburgh, PA, 1996).
72. Chu, T. L., Ito, K., Smeltzer, R. K. and Chu, S. S. C., J. Electrochem. Soc. **121** (1974) 159.
73. Matsumoto, T. and Aoki, M., Jap. J. Appl. Phys. **13** (1974) 1583.
74. Seifert, W., Bruhl, H. G. and Fitzl, G., Phys. Stat. Solidi **A61** (1980) 493.
75. Amano, H., Sawaki, N., Akasaki, I. and Toyoda, Y., Appl. Phys. Lett. **48** (1986) 353.
76. Humphreys, T. P., Sakow, C. A., Nemanich, R. J., Posthill, J. B., Rudder, R. A., Hattangady, S. V. and Markunas, R. J., Mater. Res. Soc. Symp. Proc. **162** (1990) 531.
77. Melnik, Y., Nikitina, I., Zubrilov, A. S., Sitnikova, A. A., Musikhin, U. G. and Dmitriev, V. A., Inst. Phys. Conf. Ser. **142** (1996) 863.
78. Shreter, Y. G., Rebane, Y. T., Davis, T. J., Barnard, J., Darbyshire, M., Steeds, J. W., Perry, W. G., Bremser, M. D. and Davis, R. F., Mater. Res. Soc. Symp. Proc. **449** (1997) 683.
79. Sime, R. J. and Margrave, J. L., J. Phys. Chem. **60** (1956) 810.
80. Groh, R., Gerey, G., Bartha, L. and Pankove, J. I., Phys. Stat. Solidi **A26** (1974) 353.
81. Schoonmaker, R. C., Buhl, A. and Lemley, J., J. Phys. Chem. **69** (1965) 3455.

82. Munir, Z. A. and Searcy, A. W., J. Chem. Phys. **42** (1965) 4223.
83. Van Vechten, J. A., J. Electrochem. Soc. **122** (1975) 423.
84. Van Vechten, J. A., J. Electrochem. Soc. **122** (1975) 419.
85. Seifert, W., Franzheld, R., Butter, E., Sobotta, H. and Riede, V., Cryst. Res. Tech. **18** (1983) 383.
86. Lee, H., Yuri, M., Ueda, T. and Harris, J. S. J., Mater. Res. Soc. Symp. Proc. **423** (1996) 233.
87. Molnar, R. J., Lei, T. and Moustakas, T. D., Appl. Phys. Lett. **62** (1993) 72.
88. Neugebauer, J. and Van de Walle, C. G., Phys. Rev. **B50** (1994) 8067.
89. Molnar, R. J., Nichols, K. B., Maki, P., Brown, E. R. and Melngailis, I., Mater. Res. Soc. Symp. Proc. **378** (1995) 479.
90. Elsner, J., Frauenheim, T., Haugk, M., Gutierrez, R., Jones, R. and Heggie, M. I., Mater. Res. Soc. Symp. Proc. **537** (1999) 29.
91. Northrup, J. E., Appl. Phys. Lett. **72** (1998) 2316.
92. Chien, F.-R., Nutt, S. R., Yoo, W. S., Kimoto, T. and Matsunami, H., J. Crystal Growth **137** (1994) 175.
93. Qian, W., Skowronski, M. and Rohrer, G. S., Mater. Res. Soc. Symp. Proc. **423** (1996) 475.
94. Itoh, N., Rhee, J. C., Kawabata, T. and Koike, S., J. Appl. Phys. **58** (1985) 1828.
95. Goorsky, M. S., Polyakov, A. Y., Skowronski, M., Shin, M. and Greve, D. W., Mater. Res. Soc. Symp. Proc. **449** (1997) 489.
96. Powell, R. C., Lee, N.-E., Kim, Y.-W. and Greene, J. E., J. Appl. Phys. **73** (1993) 189.
97. Qian, W., Skowronski, M., Graef, M. D., Doverspike, K., Rowland, L. B. and Gaskill, D. K., Appl. Phys. Lett. **66** (1995) 1252.
98. Kung, P., Saxler, A., Walker, D., Zhang, X., Lavado, R., Kim, K. S. and Razeghi, M., Mater. Res. Soc. Symp. Proc. **449** (1997) 79.
99. Hall, E. O., Twinning and Diffusionless Transformations in Metals (Butterworths Publications Ltd.: London, 1954).

100. Fremunt, R., Cerny, P., Kohout, J., Rosicka, V. and Burger, A., *Cryst. Res. Tech.* **16** (1981) 1257.
101. Bharatan, S., Jones, K. S., Pearton, S. J., Abernathy, C. R., and Ren, F., *Mater. Res. Soc. Symp. Proc.* **339** (1994) 491.
102. Huang, S.-C., Wang, H.-Y., Hsu, C.-J., Gong, J.-R., Chiang, C.-I., Tu, S.-L. and Chang, H., *J. Mater. Sci. Lett.* **17** (1998) 1281.
103. Karam, N. H., Parodos, T., Colter, P., McNulty, D., Rowland, W., Schetzina, J., El-Masry, N. and Bedair, S. M., *Appl. Phys. Lett.* **67** (1995) 94.
104. McIntosh, F. G., Piner, E. L., Roberts, J. C., Behbehani, M. K., Aumer, M. E., El-Masry, N. A. and Bedair, S. M., *Appl. Surf. Science* **112** (1997) 98.
105. Oktyabrsky, S., Dovidenko, K., Sharma, A. K., Joshkin, V. and Narayan, J., *Mater. Res. Soc. Symp. Proc.* **537** (1999) 43.
106. Cappelli, M. A., Kull, A. E., Schwendner, K., Lee, H., Harris, S. J., Jr. and Mroczkowski, J., *Materials Letters* **31** (1997) 161.
107. Cappelli, M. A., Kull, A. E., Schwendner, K., Lee, H., Harris, S. J. J. and Mroczkowski, J., *Mater. Res. Soc. Symp. Proc.* **423** (1996) 359.
108. Vodakov, Y. A., Mokhov, E. N., Ramm, M. G., Roenkov, A. D., Ostroumov, A. G., Wolfson, A. A., Karpov, S. Y., Makarov, Y. N. and Jurgensen, H., *Mater. Res. Soc. Symp. Proc.* **482** (1997) 27.
109. Porowski, S., Bokowski, M., Lucznik, B., Wroblewski, M., Krukowski, S., Grzegory, I., Leszyzynski, M., Nowak, G., Pakula, K. and Baranowski, J., *Mater. Res. Soc. Symp. Proc.* **449** (1997) 35.
110. Porowski, S., *J. Crystal Growth* **189/190** (1998) 153.
111. Kryliouk, O., Dann, T., Anderson, T., Gaskov, A., Jones, K., Li, J. H. and Chai, B., *Proc. 8th Biennial Workshop Organometallic Vapor Phase Epitaxy*, Dana Point, CA, USA, (1997) 14.
112. Dingle, R., Sell, D. D., Stokowski, S. E. and Ilegems, M., *Phys. Rev.* **B4** (1971) 1211.
113. Dingle, R. and Ilegems, M., *Sol. State Commun.* **9** (1971) 175.
114. Kosicki, B. B., Powell, R. J. and Burgiel, J. C., *Phys. Rev. Lett.* **24** (1970) 1421.
115. Morimoto, Y. and Ushio, S., *Jap. J. Appl. Phys.* **13** (1974) 365.

116. Linden, M., Ejder, E. and Hellborg, R., Phys. Stat. Solidi **A45** (1978) K167.
117. Seifert, W. and Tempel, A., Phys. Stat. Solidi **A23** (1974) K39.
118. Manasevit, H. M., Erdmann, F. M. and Simpson, W. I., J. Electrochem. Soc. **118** (1971) 1864.
119. Marasina, L. A., Pikhtin, A. N., Pichugin, I. G. and Solomonov, A. V., Sov. Phys. Semicond. **9** (1975) 1162.
120. Dai, R., Fu, S., Xie, J., Fan, G., Hu, G., Schrey, H. and Klingshirn, C., J. Phys. C: Solid State Phys. **15** (1982) 393.
121. Nickl, J. J., Just, W. and Bertinger, R., Mater. Res. Bull. **9** (1974) 1413.
122. Barker, A. S. J. and Ilegems, M., Phys. Rev. **B7** (1973) 743.
123. Logan, R. A. and Thurmond, C. D., J. Electrochem. Soc. **119** (1972) 1727.
124. Eckey, L., Podlowski, L., Goldner, A., Hoffmann, A., Broser, I., Meyer, B. K., Volm, D., Streibl, T., Hiramatsu, K., Detchprohm, T., Amano, H. and Akasaki, I., Inst. Phys. Conf. Ser. **142** (1996) 943.
125. Morimoto, Y., Uchiho, K. and Ushio, S., J. Electrochem. Soc. **120** (1973) 1783.
126. Kosicki, B. B. and Kahng, D., J. Vac. Sci. Tech. **6** (1969) 593.
127. Wickenden, D., Faulkner, K. R., Brander, R. W. and Isherwood, B. J., J. Crystal Growth **9** (1971) 158.
128. Chu, T. L., J. Electrochem. Soc. **118** (1971) 1200.
129. Faulkner, K. R., Wickenden, D. K., Isherwood, B. J., Richards, B. P. and Scobey, I. H., J. Mater. Sci. **5** (1970) 308.
130. Kryliouk, O., Reed, M., Dann, T., Anderson, T. and Chai, B., Mater. Sci. Eng. **B59** (1999) 6.
131. Kryliouk, O., Reed, M., Dann, T., Anderson, T. and Chai, B., Mater. Sci. Eng. **B56** (1999) 1.
132. Kryliouk, O., Reed, M., Mastro, M., Anderson, T. and Chai, B., Phys. Stat. Solidi **A176** (1999) 407.
133. Doolittle, W. A., Kropewnicki, T., Carter-Coman, C., Stock, S., Kohl, P., Jokerst, N. M., Metzger, R. A., Kang, S., Lee, K. K., May, G. and Brown, A. S., J. Vac. Sci. Tech. **B16** (1998) 1300.

134. Okada, M., Higaki, Y., Yanagi, T., Shimizu, Y., Nanishi, Y., Ishii, T. and Miyazawa, S., *J. Crystal Growth* **189/190** (1998) 213.
135. Ishii, T., Tazoh, Y. and Miyazawa, S., *Jap. J. Appl. Phys.* **36** (1997) L139.
136. Ishii, T., Mukaida, M., Nishihara, T., Hayashi, S. and Shinohara, M., *J. Appl. Phys.* **37** (1998) L672.
137. Ishii, T., Tazoh, Y. and Miyazawa, S., *J. Crystal Growth* **189/190** (1998) 208.
138. Kryliouk, O. M., Dann, T. W., Anderson, T. J., Maruska, H. P., Zhu, L. D., Daly, J. T., Lin, M.-E., Norris, P., Chai, B. H. T., Kisker, D. W., Li, J. H. and Jones, K. S., *Mater. Res. Soc. Symp. Proc.* **449** (1997) 123.
139. Li, J. H., Kryliouk, O., Holloway, P. H., Anderson, T. J. and Jones, K. S., *Mater. Res. Soc. Symp. Proc.* **468** (1997) 167.
140. Middleton, P. G., Trager-Cowan, C., O'Donnell, K. P., Cheng, T. S., Hooper, S. E. and Foxon, C. T., *Mater. Sci. Eng.* **B43** (1997) 154.
141. Nicholls, J. F. H., Gallagher, H., Henderson, B., Trager-Cowan, C., Middleton, P. G., O'Donnell, K. P., Cheng, T. S., Foxon, C. T. and Chai, B. H. T., *Mater. Res. Soc. Symp. Proc.* **395** (1996) 535.
142. Kung, P., Saxler, A., Zhang, X., Walker, D., Lavado, R. and Rzeghi, M., *Appl. Phys. Lett.* **69** (1996) 2116.
143. Matyi, R. J., Doolittle, W. A. and Brown, A. S., *J. Phys. D: Appl. Phys.* **32** (1999) A61.
144. Johnson, M. A. L., Fujita, S., Rowland, W. H. J., Bowers, K. A., Hughes, W. C., He, Y. W., El-Masry, N. A., Cook, J. W. J., Schetzina, J. F., Ren, J. and Edmond, J. A., *Sol. State Electronics* **41** (1997) 213.
145. Johnson, M. A. L., Hughes, W. C., Rowland, W. H. J., Cook, J. W. J., Schetzina, J. F., Leonard, M., Kong, H. S., Edmond, J. A. and Zavada, J., *J. Crystal Growth* **175/176** (1997) 72.
146. Andrianov, A. V., Lacklison, D. E., Orton, J. W., Cheng, T. S., Foxon, C. T., O'Donnell, K. P. and Nicholls, J. F. H., *Semicond. Sci. Technol.* **12** (1997) 59.
147. Doolittle, W. A., Kang, S., Kropewnicki, T., Stock, S., Kohl, P. A. and Brown, A. S., *J. Electron. Mater.* **27** (1998) L58.
148. Juza, R. and Hahn, H., *Z. Allorg. Allg. Chem.* **239** (1938) 282.
149. Juza, R. and Hahn, H., *Z. Allorg. Allg. Chem.* **244** (1940) 133.

150. Isherwood, B. J. and Wickenden, D. K., *J. Mater. Sci.* **5** (1970) 869.
151. Lorenz, M. R. and Binkowski, B. B., *J. Electrochem. Soc.* **109** (1962) 24.
152. Rabenau, A., in *Compound Semiconductors*, Vol. 1, Willardson, R. K. and Goering, H. L. (Reinhold Pub. Corp., New York, 1962), 174.
153. Ban, V. S., *J. Electrochem. Soc.* **119** (1972) 761.
154. Lee, H., Yuri, M., Ueda, T. and Harris, T. S., *J. Electron. Mater.* **26** (1997) 898.
155. Molnar, R. J., Gotz, W., Romano, L. T. and Johnson, N. M., *J. Crystal Growth* **178** (1997) 147.
156. Safvi, S. A., Perkins, N. R., Horton, M. N. and Kuech, T. F., *Mater. Res. Soc. Symp. Proc.* **449** (1997) 289.
157. Safvi, S. A., Perkins, N. R., Horton, M. N., Matyi, R. and Kuech, T. F., *J. Crystal Growth* **182** (1997) 233.
158. Safvi, S. A., Perkins, N. R., Horton, M. N., Thon, A., Zhi, D. and Kuech, T. F., *Mater. Res. Soc. Symp. Proc.* **423** (1996) 227.
159. Perkins, N. R., Horton, M. N., Zhi, D., Matyi, R. J., Bandic, Z. Z., McGill, T. C. and Kuech, T. F., *Mater. Res. Soc. Symp. Proc.* **423** (1996) 287.
160. Perkins, N. R., Horton, M. N., Bandic, Z. Z., McGill, T. C. and Kuech, T. F., *Mater. Res. Soc. Symp. Proc.* **423** (1996) 243.
161. Matyi, R. J., Zhi, D., Perkins, N. R., Horton, M. N. and Kuech, T. F., *Mater. Res. Soc. Symp. Proc.* **423** (1996) 239.
162. Romano, L. T., Molnar, R. J., Krusor, B. S., Anderson, G. A., Bour, D. P. and Maki, P., *Mater. Res. Soc. Symp. Proc.* **423** (1996) 245.
163. Molnar, R. J., Aggarwal, R., Liao, Z. L., Brown, E. R., Melngailis, I., Gotz, W., Romano, L. T. and Johnson, N. M., *Mater. Res. Soc. Symp. Proc.* **395** (1996) 189.
164. Detchprohm, T., Hiramatsu, K., Itoh, K. and Akasaki, I., *Jap. J. Appl. Phys.* **31** (1992) L1454.
165. Götz, W., Walker, J., Romano, L. T., Johnson, N. M. and Molnar, R. J., *Mater. Res. Soc. Symp. Proc.* **449** (1997) 525.
166. Skromme, B. J., Zhao, H., Wang, D., Kong, H. S., Leonard, M. T., Bulman, G. E. and Molnar, R. J., *Appl. Phys. Lett.* **71** (1997) 829.

167. Naniwae, K., Itoh, S., Amano, H., Itoh, K., Hiramatsu, K. and Akasaki, I., *J. Crystal Growth* **99** (1990) 381.
168. Maki, P. A., Molnar, R. J., Aggarwal, R. L., Liao, Z.-L. and Melngailis, I., *Mater. Res. Soc. Symp. Proc.* **395** (1996) 919.
169. Detchprohm, T., Amano, H., Hiramatsu, K. and Akasaki, I., *J. Crystal Growth* **128** (1993) 384.
170. Detchprohm, T., Hiramatsu, K., Sawaki, N. and Akasaki, I., *J. Crystal Growth* **137** (1994) 170.
171. Detchprohm, T., Hiramatsu, K., Sawaki, N. and Akasaki, I., *J. Crystal Growth* **145** (1994) 192.
172. Meyer, B. K., Volm, D., Graber, A., Alt, H. C., Detchprohm, T., Amano, A. and Akasaki, I., *Sol. State Commun.* **95** (1995) 597.
173. Volm, D., Streibl, T., Meyer, B. K., Detchprohm, T., Amano, H. and Akasaki, I., *Sol. State Commun.* **96** (1995) 53.
174. Detchprohm, T., Kuroda, T., Hiramatsu, K., Sawaki, N. and Goto, H., *Inst. Phys. Conf. Ser.* **142** (1996) 859.
175. Molnar, R. J., Maki, P., Aggarwal, R., Liao, Z. L., Brown, E. R., Melngailis, I., Gotz, W., Romano, L. T. and Johnson, N. M., *Mater. Res. Soc. Symp. Proc.* **423** (1996) 221.
176. Gotz, W., Romano, L. T., Walker, J., Johnson, N. M. and Molnar, R. J., *Appl. Phys. Lett.* **72** (1998) 1214.
177. Ueda, T., Huang, T.-F., Spruytte, S., Lee, H., Yuri, M., Itoh, K., Baba, T. and Harris, J. S., Jr., *J. Crystal Growth* **187** (1998) 340.
178. Nakamura, S., Senoh, M., Nagahama, S.-i., Iwasa, N., Yamada, T., Matsushita, T., Kiyoku, H., Sugimoto, Y., Kozaki, T., Umemoto, H., Sano, M. and Chocho, K., *Jap. J. Appl. Phys.* **37** (1998) L309.
179. Nakamura, S., *Photonics Spectra* **32** (1998) 130.
180. Singh, R., Barrett, R. J., Gomes, J. J., Dabkowski, F. P. and Moustakas, T. D., *MRS Internet J. Nitride Semicond. Res.* **3** (1998) 13.
181. Porowski, S., *Mater. Sci. Eng.* **B44** (1997) 407.

182. Baranowski, J. M., Liliental-Weber, Z., Korona, K., Pakula, K., Stepniewski, R., Wyszomolek, A., Grzegory, I., Nowak, G., Porowski, S., Monemar, B. and Bergman, P., *Mater. Res. Soc. Symp. Proc.* **449** (1997) 393.
183. Baranowski, J. M. and Porowski, S., *Proc. 9th IEEE Conference on Semiconducting and Insulating Materials, Toulouse, France*, (1996) 77.
184. Leszczynski, M., Grzegory, I., Teisseyre, H., Suski, T., Bockowski, M., Jun, J., Baranowski, J. M., Porowski, S. and Domagala, J., *J. Crystal Growth* **169** (1996) 235.
185. Porowski, S. and Grzegory, I., *J. Crystal Growth* **178** (1997) 174.
186. Pelzmann, A., Kirchner, C., Mayer, M., Schwegler, V., Schauler, M., Kamp, M., Ebeling, K. J., Grzegory, I., Leszczynski, M., Nowak, G. and Porowski, S., *J. Crystal Growth* **189/190** (1998) 167.
187. Porowski, S., *J. Crystal Growth* **166** (1996) 583.
188. Perlin, P., Suski, T., Polian, A., Chervin, J. C., Knap, W., Camassel, J., Grzegory, I., Porowski, S. and Erickson, J. W., *Mater. Res. Soc. Symp. Proc.* **449** (1997) 689.
189. Suski, T., Perlin, P., Leszczynski, M., Teisseyre, H., Grzegory, I., Jun, J., Bockowski, M., Porowski, S., Pakula, K., Wyszomolek, A. and Baranowski, J. M., *Mater. Res. Soc. Symp. Proc.* **395** (1996) 15.
190. Suski, T., Perlin, P., Teisseyre, H., Leszczynski, M., Grzegory, I., Jun, J., Bockowski, M., Porowski, S. and Moustakas, T. D., *Appl. Phys. Lett.* **67** (1995) 2188.
191. Suski, T., Krueger, J., Kisielowski, C., Phatak, P., Leung, M. S. H., Liliental-Weber, Z., Gassmann, A., Newman, N., Rubin, M. D., Weber, E. R., Grzegory, I., Jun, J., Bockowski, M., Porowski, S. and Helava, H. I., *Mater. Res. Soc. Symp. Proc.* **423** (1996) 329.
192. Teisseyre, H., Leszczynski, M., Suski, T., Grzegory, I., Bockowski, M., Jun, J., Porowski, S., Pakula, K., Robert, J.-L., Beaumont, B., Gibart, P., Vaille, M. and Faurie, J. P., *Semicond. Sci. Technol.* **12** (1997) 240.
193. Melnik, Y. V., Vassilevski, K. V., Nikitina, I. P., Babanin, A. I., Davydov, V. Y. and Dmitriev, V. A., *MRS Internet J. Nitride Semicond. Res.* **2** (1997) 39.
194. Perlin, P., Suski, T., Polian, A., Chervin, J. C., Litwin-Staszewska, E., Grzegory, I., Porowski, S. and Erickson, J. W., *Mater. Res. Soc. Symp. Proc.* **449** (1997) 519.
195. Dalven, R., in *Introduction to Applied Solid State Physics*, Vol. (Plenum Press, New York, 1980), 199.
196. Pankove, J. I., *Mater. Res. Soc. Symp. Proc.* **162** (1990) 515.

197. Pankove, J. I. and Norris, P. E., RCA Rev. **33** (1972) 377.
198. Fischer, A. G., Sol. State Electronics **2** (1961) 232.
199. Amano, H., Kito, M., Hiramatsu, K. and Akasaki, I., Jap. J. Appl. Phys. **28** (1989) L2112.
200. Krasnoperov, V. A. and Fainer, I. S., Optics and Spectrosc. **26** (1969) 166.
201. Chichibu, S., Azuhata, T., Sota, T. and Nakamura, S., Appl. Phys. Lett. **70** (1997) 2822.
202. Matsuoka, T., J. Crystal Growth **124** (1992) 433.
203. Matsuoka, T., Yoshimoto, N., Sasaki, T. and Katsui, A., J. Electron. Mater. **21** (1992) 157.
204. Yoshimoto, N., Matsuoka, T., Sasaki, T. and Katsui, A., Appl. Phys. Lett. **59** (1991) 2251.
205. Nakamura, S. and Makai, T., Jap. J. Appl. Phys. **31** (1992) L1457.
206. Kum, D. and Byun, D., J. Electron. Mater. **26** (1997) 1098.
207. Dingle, R., Leheny, R. F., Shaklee, K. L. and Zetterstrom, R. B., Bull. Am. Phys. Soc. **16** (1971) 408.
208. Seifert, W., Fitzl, G. and Butter, E., J. Crystal Growth **52** (1981) 257.
209. Grudowski, P. A., Holmes, A. L., Eiting, C. J. and Dupuis, R. D., JOM **48** (1996) 46.
210. Dingle, R., Leheny, R. F., Shaklee, K. L. and Zetterstrom, R. B., Appl. Phys. Lett. **19** (1971) 5.
211. Amano, H., Akasaki, I., Hiramatsu, K., Koide, N. and Sawaki, N., Thin Solid Films **163** (1988) 415.
212. Shintani, A., Takano, Y., Minagawa, S. and Mari, M., J. Electrochem. Soc. **125** (1978) 2076.
213. Nakamura, S., Mukai, T., Senoh, M. and Iwasa, N., Jap. J. Appl. Phys. **31** (1992) L139.
214. Pearton, S. J., Abernathy, C. R. and Ren, F., Electronics Lett. **30** (1994) 527.
215. Zavada, J. M., Wilson, R. G., Pearton, S. J. and Abernathy, C. R., Mater. Res. Soc. Symp. Proc. **339** (1994) 553.

216. Nakamura, S., Senoh, M., Nagahama, S.-i., Iwasa, N., Yamada, T., Matsushita, T., Kiyoku, H. and Sugimoto, Y., *Jap. J. Appl. Phys.* **35** (1996) L74.
217. Szweda, R., *III-Vs Review* **10** (1997) 22.
218. Mihopoulos, T. G., Gupta, V. and Jensen, K. F., *J. Crystal Growth* **195** (1998) 733.
219. Safvi, S. A., Redwing, J. M., Thon, A., Flynn, J. S., Tischler, M. A. and Kuech, T. F., *Mater. Res. Soc. Symp. Proc.* **449** (1997) 101.
220. Theodoropoulos, C., Mountziaris, T. J., Moffat, H. K. and Han, J., *J. Crystal Growth* **217** (2000) 65.
221. Safvi, S. A., Redwing, J. M., Tischler, M. A. and Kuech, T. F., *J. Electrochem. Soc.* **144** (1997) 1789.
222. Sun, J., Redwing, J. M. and Kuech, T. F., *Phys. Stat. Solidi A* **176** (1999) 693.
223. Flemish, J.R., Jones, K.A. and Ban, V.S., "Development of the Merged Hydride VPE/MOCVD Epitaxial Growth Method and the Selective Epitaxy/Plasma Etch Techniques for III-V Materials," U.S. Army SBIR Contract DAL01-C-0938 (1991).
224. Shintani, A. and Minagawa, S., *J. Crystal Growth* **22** (1974) 1.
225. Jacko, M. G. and Price, S. J. W., *Can. J. Chem.* **41** (1963) 1560.
226. Mihopoulos, T. G., Ph.D. diss., MIT, Department of Chemical Engineering, 1998.
227. Talalaev, R. A., Yakovlev, E. V., Karpov, S. Y. and Makarov, Y. N., *J. Crystal Growth* **230** (2001) 232.
228. Chen, C. H., Liu, H., Steigerwald, D., Imler, W., Kuo, C. P., Craford, M. G., Ludowise, M., Lester, S. and Amano, J., *J. Electron. Mater.* **25** (1996) 1004.
229. Stringfellow, G. B., Organometallic Vapor Phase Epitaxy: Theory and Practice (Academic Press: San Diego, CA, 1999).
230. Mastro, M. A., Kryliouk, O. M., Reed, M. D., Anderson, T. J., Davydov, A. and Shapiro, A., *Phys. Stat. Solidi* (2001).
231. Cadoret, R. and Trassoudaine, A., *J. Phys. Condensed Matter* **13** (2001) 6893.
232. Karpov, S. Y., Prokofyev, V. G., Yakovlev, E. V., Talalaev, R. A. and Makarov, Y. N., *MRS Internet J. Nitride Semicond. Res.* **4** (1999) 4.
233. Zhang, X., Kung, P., Walker, D., Saxler, A. and Razeghi, M., *Mater. Res. Soc. Symp. Proc.* **395** (1996) 625.

234. Wang, H. Y., Huang, S. C., Yan, T. Y., Gong, J. R., Lin, T. Y. and Chen, Y. F., *Mater. Sci. Eng.* **B57** (1999) 218.
235. Xu, H. Z., Bell, A., Wang, Z. G., Okada, Y., Kawabe, M., Harrison, I. and Foxon, C. T., *J. Crystal Growth* **222** (2001) 96.
236. Smith, W. R., *Ind. Eng. Chem. Fundam.* **19** (1980) 1.
237. Sandler, S. I., Chemical and Engineering Thermodynamics (John Wiley & Sons: New York, 1989).
238. Chase, M. W., JANAF Thermochemical Tables; (American Chemical Society: Washington, DC, and American Institute of Physics: New York, for the National Bureau of Standards), issued as Supplement #1 to Volume 14 of the *Journal of Physical and Chemical Reference Data*; 3rd ed., 1986.
239. Barin, I., Thermochemical Data of Pure Substances (VCH: Weinheim, 1993).
240. Davydov, A. V., Boettinger, W. J., Kattner, U. R. and Anderson, T. J., *Phys. Stat. Solidi A* **188** (2001) 407.
241. Wang, T., Morishima, Y., Naoi, N. and Sakai, S., *J. Crystal Growth* **213** (2000) 188.
242. Wu, X. H., Fini, P., Tarsa, E. J., Heying, B., Keller, S., Mishra, U. K., DenBaars, S. P. and Speck, J. S., *J. Crystal Growth* **189-190** (1998) 231.
243. Stringfellow, G. B., *J. Phys. Chem. Sol.* **33** (1972) 665.
244. Stringfellow, G. B., *J. Phys. Chem. Sol.* **34** (1973) 1749.
245. Phillips, J. C., Bonds and Bands in Semiconductors (Academic Press: New York, 1973).
246. Wei, C. H. and Edgar, J. H., *J. Crystal Growth* **217** (2000) 109.
247. Wei, C. H. and Edgar, J. H., *J. Crystal Growth* **208** (2000) 179.
248. Matsuoka, T., *J. Crystal Growth* **189/190** (1998) 19.
249. Matsuoka, T., *MRS Internet J. Nitride Semicond. Res.* **3** (1998) 54.
250. Matsuoka, T., *Appl. Phys. Lett.* **71** (1997) 105.
251. Keating, P. N., *Phys. Rev.* **145** (1966) 637.
252. Kim, K., Lambrecht, W. R. L. and Segall, B., *Phys. Rev. B* **53** (1996) 16310.
253. Ho, I. H. and Stringfellow, G. B., *Mater. Res. Soc. Symp. Proc.* **449** (1997) 871.

254. Ho, I.-h. and Stringfellow, G. B., Appl. Phys. Lett. **69** (1996) 2701.
255. Ho, K.-L., Ph.D. diss., MIT, Dept. of Chemical Engineering, 1991.
256. Takayama, T., Yuri, M., Itoh, K., Baba, T. and Harris, J. S. J., J. Crystal Growth **222** (2001) 29.
257. Ito, T., Jap. J. Appl. Phys. Pt. 2: Letters **37** (1998) L574.
258. Ito, T., Khor, K. E. and Das Sarma, S., Phys. Rev. B **41** (1990) 3893.
259. Ito, T., Jap. J. Appl. Phys., pt 2 **36** (1997) L1065.
260. Wang, L.-W., Bellaiche, L., Wei, S.-H. and Zunger, A., Phys. Rev. Lett. **80** (1998) 4725.
261. Kent, P. R. C. and Zunger, A., Phys. Rev. Lett. **86** (2001) 2613.
262. Kim, K. and Zunger, A., Phys. Rev. Lett. **86** (2001) 2609.
263. Bellaiche, L., Wei, S.-H. and Zunger, A., Phys. Rev. B **54** (1996) 17568.
264. Zhang, S. B. and Zunger, A., Appl. Phys. Lett. **71** (1997) 677.
265. Phillips, J. C., Phys. Rev. Lett. **20** (1968) 550.
266. Lawaetz, P., Phys. Rev. B **5** (1972) 4039.
267. Melnik, Y., Nikolaev, A., Nikitina, I., Vassilevski, K. and Dmitriev, V., Proc. 1997 MRS Fall Meeting, Boston, MA, **482** (1997) 269.
268. Onabe, K., Jap. J. Appl. Phys. **21** (1982) L323.
269. Piner, E. L., El-Masry, N., Liu, S. X. and Bedair, S. M., Mater. Res. Soc. Symp. Proc. **482** (1998) 125.
270. Koukitu, A., Hama, S.-i., Taki, T. and Seki, H., Jap. J. Appl. Phys., pt 1 **37** (1998) 762.
271. Koukitu, A., Takahashi, N., Taki, T. and Seki, H., J. Crystal Growth **170** (1997) 306.
272. Scholz, F., Off, J., Kniest, A., Goergens, L. and Ambacher, O., Mater. Sci. Eng. **B59** (1999) 268.
273. Van der Stricht, W., Moerman, I., Demeester, P., Crawley, J. A. and Thrush, E. J., J. Crystal Growth **170** (1997) 344.

274. Keller, S., Keller, B. P., Kapolnek, D., Mishra, U. K., Denbaars, S. P., Shmagin, I. K., Kolbas, R. M. and Krishnankutty, S., *J. Crystal Growth* **170** (1997) 349.
275. Yamaguchi, S., Kariya, M., Nitta, S., Amano, H. and Akasaki, I., *Appl. Surf. Science* **159** (2000) 414.
276. Popovici, G., Xu, G. Y., Botchkarev, A., Kim, W., Tang, H., Salvador, A., Strange, R., White, J. O. and Morkoc, H., *Mater. Res. Soc. Symp. Proc.* **468** (1997) 219.
277. Wei, C. H. and Edgar, J. H., *J. Crystal Growth* **217** (2000) 109.
278. Wei, C. H. and Edgar, J. H., *J. Crystal Growth* **208** (2000) 179.

BIOGRAPHICAL SKETCH

Michael Donley Reed was born in Pittsburgh, PA on March 27, 1970 to W. Donley and Evelyn C. Reed. He attended Gateway Senior High School in Monroeville, PA, where he was active in the National Forensics League, Chess Club, and several mathematics and scientific clubs and teams. He was a member of the National Honor Society and a Richard K. Mellon National Merit Scholar, and graduated with highest honors.

He attended Carnegie Mellon University in Pittsburgh, PA, graduating with a double major Bachelor of Science degree in chemical engineering and engineering and public policy. While at Carnegie Mellon, he was President of Kappa Chapter of Alpha Phi Omega National Service Fraternity, Chairman of the Student Government Elections, and later a member of the Student Government. He additionally worked in Carnegie Mellon's Academic Computing Department, attaining the highest managerial and technical positions open to students, despite being a chemical engineer by degree.

During the summer of 1990, he worked for Dow Chemical Company in Granville, OH, performing research with Dr. Richard Booth on automatic testing instruments for plastic foams. During the summer of 1991, he worked at Carnegie Mellon's Chemical Engineering Department, researching deposition of zinc cadmium telluride for the growth of infrared photodetectors. This work was performed with Drs. Paul Sides, Ed Ko, and In-Hwan Oh.

He entered the Chemical Engineering Department at the University of Florida in August of 1992.

I certify that I have read this study and that in my opinion it conforms to acceptable standards of scholarly presentation and is fully adequate, in scope and quality, as a dissertation for the degree of Doctor of Philosophy.



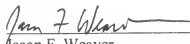
Timothy J. Anderson, Chairman
Professor of Chemical Engineering

I certify that I have read this study and that in my opinion it conforms to acceptable standards of scholarly presentation and is fully adequate, in scope and quality, as a dissertation for the degree of Doctor of Philosophy.



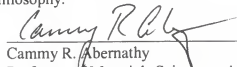
Fan Ren
Professor of Chemical Engineering

I certify that I have read this study and that in my opinion it conforms to acceptable standards of scholarly presentation and is fully adequate, in scope and quality, as a dissertation for the degree of Doctor of Philosophy.



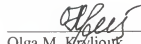
Jason F. Weaver
Assistant Professor of Chemical
Engineering

I certify that I have read this study and that in my opinion it conforms to acceptable standards of scholarly presentation and is fully adequate, in scope and quality, as a dissertation for the degree of Doctor of Philosophy.



Cammy R. Abernathy
Professor of Materials Science and
Engineering

I certify that I have read this study and that in my opinion it conforms to acceptable standards of scholarly presentation and is fully adequate, in scope and quality, as a dissertation for the degree of Doctor of Philosophy.



Olga M. Kozliouk
Research Associate Professor of Chemical
Engineering

This dissertation was submitted to the Graduate Faculty of the College of Engineering and to the Graduate School and was accepted as partial fulfillment of the requirements for the degree of Doctor of Philosophy.

May 2002



Pramod P. Khargonekar
Dean, College of Engineering

Winfred M. Phillips
Dean, Graduate School



.R325

